Experimental and computational study of the aerodynamic characteristics of archery arrows

Ortiz Enriquez Julio Cesar

Doctoral Dissertation

Graduate School of Informatics and Engineering

Department of Mechanical Engineering and Intelligent Systems

The University of Electro-Communications

January 2021

Experimental and computational study of the aerodynamic characteristics of archery arrows

Examining Committee:

Supervisor: Miyazaki Takeshi
Members: Matuttis Hans-Georg
Okawa Tomio
Chiba Kazuhisa
Mamori Hiroya

論文概要

本論文では、アーチェリー矢の空力特性が実験と数値シミュレーションによって調べられている。鏃、シャフトそして矢羽の様々な組合せが空力特性に及ぼす影響を解明している。JAXA の Magnetic Suspension and Balance System (MSBS)風洞において、抗力係数(C_D)、揚力係数(C_L)、ピッチングモーメント係数(C_M)を計測した。レイノルズ数 Re$= 1.2 \times 10^4$でのC_D は、直線状の小矢羽をつけた場合には 1.56 であり、大矢羽の場合は 2.05 となる。一方、C_M が表す矢羽の安定化効果は大矢羽の場合が大きくなる。より高いレイノルズ数における飛翔実験では、シャフト内に加速度センサーを挿入して、矢に働く瞬間的な空気力の測定を行った。小矢羽をつけた場合、Re$= 1.8 \times 10^4$では、矢側面の境界層流れが乱流状態から層流状態へ戻ることを示唆する減速率の減少が見られた。また、鏃形状を流線形にすると、椎型の競技用鏃の場合よりも高いレイノルズ数領域まで、層流境界層が形成されることを示した。これらの空力特性に関する知見に基づいて、矢の飛翔軌道と飛翔姿勢を数値計算して、発射条件や背景風の影響を調べた。矢の飛翔中の迎角は発射時の回転角速度に依存し、理想的な回転角速度で放たれた矢にはほとんど迎角がつかず、境界層が層流状態になることが分かった。また、層流状態が保たれると乱流状態の場合に比べて C_D が減少するために、背景風による的ずれが 45% 軽減されることが示された。

Abstract

In this work the aerodynamic properties of archery arrows were studied by means of experimental procedures and numerical simulations. Arrows with different types of shafts, points and vanes were analyzed. From the experiments in the JAXA's Magnetic Suspension and Balance System (MSBS), the drag (C_{D}), pitching moment (C_{M}) and lift (C_{L}) coefficients were obtained. At a Reynolds number Re=1.2×10^4, the values of C_{D} were 1.56 and 2.05 for the short and large straight vanes, respectively. Moreover, a larger stabilizing effect was measured for those arrows using large vanes compared to those ones using smaller vanes. In a second type of experiment, the aerodynamic loads exerted on flying arrows were measured using an acceleration sensor inserted in their shafts. From the data provided by the acceleration sensor, the state of the arrow's boundary layer was inferred. A turbulent-laminar boundary layer transition was found during the arrows' free flight for shots with Re=1.8×10^4. Moreover, by using streamlined points attached to the arrows' front, the boundary layer was confirmed to remain laminar at higher values of Re compared to those arrows using bulge-type points. Further, the trajectory and attitude of the archery arrows were computed under the influence of different background wind conditions. The wind velocities were considered to be uniform, non uniform and similar to those taking place in outdoors archery ranges. Arrows with larger mass showed less deviated trajectories, regardless of the type of background wind. The boundary layer was found to remain laminar along the trajectory by keeping an angle of attack close to zero, which is obtained if the so-called ideal initial conditions can be achieved during the shooting stage. By keeping the boundary layer laminar, the wind drift was reduced around 45% under the influence of a uniform side-wind of 3 ms^{-1}. The computed velocity decay and deceleration in the three spatial components showed good agreement with the experimental data, which validates our mathematical model.

Acknowledgements

I would like to thank all people who contributed to the realization of this research work. First of all my thesis supervisor Prof. Miyazaki Takeshi who gave me strong encouragement, advice and support, and showed me unlimited patience. Without his guidance and love in the pursuit of knowledge this project would had been harder. I also would like to thank my thesis committee members, Prof. Matuttis H.G., Prof. Okawa T., Prof. Chiba K. and Prof. Mamori H. From Kyoto University Prof. Taguchi S., who gave me advice in the early part of my staying in Japan. Among the students in the several stages during my stay in UEC, I would like to thank to Ando R., Matsumoto T., Murayama K., Ando M., Hasegawa T., Serino A., Onoguchi T., Maemukai H., Higashimoto A. and Ito K. Without their hard work and dedication, the realization of the complete research would not have been possible. The support of my friends Komori, Ishikawa, Yamazaki, Toshiki and Saito was invaluable along my staying in UEC. The JUSST program students and friends coming from several nations from which I learned valuable ideas. The endless discussions with my friends Jairo, Edgar, Edgarito, Gibran and Soutarou taught me in several ways. To all of them I feel deeply grateful.

In the UEC staff I would like to express my gratitude to all the people in the International Students Office and in the M Department, for their unlimited orientation and help. Also, I would like to thank Prof. Oku, Prof. Suwako, Prof. Choo, Prof. Shiga and Prof. Ikeda who gave me advice in many occasions. I would like to thank MEXT and the Japanese nation from which I received economic support along the complete research stay and doctoral programs.

From Mexico I would like to thank Prof. Mariko Nakano and all the exchange Mexican students in UEC, who in many occasions listened to me and gave me advice.

I would like to specially thank Muying Chen for having so much patience and consideration with me. She definitely made all these years in Japan happier. Finally, I would like to dedicate this work to my mother, Maria Magdalena Enriquez Ponce, who gave me strength along all this time. Without her love and the support from all my family this project would not have been possible.

Contents

Chapter 1

Introduction

Advances in modern technology have allowed the standardization of products of all kinds in which sports and recreation are not the exception. The advent of computers, new electronic devices and materials concede us the great privilege of living in a time in history where technology plays a fundamental role in the way we live today. Immeasurable examples can be cited. In the present work are utilized modern tools and techniques to study the sporting products, specifically archery arrows.

In recent years the industry around the sports has had an enormous evolution in all senses. The coverage of media, the interest of sponsors and governments and the popularity in the general public has increased in an astounding way in national and international sports competitions, enhancing the flow of resources of all kinds to these events. Take as a good example, the Olympic Winter Games in the Russian city of Sochi in 2014, which set new world records of various types, e.g. to be the most expensive in Olympic Games history in their Summer and Winter versions (around $51 billion) and for the highest dividends from broadcasting rights up to that time [24]. It is evident, in terms of invested money, that such competitions represent an opportunity for determined nations to offer to the world the best qualities of their countries.

Investment in technology also plays an important role in the modern sports events. As proof we could refer to the Summer Olympic Games 2008 held in Beijing. For this competition, the Beijing Olympics Committee developed a so called 'high-tech Olympics' strategy that covered a wide range of areas related with the sporting event. Such areas included internal and external logistics, information services, drug testing and health, equipment, security and others [25]. Focusing in the equipment directly used in the practice of sports, Allen et al. [1] lists a vast of works related with the advance in technology and research in such devices, and his publication works as a good starting point in order to get a view of the kind of research that is being done in sports engineering. The utilization

of high technology in the design, development and test of new products has a prior importance nowadays. In this way, companies assure that the final product will posses the desired characteristics and performance allowing more efficiency, durability and product duration. Equipment in sports activities are not the exception and a common practice today is the usage of hardware and software in the production process that in the recent past years were only utilized for military and heavy industries. Following the overall tendency, the companies related to the archery business are receiving technical support from the different research groups all around the world. Therefore, to make possible high quality research and development of products used in archery competitions, it is necessary the utilization of modern techniques. In the current work, our research group use some available ones. Along the next sections will be listed some of the most relevant research works and approaches related to the study of the dynamics of archery arrows.

1.1 Importance of the consideration of engineering techniques in the design of sporting equipment

Fluid flow over solid bodies is often observed in many technological devices. Sporting equipment is not the exception. Due to such flow, physical phenomena such as the drag force acting on a 100 m sprint runner and the lift developed by an spinning tennis ball arise. Therefore, developing a good understanding of fluid flow interacting with solid bodies is important in the design of modern sporting equipment.

The flow field and geometries found during the design of technological devices in general are too complicated to be carried out analytically, and thus it is necessary to rely on correlations based on experimental data. In modern days, the availability of smaller and high-speed computers made possible to carry on virtual or numerical experiments, specially during the early stages of the product design. In this way, the expensive and time consuming testing and physical experimentation can be limited to the final design stage. Examples of those experiments are the tests carried on in water channels, wind tunnels, etc.

In recent years, the sports engineering became a flourishing research field for physicist and engineers due to the realization of the positive impact of using modern tools and techniques in the design and testing stages of sports equipment. The literature covers a wide range of examples [1] for various disciplines and approaches, including pole vault [10] and projectile disciplines [9, 17], water channel experiments [29] and computational techniques [12, 30]. It is expected that an adequate design and technology selection may reduce errors and improve the per-

formance in the competitions. The latter represents the motivation for our group to carry out a detailed study of archery arrows, in order to understand their dynamics and clarify some of the interesting effects that arise during the shots.

1.2 A first close up to the archery arrows

We may refer to the arrows as such objects that have accompanied the humans on their evolution as a sophisticated animal species on this planet. From the very early times, arrows have been manufactured by humans to hunt and as a warfare device. In the same way, the production of better arrows has marked the difference between the success or failure of different human groups. The ability to create arrows that showed more stable flight or were more resistant to the environmental conditions gave advantages to certain groups of humans over the others. Currently, arrows are mostly used for sports and recreation. Only certain isolated human groups still using arrows or other projectiles as a regular instrument to satisfy their necessity of food and protection.

Take for example the Pirahãs, modern inhabitants of the Amazonian jungle in Brazil. Everett [7] described that even considering that this culture is one the simplest known in the modern world and that they produce and posses very few tools, bows and arrows still among those precious objects that these peoples have. Their powerful bows are longer than 1.8 m and their arrows reach between 1.8 and 2.7 m in length. Such arrows take approximately three hours to make and their physical characteristics vary according to the purpose they are designed for. If the arrows were used to hunt monkeys or fish, the points would be made from sharpened hardwood or a narrow piece of bone, respectively. If the arrows were used in their sporting competitions, the points would be made from bamboo. The fletching of such arrows is made using feathers from local birds, attached to the end of the arrows using cotton. Everett explicitly describes the arrows' efficiency: *I have seen wild pigs skewered by these arrows- entering near the rectum and protruding out the throat*. From this testimony is possible to learn that the Pirahãs posses a deep knowledge of the vital importance of the arrows' basic components in their performance.

Some other historical testimonies available in the literature result of interest regarding to the advantages of constructing archery arrows with the appropriate physical properties. Take the testimony written in 1545 by Roger Ascham [2], in which is stated that the *greatest enemy of shooting is the wind and the weather* and that *weak bows and light shafts cannot stand in a rough wind*. From the latter testimonies is possible to learn the very old realization of the importance that the materials used to manufacture the arrows determine their behaviour when shot in the regular outdoors conditions.

Nevertheless, there exists a remarkable evolution from the non-expensive wood-made English longbow to the ultra modern bows. Despite the simplicity of the English bows, considerable effort and skill was required during their construction, as noted by Denny [3]. Such bows had a length of 1.8 m and a shooting range of between 160 and 220 m. It is of interest to know that archers using such a bow were able to shoot around 12 arrows per minute. The efficiency of such a bow was of around 70% to 80%. The efficiency value is a measure between the energy invested by the archer to draw back the bowstring and the energy transferred to the arrow. Modern bows have an efficiency of around 90%.

1.3 Generalities of the modern archery arrows

Arrows are thin, elongated, light and flexible cylindrical bodies with rotation and flexural movements along them, resulting in high complexity in terms of characterization and study. The arrows shot using a recurve bow are expected to stay in the air less than 2 s in a 70 m archery field and move at an average velocity of 60 ms^{-1}. Such a small time span and high velocity increase the difficulty when studying these projectiles in detail.

The archery competition is a shooting discipline in which the accuracy and precision are key factors in order to obtain a good final score. In the competitions using a recurve bow, the archers aim at a target with 1.22 m in diameter and located 70 m away. The target is divided into 10 smaller evenly spaced concentric circles, rings. The innermost of the rings has a diameter of 0.122 m and is assigned with the maximum of 10 points. The archers shoot a specified number of arrows and the archer who sums more points wins the competition. Striking the innermost ring gives the opportunity to increase the final score. This task is easy to describe but if we take a look closer and consider the multiple elements affecting the shots, difficulties arise.

The movement of an arrow is described by six degrees of freedom: linear motion along each of the three directions (x, y and z) and rotational motion about each of these axes. Further, with the recent availability of high-speed video cameras the experimentalist were able to find that the arrows show another interesting movement en route to the archery target: flexural oscillation. This movements is a snake-like movement that the arrow shows due to its flexibility. Note that the actual arrows are not strictly rigid bodies. Such movement arises from the interaction between the arrow and the bowstring. During the shooting stage, the bowstring exerts a load in the flexible arrow that forces it to modify its shape, arising the characteristic flexural oscillation. The rate of longitudinal bending of an arrow depends upon the arrow shaft characteristics. It also has been observed that the flexural oscillation is highly reduced when the arrows are shot using com-

pound bows.

In the following sections are briefly explained some of the most relevant works related with the study of the modern commercial arrows, with the objective to grasp in a better way the state of the art and the techniques that are being used to improve the arrows' design.

1.4 Influence of the Arrows' center of pressure and center of gravity position

An important aspect to consider when discussing the stability of projectiles is the position of their center of pressure *c.p.* and the center of gravity *c.g.* When the position of the *c.p.* is ahead of *c.g.* stability reigns. Take for example bullets who have their *c.p.* very close to their *c.g.* due to their reduced size and mass distribution. Therefore, a bullet is by itself aerodynamically unstable. To achieve an stable flight, the engineers were forced to impart spin to the bullet before it leaves the gun's muzzle. Contrary, the archery arrows are very stable projectiles. Their *c.p.* is located well in the rear part, near the fletched vanes [23]. The influence of the lift force on the vanes induces a corresponding pitching moment that stabilizes the arrow's attitude during their trajectory.

Another interesting example to consider is the javelin throw. Even though archery and javelin throw differ in many aspects, the javelins are subject to the same aerodynamic loads as the archery arrows and serve us to remark some important physical characteristics. Javelins are long spears with a mass of around 0.80 kg and a fineness ratio $f = 80$. The fineness ratio is the relation between the projectile's length and its diameter $f = l/d$. The initial launching velocity for javelins is in average 30 ms^{-1}. While studying the dynamics of flying javelins, Hubbard [12, 13] found that these devices develop relatively large angles of attack during their flight, in the order of around 35°, leading to large lift forces necessary to increase the range that would make the thrower to get a high score in the competition. Such values of the angle of attack also induce an important drag component that leads to less precise shots (in the javelin throw, precision is not so relevant as in the archery competition).

An important difference between the aerodynamics of arrows and javelins is the position of their corresponding *c.p.* and *c.g.* In javelins, *c.p.* is found very close to *c.g.*, at around 8.0×10^{-3} m [12]. Whereas in the case of the arrows, *c.g.* is located in the front part while *c.p.* in the tail, having a distance of around 0.40 m between them. The fact that *c.p.* and *c.g.* are very close represents an absence of pitching moment in the javelin's flight. Therefore, no counterbalance effect to the increasing angle of attack takes place. The growing magnitude of the

angle of attack allows to generate large values of lift and drag forces. In contrast, the maximum value of the angle of attack computed by Miyazaki et al. [22] in arrows in free flight, under no wind conditions, is around 0.40°. This small angle of attack is a product of the pitching moment-lift force balance effect. Such small angle of attack generates smaller drag force and drift in an arrow than in a javelin, allowing precise shots.

1.5 Air flow around an archery arrow's point

During an archery arrow's flight, the arrow aligns itself with the vector sum of its forward velocity and the wind velocity en route to the target. Therefore, the drag has a lateral component due to such alignment which provokes a lateral displacement of the arrow. This displacement is known as *wind drift*. In order to reduce the wind drift, a higher initial velocity and reduced drag are both desirable. It must be considered that a major proportion of the drag is due to the drag exerted on the arrow's shaft. Therefore the selection of the proper shaft is important to reduce undesired arrow's movements. To grasp in detail the mechanism under which the wind drift occurs, the study of the wind flow characteristics must be considered in detail. It is recognized that the airflow along the arrow's shaft is initially laminar and then, a short distance along the shaft, transition to turbulent flow occurs. The magnitude of the drag is known to change significantly depending upon the position of the transition to turbulent regime. To study in detail the latter, Park et al. [29] performed experiments in a water channel to study the flow of water around the point of a model archery arrow. The diameter of the arrow's point was scaled to 16:1.

In their study, Park et al. analysed two points with different shapes, i.e. *bullet* and *bulge* points. On the one hand, the maximum diameter of the bullet point is equal to the diameter of the arrow shaft. On the other hand, the bulge point has a maximum diameter a slightly larger than the arrow shaft. Some of the more relevant findings are listed below:

- When the bullet point was used and the angle of attack was set to zero at Re= 3.43×10^4 (using the diameter of the shaft as the characteristic length), the flow around the arrow's point was found to be laminar. The transition to turbulent state occurred at around 1 m downstream from the point of the arrow's model. In an actual commercial arrow, which is shorter than its model, the transition would happen at around 0.06 m downstream from the point (around 10 % of its total length).

- In the case of the bulge point at Re=6.92×10^3, laminar flow along the whole point was found. At Re = 2.41×10^4 there existed flow separation

in the area of maximum diameter of the point but immediate reattachment and therefore laminar flow along the shaft. When Re =2.74 $\times$ 10^4, there existed flow separation just after the area of the point with maximum diameter and the recirculation position was found to be in the rear taper of the point, where the point and the shaft joint. Downstream the rear end of the recirculation area the flow was found to be turbulent at such Re.

- At Re = 3.43 $\times$ 10^4 the flow was turbulent from the taper near the joint with the shaft for $|\gamma| < 3.0°$.

It is observed that the state of fluid flow around an arrow varies with the Re values and arrow's attitude. The complete determination of the fluid flow characteristics is not a straightforward task due to nature of the transition phenomena that makes the experimental procedures time consuming and expensive. The importance of the state of the fluid flow in the dynamics of the archery arrows will be analysed in Chapters 5 and 6.

1.6 Influence of arrows' mass in the trajectory computations

Recently Kuch et al. [19] computed the trajectories of commercial arrows with different masses under still air conditions. The still air conditions refer to the case when the effect of the background wind in the trajectory of the arrows is considered to be negligible. However, the interaction between the arrows and the surrounding air stills generating aerodynamic loads on the arrows. Such effects are reflected in the drag force and lift and pitching moments.

Kuch et al. obtained a correlation between the mass and the vertical deviation when the arrows strike a target located 70 m away from the shooting position. The arrows were Easton X10 arrows with different stiffness. In their work, no details are given on the effect that the different arrows' mechanical properties (like stiffness) on the computed trajectories. Further, in their study a constant laminar value of the drag coefficient, C_D =1.5, was considered, which might not be the best choice for arrows shot with recurve bows. The initial arrow's velocity considered in their computations was around 62 ms^{-1}, which under regular conditions would correspond to a turbulent boundary layer regime. This would increase by at least a factor of two the magnitude of C_D (see Chapter 5). Further, the values of C_D change along the arrows' trajectories and depend upon the flow characteristics, as will be shown in Chapter 6. Kuch et al. showed that heavier arrows experienced larger vertical deviations from the center of the target, as expected.

1.7 Measuring the velocity and acceleration using miniaturized sensors

In the previous section, it was discussed that the influence of the mass is an important factor in determining the trajectory of the arrows in free flight. Nevertheless, Kuch et al. considered a constant value of the drag coefficient C_D in their computations also. It is known that velocity decays as the arrow travels downrange and therefore the drag, which is proportional the square of the velocity. Such variation in the drag must be considered in any attempt to study the dynamics of archery arrows. Due to the latter, recently, Barton et al. [4, 5] designed and tested a miniaturized measurement system (with a diameter of 9×10^{-3} m and 40×10^{-3} m in length) and mounted it on hunting arrows to measure the downrange evolution of the velocity and the deceleration. The masses of the sensor and the arrows were 6.5 g and 18 g, respectively. Arrows were shot with crossbows, which allow larger initial velocities than the recurve bows considered in the present study.

From their experiments, the launching and impact velocities were obtained for arrows using two types of broad-heads with different shape. The kinetic energy, flying time and averaged drag were extracted from the experimental results. From the knowledge of the retained energy it was possible to obtain the aerodynamic efficiency of the tested arrows.

We believe that by measuring precisely the time dependant aerodynamic forces exerted on the arrows during free flight, it would be possible to better elucidate the characteristics of the surrounding fluid flow.

1.8 Computation of arrows' trajectories with drag and without drag

It has been previously mentioned that the aerodynamic loads exerted on the arrows determine their downrange trajectory. Figure 1.1 shows two trajectories of arrows where the drag force was neglected (solid line) and regular drag force was considered (broken line). Such results correspond to numerical computations (for details of the numerical simulations, see Chapter 4). Note that in an archery range of 70 m, the final striking positions differ in 0.87 m, which is not a negligible distance considering that the archery competition is a precision sports. In order to carry out an accurate and realistic analysis of the dynamics of archery arrows, the aerodynamic loads must be taken into account.

Therefore, the numerical computations carried out in the current work gives us valuable and realistic information only if the aerodynamic properties of actual commercial arrows are taken into account. In Chapter 5 those aerodynamic

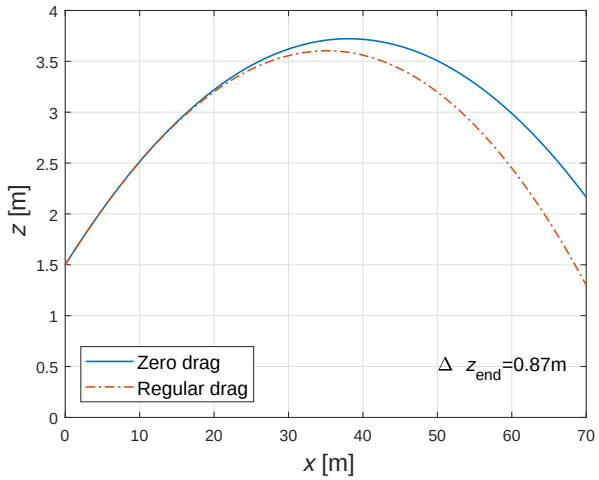

Figure 1.1: Comparison in the trajectory of an arrow with regular and zero drag in an archery range of 70 m with an initial velocity $V_0 = 57$ ms^{-1}.

properties for several commercial archery arrows are shown.

1.9 Influence of the environmental conditions in the arrows' dynamics

An important factor that has to be considered in the study of any sports that is performed outdoors is the influence of the background wind. In case of archery competitions, it has been referred to as one of the most important elements disturbing the archers and their shots [32, 31]. Park [30] has studied the effect that side wind gusts have in the lateral displacement, wind drift, of arrows shot from a compound bow. He reported that in an outdoors archery range with a maximum distance of 70 m, a wind drift of around 0.18 m would not be rare considering a uniform side-wind of 3 ms^{-1}. The concept of uniform side-wind refers to wind blowing from the lateral side of the flying arrows. Such theoretical wind is considered to remain constant along the whole arrow's trajectory. Its direction is also considered to remain unchanged. A lateral deviation of 0.18 m in the arrow's trajectory may not be negligible in the major archery competitions, marking the difference between winning or not the archery ranking round.

Since the archery ranges for major competitions are located outdoors, the influence of the changing wind gusts on the arrows' trajectories is important. Therefore, in the current work we study the response of several types of arrows to such background wind effects. Different types of background winds, for which the ve-

locities and directions remain constant and vary along the arrows' trajectories are considered in the computation of the equations of arrow motion. The details of the background wind are explained in Chapter 4).

1.10 Further studies related to the influence of the environmental conditions on the sporting competitions

The environmental conditions have been proved to be determinant for the sports performance and therefore of interest for several research groups. Jung et al. [15] studied the effect of the background wind in the maximum range that can be travelled in the ski jumping competition. Head- and tail-winds were considered during the trajectory of the athletes. Nevertheless, cross-winds were not taken into account, which provides limited conclusions. Winds in real outdoor conditions are expected to change speed and direction during the few seconds that last the flight of the jumpers. Therefore, the influence of the cross-winds cannot be neglected to achieve a realistic aerodynamic analysis. Likewise, such crosswinds must be taken into consideration while analysing the trajectory of archery arrows. Jung et al. also remarked the difficulty to carry out wind tunnel measurements for changing-wind conditions, which is a limitation that we also faced during our wind tunnel tests.

Hoof et al.[11] carried out CFD simulations to study the influence of the stadium geometry on the wind flow and wind-driven rain (WDR) patterns. The main objective of their work was to determine which stadium configuration would provoke that more percentage of the sitting area would get wet in a WDR scenario. The several analysed stadium configurations covered different types of roofs and different stand arrangements. The results showed that the stadium's shape is a factor that cannot be neglected during the design and construction stages.

Hoof et al. found that in a horizontal plane located at a heigh of 1 m above the ground, the time averaged wind velocity ranges from around 0.4 ms^{-1} to 5.6 ms^{-1} for an stadium with two sets of stand arrangements located only in the long edges and a flat roof. In the case of an enclosed rectangular stadium, the wind velocity ranged from around 0.4 ms^{-1} to 3.6 ms^{-1}. Such changes in the wind velocity are not negligible and affects in an important way the performance of the sports equipment and the competitors themselves. Further, the wind direction also resulted highly affected by the stadium configuration. Since the arrow competition is carried out almost at the ground level, the latter considerations must be taken into account.

In recent years, the regulations regarding to stadium construction have in-

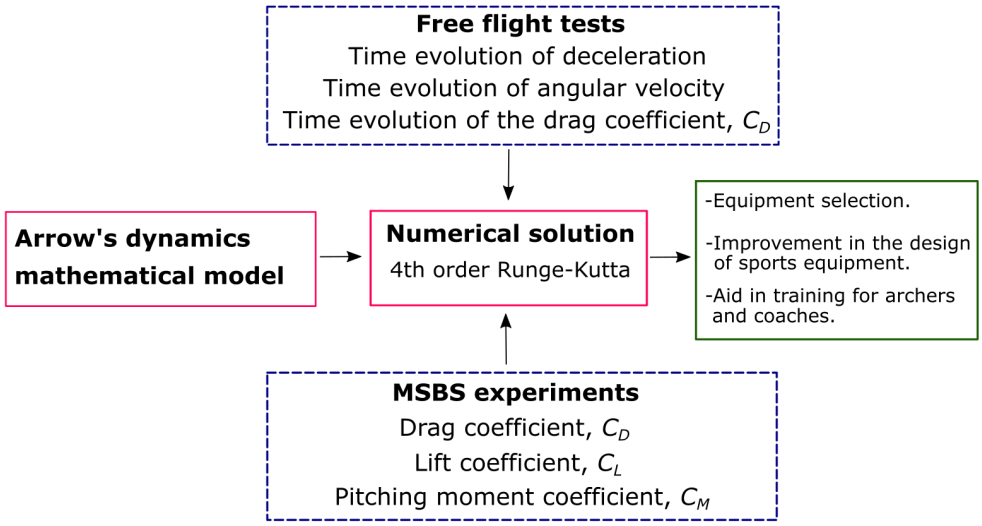

Figure 1.2: Basic research overview. Two types of experiments (Free flight experiments and MSBS tests) were used to obtain the aerodynamic characteristics of several commercial archery arrows. Using such properties we computed numerically the equations of arrow motion to study in detail the response of several arrows configurations.

creased their standards and specifications. During the contemporary stadium design, the percentage of the seats that remain dry under difficult environmental conditions during rain or snow is an important specification. The theoretical and computational studies regarding the shape and orientation of sporting stadiums is an example of how the new tools and technologies are used to improve the future architecture in sporting structures.

1.11 General overview of the current work

In the previous sections, we offered an introduction to some of the relevant works related with our investigation to remark the important points to be considered when studying the dynamics of archery arrows. Figure 1.2 shows a general representation of the work carried out in the current research project. Since we are interested in giving realistic results that may aid in the equipment selection and improve the design of archery arrows, we measured the physical and aerodynamic characteristics of several types of commercial arrows. The description of the arrows' physical characteristics are given in Chapter 2.

We carried out two types of experiments to determine the aerodynamic characteristics of the archery arrows. The first of the experiments was performed by

shooting arrows in an indoor archery range. The trajectories of the arrows were recorded from the side using several high-speed video cameras that were located at the beginning and at the end of the arrows' flights. From the analysis of the video recordings, it was possible to obtain the initial and final conditions of the shots. An acceleration sensor was introduced in the arrow's shaft allowing us to measure the exerted force and angular velocity in the three spatial components. The second type of experiments were carried out in the JAXA's Magnetic Suspension and Balance System (MSBS). The details about the experimental configurations are given in Chapter 3.

Further, we proposed a mathematical model that describes accurately the attitude and trajectory of the flying arrows using the equations of motion for a rigid body. Such mathematical model is complicated, making necessary to solve the equations of arrow motion using a numerical scheme (4th order Runge-Kutta method). The obtained experimental data that describe the actual arrows' characteristics was used as input in our mathematical model to test the arrows' response to several operation conditions. In the numerical computations the effect of the background wind in the trajectories of the arrows was considered.

By using the actual arrows' properties, we can study and compare different arrows' configurations, which may contribute to the improvement of the current technology and possibly aid in the training of archers and couches. The equations of arrow motion are given in Chapter 4. The results from the experimental tests are explained in Chapter 5. The initial conditions, background wind descriptions and results from the numerical simulations are given in Chapter 6. Lastly, a summary of the main findings, conclusions and future work are given in Chapter 7.

Chapter 2

Arrow's description

The modern archery arrows are slender, thin, flexible and elongated bodies constructed basically with 4 elements: shaft, point, vanes and nock (Figure 2.1). An arrow is a projectile in which the point is attached at the leading edge of the shaft. The vanes or stabilizing fins are located at the rear part of the arrow. The nock is attached at the very end of the arrow to fix it tightly in contact with the bowstring. There exist available in the market various types of those components, each of them with different characteristics that offer to the archers the option to choose their preferred configuration [6]. In the current chapter, the arrows' components studied in this work are described.

We investigate the influence of the different physical properties of the arrows in the flying dynamics, considering several arrow configurations. Two types of shafts (A/C/E and X10), four types of vanes (curved SWV, curved GPV, straight short and straight large) and two types of points (bulge-type and streamlined) were studied in detail. In order to achieve larger values of the Reynolds number in the MSBS, we constructed a model of the X10 arrow and kept an identical fineness ratio, f. In the following sections the detailed descriptions of every component of the arrows are given.

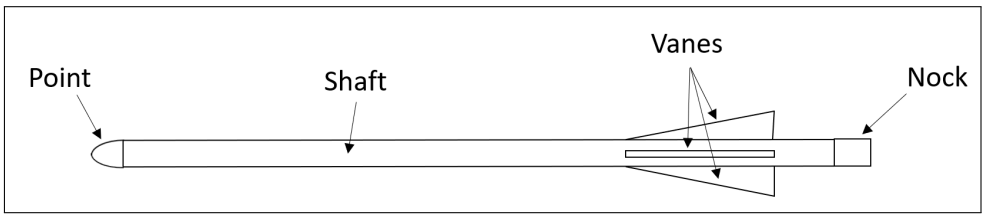

Figure 2.1: Basic components of an archery arrows: point, shaft, vanes and a nock.

2.1 Basic aerodynamic forces exerted on the arrows

Since the flying arrows are bodies that are immersed in a fluid, air, the interactions between their bodies and the surrounding air result in aerodynamic forces. Our discussion will be focused on the aerodynamic forces, i.e. the lift and drag. Other effects such as the Magnus effects are not considered in the current work. In an external flow, the viscous effects are confined to a portion of the flow field, such as the boundary layer, which is surrounded by an outer flow with small velocity gradients.

When a fluid moves over the archery arrows, it exerts pressure and shear forces that act in the normal and parallel directions of the arrows' bodies. In our discussion we are interested in the resultant of the pressure and shear forces acting on the flying arrows rather than the details of the distributions of these forces along the entire arrow's body. The component of the resultant pressure and shear forces along the flow direction is called the drag force (F_{D}) and is given by

$$F_{\mathrm{D}} = \frac{1}{2} C_{\mathrm{D}} \rho A V^2, \tag{2.1}$$

where C_{D} is the dimensionless drag coefficient, A is the arrow's cross-sectional area and V is the arrow's velocity. The drag force is exerted in the opposite direction to the arrow's velocity. The air's density is ρ=1.225 kgm^{-3} at 15 °C at sea level. Whereas the component that acts normal to the flow direction is called the lift force (F_{L}) and is given by

$$F_{\mathrm{L}} = \frac{1}{2} C_{\mathrm{L}} \rho A V^2, \tag{2.2}$$

where C_{L} is the dimensionless lift coefficient. Like C_{D}, the lift coefficient is a factor that contains the particular characteristics of the arrows. It depends on the arrow's velocity, spin rate and surface characteristics. Another important aerodynamic factor is the pitching moment τ_M. The pitching moment arises when the aerodynamic center, or center of pressure, is located at a different position from the center of gravity and is given by

$$\tau_M = \frac{1}{2} C_{\mathrm{M}} \rho A l V^2, \tag{2.3}$$

where C_{M} is the dimensionless pitching moment coefficient and l is the arrow's length. When discussing about fluid dynamics, we regularly encounter the dimensionless parameter Reynolds number, Re, which provides an estimate of the

relation between inertia and viscosity in any fluid flow. Its value can be computed with

$$\mathrm{Re} = \frac{VD}{\nu}, \tag{2.4}$$

where ν is the air's kinematic viscosity and D is the characteristic length. Along the current work, the characteristic length is the arrow's mean diameter, d. Due to the arrows rotate along their axis, it is necessary to introduce the dimensionless spin parameter, which relates an arrow's velocity and spinning rate by

$$S_P = \frac{r\omega_3}{V}, \tag{2.5}$$

where $r = d/2$ is the arrow's mean radius and ω_3 is the rotation rate in the arrow's axial direction.

2.2 Shaft description

The modern arrows' shaft are constructed from a carbon fibre sheet wrapped around an aluminium alloy tubular core. We focus our research on two main types of shafts, the commercial Easton A/C/E and Easton X10. The shafts' radius changes slightly along their complete length as shown in Figure 2.2. The maximum diameter for the A/C/E and the X10 shafts are 5.39×10^{-3} m and 4.97×10^{-3} m respectively. Whereas the minimum diameter for the A/C/E and the X10 shafts are 5.07×10^{-3} m and 4.45×10^{-3} m respectively. Throughout the current work we consider in all the calculations the arithmetic mean of the diameter and the radius and simply call them diameter (d) and radius (r). The length of the bare shafts is 0.626 m for both types. Observe the larger mean diameter of the A/C/E shaft in Figure 2.3. The complete physical characteristics of the shafts are summarized in Table 2.1. Hereafter, we will refer to both arrow configurations as the A/C/E arrow and the X10 arrow. Figure 2.4 shows the A/C/E and the X10 arrows.

2.3 Points description

The type of point used in every arrow is defined by the type of activity that is being carried out, ranging from target practice to hunting. The points are available in numerous shapes and weights. Each of them designed for a specific purpose. In the current work, two types of points used in sporting arrows are studied. The first of

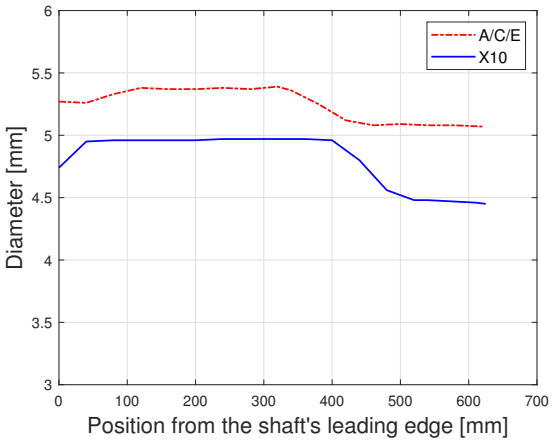

Figure 2.2: Variation of the shafts' diameter along the length.

Table 2.1: Physical characteristics of the A/C/E and X10 shafts.

Shaft	**Length [m]**	**Mean diameter [m]**	**Mass [kg]**	**Fineness ratio**
A/C/E	0.626	5.24×10^{-3}	1.20×10^{-2}	118.5
X10	0.626	4.82×10^{-3}	1.18×10^{-2}	129.9
X10 (model)	1.03	7.92×10^{-3}	2.66×10^{-2}	129.9

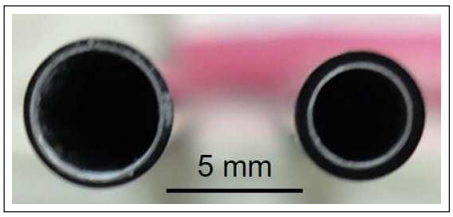

Figure 2.3: Cross-sectional view of the an arrow using A/C/E shaft in the left and an arrow using the X10 shaft in the right.

Figure 2.4: Arrows using the two types of shafts, in the upper part an arrow using the A/C/E shaft. In the lower part an arrow using the X10 shaft. Both arrows using the curved SWV vanes.

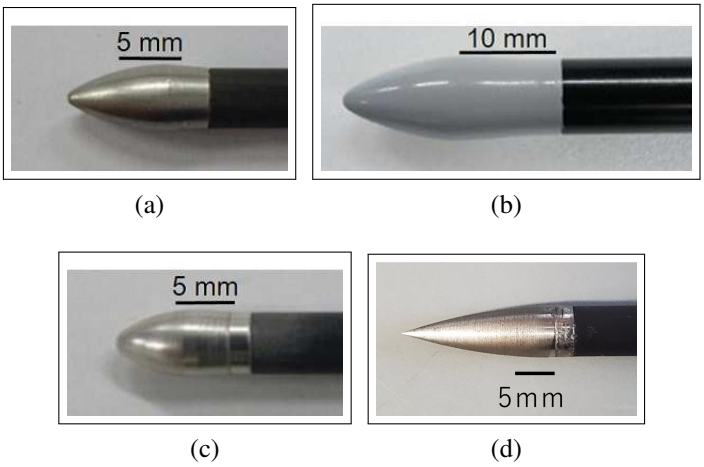

(a) (b) (c) (d)

Figure 2.5: Different arrow points used of the type a) X10, b) X10 (arrow's model) c) A/C/E and d) Streamlined.

Table 2.2: Physical characteristics of the considered points.

Type of point	**Length [m]**	**Maximum diameter [m]**	**Mass [kg]**
A/C/E	10.7×10^{-3}	5.92×10^{-3}	2.01×10^{-3}
X10	11.5×10^{-3}	5.31×10^{-3}	7.76×10^{-3}
X10 (model)	11.5×10^{-3}	8.0×10^{-3}	2.83×10^{-3}
Streamlined	17.6×10^{-3}	5.44×10^{-3}	2.59×10^{-3}

them is denoted as the bulge-type point (Figure 2.5a, Figure 2.5b and Figure 2.5c), for which one of the main characteristics is that its maximum diameter is slightly larger that the shaft's diameter. The bulge-type points are commonly selected in order to easily withdraw the arrows from the target and to minimize damage in the arrows' front produced by the impact. The second type of point considered is the streamlined point (Figure 2.5d). As its name suggests, it has a streamlined shape to retard the flow separation and therefore the laminar-turbulent transition of the boundary layer. The complete physical characteristics of the points are summarized in Table 2.2.

2.4 Vanes description

The vanes or fletching work as aerodynamic stabilization devices attached to the arrows' rear part. They are commonly constructed from light and semi-flexible materials. The modern vanes are typically made from plastics, which offer re-

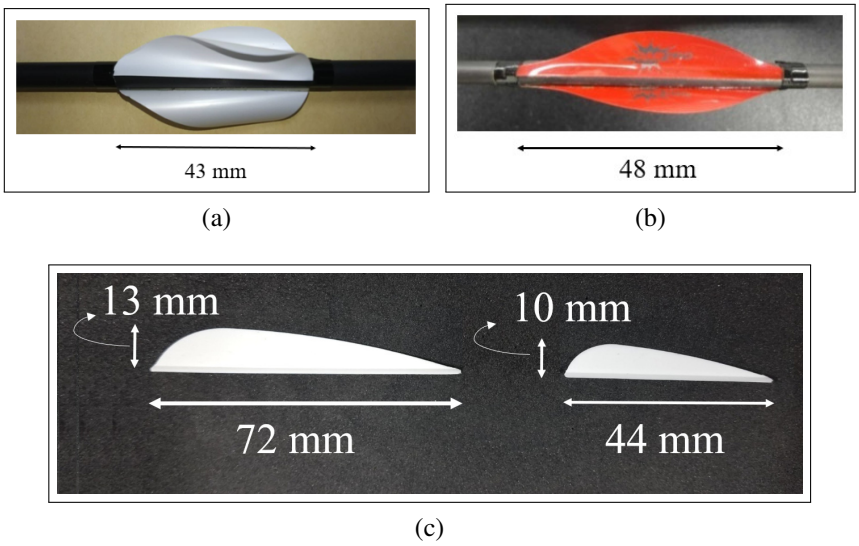

(a) (b)

(c)

Figure 2.6: The four types of vanes considered in the current study, a) Sping Wing Vanes (SWV), b) Gas Pro Vanes (GPV) and c) Straight large vanes (left) and Straight short vanes (right).

sistance and flexibility at the same time. Usually three vanes are attached to the archery arrows for stabilization. There are several types of commercial vanes available in the market [6]. In this work we analysed the response of arrows using curved (Figure 2.6a and Figure 2.6b) and straight vanes (Figure 2.6c). The selected curved vanes were the Range-O-Matic Archery Company's SPIN-WING-VANES (SWV) and the Disegna Sports Distribution's Gas Pro Vanes (GPV). Whereas the straight vanes were the Easton Diamond Vanes with two sizes (size 175 and size 280), for which the area is different. Hereafter we refer to them as short straight vanes and large straight vanes, respectively, for simplicity. Fletching the arrows with the straight vanes will produce little spin around the arrow's axis during free flight, whereas the curved vanes produce larger rotation rates. In Table 2.3 are given the complete physical characteristics of the vanes.

2.5 Computation of the moments of inertia, I and I_3

Due to the different arrow components in every configuration, all the studied arrows posses different physical characteristics. Two important physical characteristics that must be taken into account in every study related to the arrows' dynamics are the moments of inertia. In the current section we specify the way in which the moment of inertial around the center of mass I and the moment of inertia around

Table 2.3: Physical characteristics of the considered vanes.

Type of vanes	**Length [m]**	**Total area [m^2]**	**Mass [kg]**
SWV	4.45×10^{-2}	1.29×10^{-3}	0.15×10^{-3}
GPV	5.50×10^{-2}	0.97×10^{-3}	0.21×10^{-3}
Large straight	7.20×10^{-2}	1.96×10^{-3}	1.66×10^{-3}
Short straight	4.40×10^{-2}	0.93×10^{-3}	0.60×10^{-3}

Note: The total area and mass specified in this table correspond to the total of the three vanes.

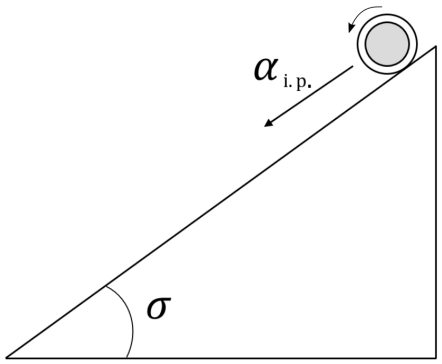

Figure 2.7: Illustration of the relevant variables to determine the moment of inertia (I_3) along the arrow's axis.

the arrow's axis I_3 are obtained.

In order to compute I, there must be considered the masses and lengths of each of the arrow's components individually. As for the case of I_3, its value was determined experimentally through a simple experiment in which the arrows were freely rolled in an inclined plane with fixed angle σ (Figure 2.7). The free rolling was recorded with a high speed video camera. From the video recordings is possible to obtain the arrow's velocity and acceleration ($\alpha_{\text{i.p.}}$). The value of I_3 can be determined by,

$$I_3 = Mr^2 \left(\frac{g \sin\sigma}{\alpha_{\text{i.p.}}} - 1 \right), \tag{2.6}$$

where M is the arrow's total mass, r its radius and g=9.81 ms^{-2} is the gravitational acceleration.

Table 2.4: Physical properties of the different arrow configurations considered in the current study.

Shaft/ Point/ Vanes	**Diameter [m]**	**Length [m]**	**Mass [kg]**	$c.g.$ **[m]**
X10 / Bulge / SWV	4.82×10^{-3}	0.637	0.0197	0.19
A/C/E / Bulge / SWV	5.24×10^{-3}	0.636	0.0143	0.21
A/C/E / Bulge / GPV	5.24×10^{-3}	0.636	0.0144	0.21
A/C/E / Bulge / Str. short	5.24×10^{-3}	0.636	0.0143	0.24
A/C/E / Bulge / Str. large	5.24×10^{-3}	0.636	0.0154	0.26
A/C/E / Stream. / Str. short	5.24×10^{-3}	0.638	0.0148	0.26

Note: The $c.g.$ is measured from the front part of the arrow's point.

2.6 Summary of the physical properties for every arrow configuration

Table 2.4 summarizes the physical properties of the six different arrow configurations studied in the current work. The type of shaft, point and vanes are specified in the first column. The second and third columns correspond to the mean diameter (d) and the total length (l) or the arrows. Whereas the total mass (M), considering the point, shaft and vanes are given in the fourth column. The last column corresponds to the position of the center of gravity ($c.g.$) measured from the frontal part of the arrow's point.

Chapter 3

Experimental apparatus

In this chapter the details of the two support-interference-free experiments are described. We had to measure accurately the aerodynamic properties of the arrows described in Chapter 2. All the described arrow configurations are taken into account. The two types of experiments are the wind tunnel procedures in the JAXA's MSBS (Section 3.1) and the free flight tests (Section 3.2).

3.1 Description of the MSBS tests

JAXA's 60 cm $\times$ 60 cm Magnetic Suspension and Balance System (MSBS) is a wind tunnel that allowed us to suspend magnetically against gravity the thin arrows, as shown in Figure 3.1. The arrows are suspended using a magnetic field generated by an array of 10 coils located around the wind tunnel. When the wind flow is turned on, the magnetic field is automatically adjusted to balance the arrows in a fixed position against the aerodynamic forces and the gravity. The orientation of the arrow with the wind flow, attitude, can be adjusted arbitrarily. In our experiments, a maximum angle of attack of $|\gamma| < 3.0^\circ$ was set. To successfully generate the magnetic field to suspend the arrows, 10 cylindrical neodymium magnets with a diameter of 4×10^{-3} m and and length of 30×10^{-3} m are inserted inside the arrows' shaft.

From the MSBS tests, it is possible to obtain the values of the drag (C_D), lift (C_L) and pitching moment (C_M) coefficients for the different arrows' configurations. In the case of the X10, a model of the arrow (Figure 3.2) was constructed to reach higher values of the Reynolds number, Re. Throughout the current work, the arrows' mean diameter is used to compute the value of the Reynolds number with Re=$2rU/\nu$, where r is the arrow's mean radius, U is the wind's velocity and ν is the air's kinematic viscosity at room temperature. The wind velocity range in the MSBS is 8 ms$^{-1} < U <$ 45 ms^{-1} with a fluctuation of 0.06% at 30 ms^{-1}. The

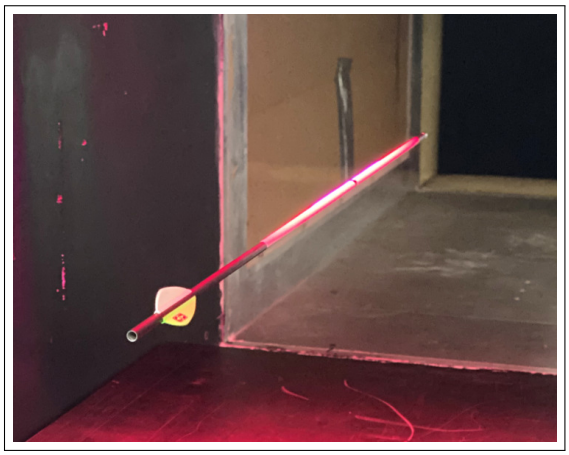

Figure 3.1: Magnetically suspended arrow using straight vanes in the MSBS.

maximum Reynolds number obtained using the actual arrows was Re$< 1.5 \times 10^4$. Whereas by using the X10 model it was possible to extend the measurements up to Re$= 2.0 \times 10^4$. The response time of the feedback measuring circuit is around 500 Hz, which allows high precision in the measurement of the aerodynamic characteristics.

3.2 Description of the free flight tests

For the free flight tests, five different high-speed video cameras were used to record the trajectory of flying arrows and from the video images we extracted several numerical parameters such as arrow's initial launching velocity, angular velocity and the initial angle of attack. It is possible to obtain the the horizontal and vertical velocity components of the arrows at two points, 55 m apart, and from them calculate the drag coefficient C_D. The detailed procedure is explained in the work by Miyazaki et al. [23].

In the free flight tests, arrows were shot using a compressed air launching system and their trajectories were recorded using several high-speed video cameras. The experiments were carried out in three different indoor archery ranges: at the Japan Institute for Sport Sciences (JISS), at the gymnasium of Edogawa Ward and at the laboratory of The University of Electro-Communications (UEC); with 65 m, 55 m and 17.7 m, respectively (Figure 3.3). In all of them, the trajectory and rotation of the arrows were recorded with several high-speed video cameras located in different positions of the trajectory. Every air conditioning system was turned off to minimize the influence of the background wind and to avoid unexpected wind gusts. The layout of the free flight tests, the position of the cameras

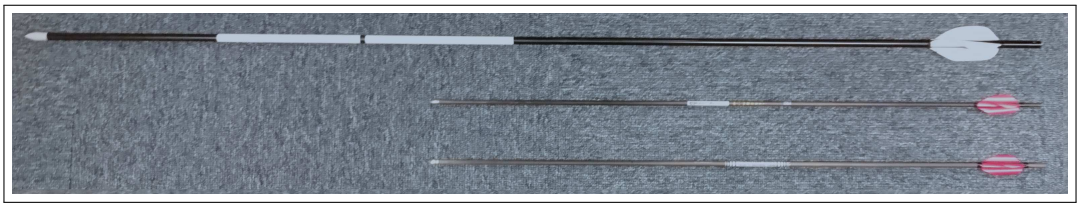

(a)

(b)

Figure 3.2: a) Comparison of the actual arrows with the X10 arrow's model. In the upper part is shown the X10 model, in the middle and inferior parts are shown the actual X10 and A/C/E, respectively and b) the magnetically suspended X10 arrow model in the MSBS.

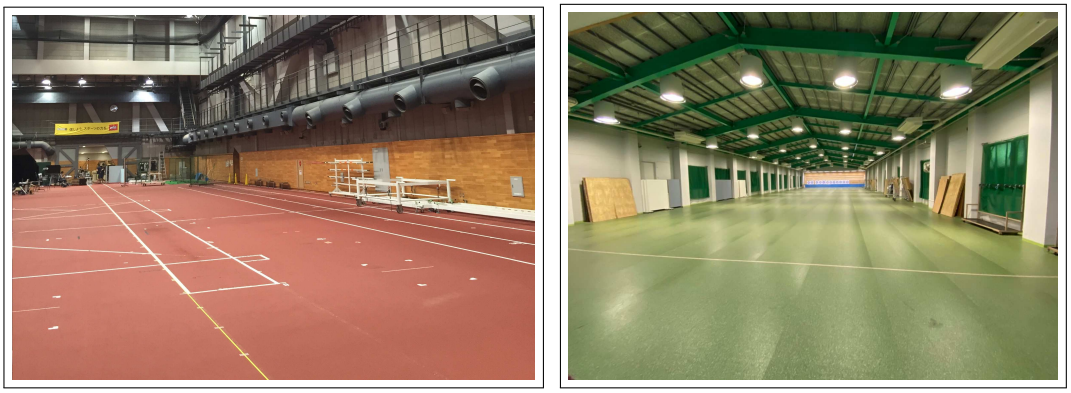

(a) (b)

(c)

Figure 3.3: Three different indoors archery ranges in which the free flight test were carried out. a) Long archery range at JISS of 65 m, b) Long archery range in Edogawa of 55 m and c) Short archery range in UEC of 17.7 m.

and the corresponding distances are shown in Figure 3.4.

The launching system is a canyon-type device which uses compressed air to propel the arrows without nock at any determined initial velocity, V_0. The arrows were located in position by introducing them in the launching device's nozzle (Figure 3.5). High repeatability can be achieved in the initial velocity of the arrows by adjusting the air's pressure. An arrow shot using this device translates and rotates as a rigid body, not showing the flexural oscillation that otherwise would experience if shot by a real archer. Later, it will be shown that this characteristic greatly simplifies the mathematical modelling of the arrows in free flight.

In Tables 3.1 and 3.2 are shown the cameras that were used in the experiments in the large archery ranges at JISS and Edogawa, respectively. For the experiments in the short archery range in UEC uniquely the Phantom LC310 was used.

Table 3.1: Used cameras in the 65 m at JISS with their characteristics.

Type of camera	**Position**	**Pixels**
Photron SA2	Camera 1	1920 ×1080
Photron SA2	Camera 2	1920 ×1080
Phantom v311	Camera 3	1280×720
Phantom v710	Camera 4	1280 ×720

Table 3.2: Used cameras in the 55 m at Edogawa with their characteristics.

Type of camera	**Position**	**Pixels**
Phantom LC310	Camera 1	1280 × 800
Phantom v2640	Camera 2	1920 ×1080
Phantom LC310	Camera 3	1280 ×1080
Phantom v710	Camera 4	1280 ×720

3.2.1 Acceleration sensor description

The acceleration sensor used during the free flight experiments allows us to measure the deceleration and the angular velocity in the three spatial components. It was designed by Logical Product (LP-UUEC002) and has a total length of 0.069 m, including the holders located at the two ends of the sensor. The holders are designed to maintain the acceleration sensor tightly fixed inside the arrow's shaft. Two types of holders with different length, shown in Figure 3.6, were tested. The acceleration sensor is energized by utilizing a fishing tackle's Lithium 3 V battery. To extract the recorded data, the acceleration sensor was designed with a USB port. The total mass of the sensor (including the holders and battery) is 1.37 $\times$ 10^{-3} kg. The measurement frequency is 200 Hz and it can record deceleration up to 16 g (g denotes the gravitational acceleration) and a maximum rotation rate of 2250 deg s^{-1}. The recording procedure begins once the sensor experiences an acceleration of 10 g during the propulsion stage. The sensor registers the deceleration and angular velocity up to 2 s.

Moreover, to locate the sensor well in the front part of the arrow, the insert of the point was cut, as shown in Figure 3.7. The acceleration sensor replaces the mass of the cut section, keeping the total mass of the arrow unchanged. The sensor was inserted from the rear part of the arrow and slid to the front end carefully, as shown in Figure 3.8.

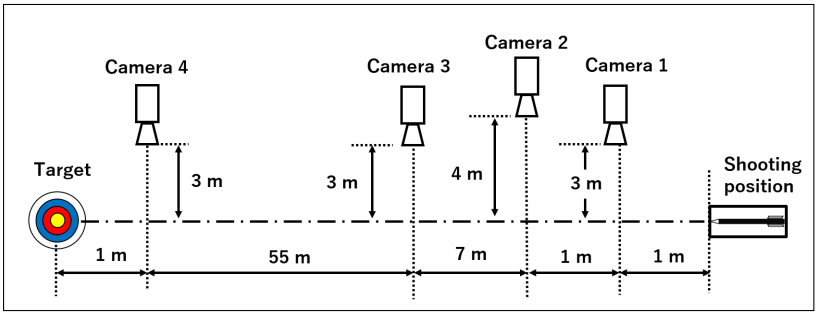

(a)

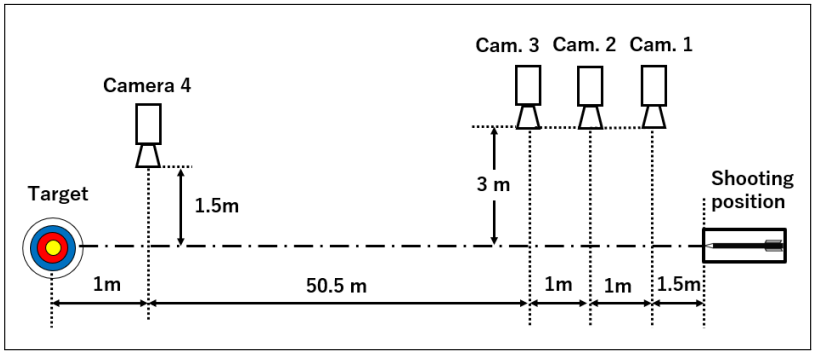

(b)

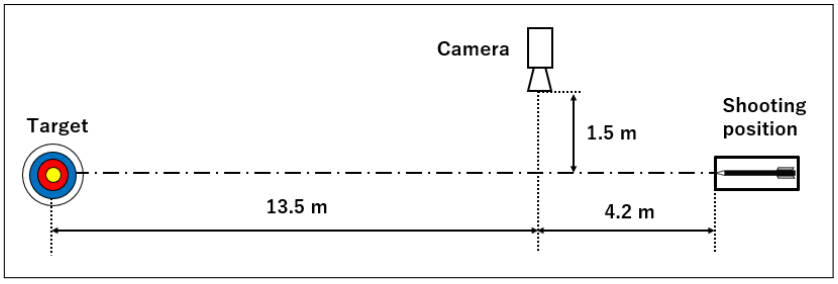

(c)

Figure 3.4: Three different indoors archery ranges in which the free flight test were carried out. a) Long archery range at JISS of 65 m, b) Long archery range in Edogawa of 55 m and c) Short archery range in UEC of 17.7 m.

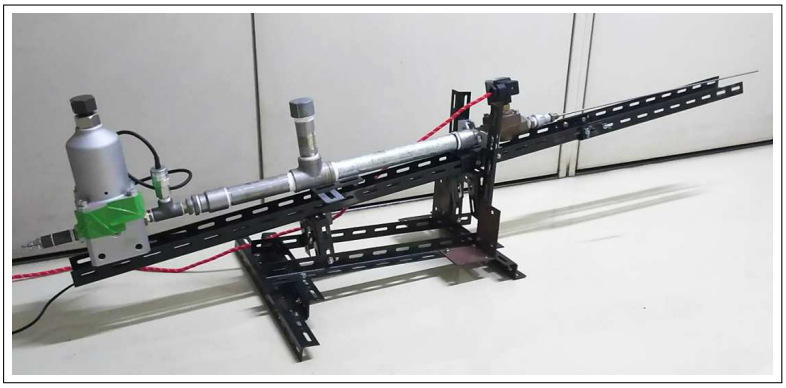

Figure 3.5: Compressed-air launching device.

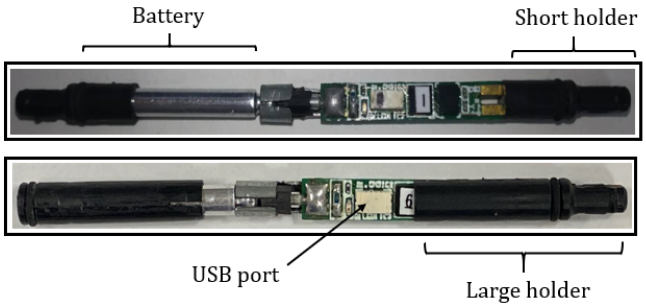

Figure 3.6: Main components of the acceleration sensor.

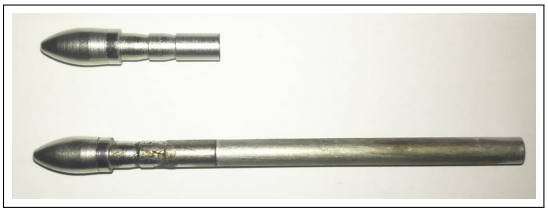

Figure 3.7: The point's insert was cut to allow the location of the acceleration sensor.

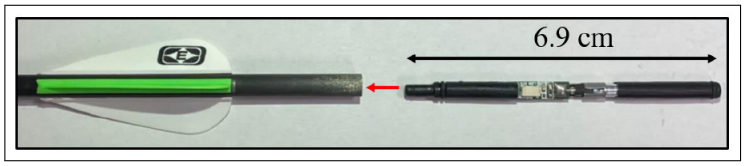

Figure 3.8: Acceleration sensor being introduced from the arrow's rear part.

Chapter 4

Equations of arrow motion

This chapter presents the equations that describe the trajectory and attitude of archery arrows in free flight under still air conditions and considering the background wind effect. The still air conditions refer to the case in which the wind currents are considered to be negligible. The arrows' attitude and trajectory are influenced uniquely by the gravitational acceleration and the aerodynamic load exerted on the arrows. Nevertheless the wind gusts that may occur in outdoor competitions are not taken into account under the still air approach.

The consideration of the background wind is crucial in simulating accurately the outdoor arrow motion. The background wind is considered as one of the most important elements disturbing the shots that are beyond the control of the archers [31, 32]. Since the major archery competitions are performed outdoors, the response of arrows to several background wind conditions has to be analysed in order to determine which arrow configurations would display the best performance in the competitions. In the current work several types of winds, for which the characteristics are different, are analysed in Chapter 6.

As mentioned in Chapter 3, we shot the arrows using a canyon-type blowing off system. Therefore the arrows are tightly fixed into the blowing nozzle before being shot, preventing them to have an oscillatory motion along their shafts that would arise if shot with recurve bows. The latter allow us to model the arrows as rigid bodies. The equations of motion are computed numerically to determine the trajectory and attitude of the arrows during free flight. In the following sections the details of such mathematical model are explained.

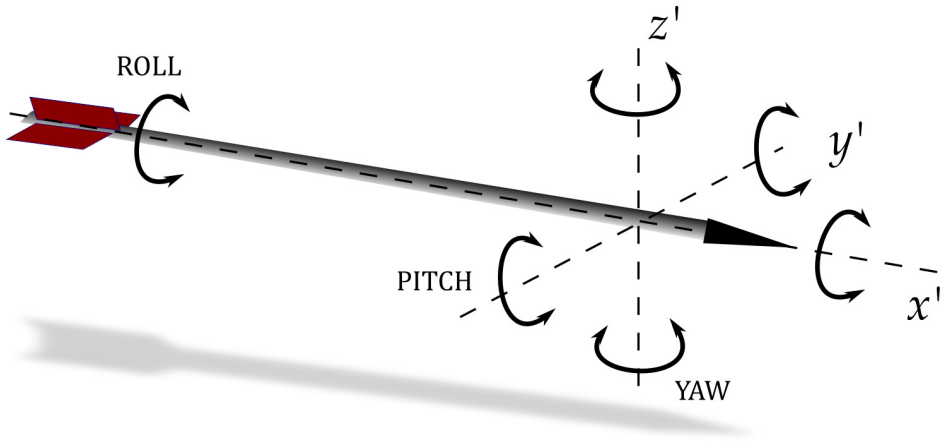

Figure 4.1: Basic movements of an arrow during free flight.

4.1 Equations of arrow motion under still-air conditions

Besides the arrows' translation between the shooting position to the target, the arrows rotate around their longitudinal (x'), horizontal (y') and vertical (z') axes, as shown in Figure 4.1. Such rotation movements can be referred as roll, pitch and yaw, respectively and they are considered in the computation of the equations of arrow motion.

Let us define first two Cartesian right-handed 3D reference frames, of which one will be arbitrarily called the *inertial* frame (xyz) and the other will be referred to as the *arrow's* frame ($x'y'z'$). The inertial frame is an earth-fixed set of axes used as an unmoving frame. Whereas the arrow's frame is fixed to the arrow itself and its orientation changes with time as the arrow moves. Consider the unit vectors $\boldsymbol{i}$,$\boldsymbol{j}$ and $\boldsymbol{k}$ in the direction of x, y and z, respectively, as shown in Figure 4.2. Figure 4.2 shows a flying arrow, in which the horizontal plane parallel to the ground is formed by the x-y axes. Thus, the arrow's velocity vector is defined as $\boldsymbol{V}$=VsinΘ cosΦ $\boldsymbol{i}$+ VsinΘ sinΦ $\boldsymbol{j}$+ VcosΘ $\boldsymbol{k}$, where the angle formed between $\boldsymbol{V}$ and the z axis is Θ (Figure 4.3a). The angle Φ is formed between $[\boldsymbol{V} - (\boldsymbol{V} \cdot \boldsymbol{k})\boldsymbol{k}]$ and the x axis (Figure 4.3b). Thus, the three spatial components of the arrow's velocity are expressed as

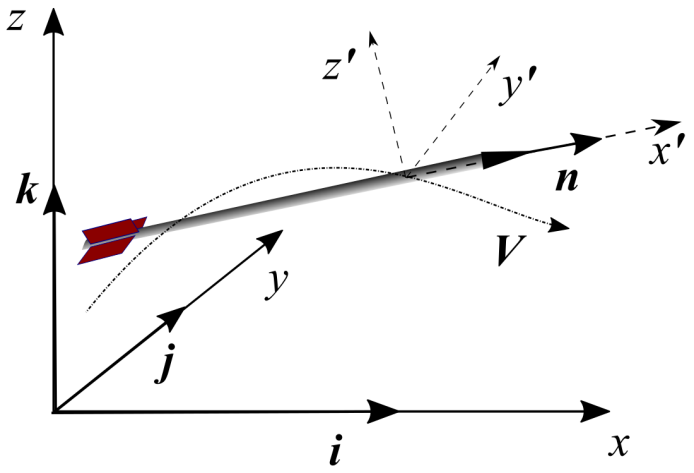

Figure 4.2: a) Representation of an arrow in free flight and the relevant magnitudes described in the mathematical model.

$$\frac{dx}{dt} = V\sin\Theta\cos\Phi, \tag{4.1}$$

$$\frac{dy}{dt} = V\sin\Theta\sin\Phi, \tag{4.2}$$

$$\frac{dz}{dt} = V\cos\Theta. \tag{4.3}$$

Due to the pitch and yaw rotations, the arrow's axis and its velocity vector are misaligned during the free flight. To quantify such misalignment we must introduce the concept of angle of attack, γ. Consider a unit vector $\boldsymbol{n}$ along the arrow's axis which coincides with x', as shown in Figure 4.2. The angle formed between $\boldsymbol{n}$ and the z axis is called the pitch angle θ (Figure 4.3a). Whereas the yaw angle ϕ is formed between $[\boldsymbol{n}\text{-}(\boldsymbol{n}\cdot\boldsymbol{k})\,\boldsymbol{k}]$ and the x axis (Figure 4.3b). Therefore, the unit vector along the arrow's axis is defined as $\boldsymbol{n}$=sinθ cosϕ $\boldsymbol{i}$+ sinθ sinϕ $\boldsymbol{j}$+ cosθ $\boldsymbol{k}$. Thus, the angle of attack can be defined as $\gamma = \cos^{-1}(\boldsymbol{n}\cdot\boldsymbol{V}/|\boldsymbol{V}|)$.

A non-zero angle of attack during the arrow's flight generates a lift force $\boldsymbol{F}_{\mathrm{L}}$ normal to $\boldsymbol{n} = (\boldsymbol{V}/|\boldsymbol{V}|)$. Further, drag force is also experienced by the arrow during free flight and is denoted as $\boldsymbol{F}_{\mathrm{D}}$. The arrows' geometry is determinant to define the drag exerted on them. Both the aerodynamic lift and drag are defined in their vector forms, respectively, as

$$\boldsymbol{F}_{\mathrm{L}} = \frac{1}{2}\alpha\rho\pi r^2[|\boldsymbol{V}|^2\boldsymbol{n} - (\boldsymbol{n}\cdot\boldsymbol{V})\boldsymbol{V}], \tag{4.4}$$

$$\boldsymbol{F}_{\mathrm{D}} = -\frac{1}{2}C_{\mathrm{D}}\rho\pi r^2|\boldsymbol{V}|\boldsymbol{V}, \tag{4.5}$$

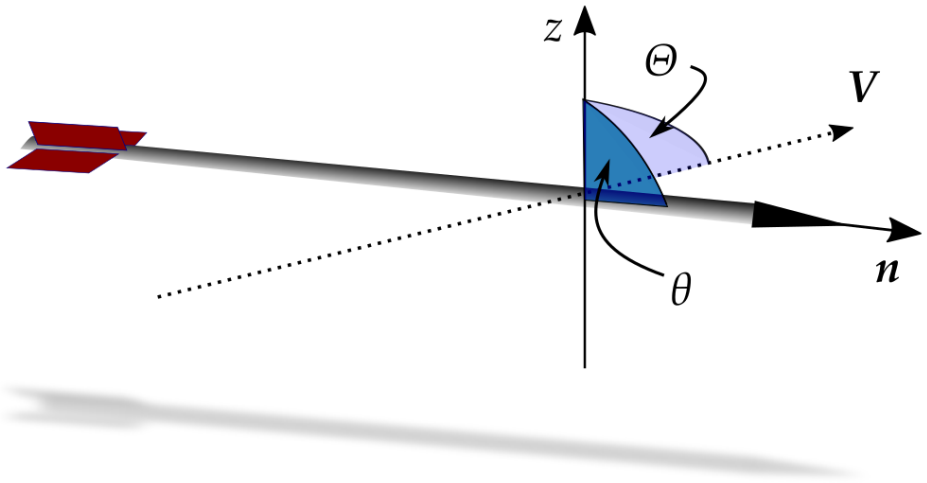

(a)

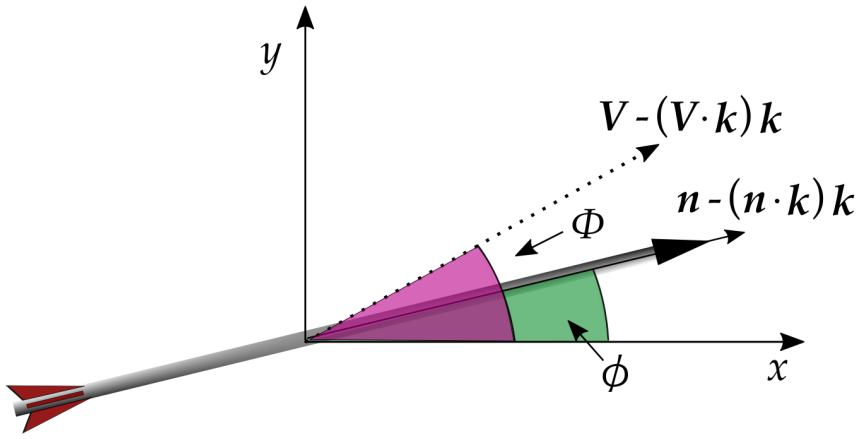

(b)

Figure 4.3: a) Representation of an arrow in free flight and the relevant magnitudes described in the mathematical model.

where α is a parameter related with the lift coefficient by $C_{\mathrm{L}} = \alpha\gamma$, which is valid as long as γ remains small. The values of C_{L} for the different arrow configurations were obtained from the MSBS tests and are given in Chapter 5. Here ρ and r denote the air's density and the arrow's radius, respectively. Here the drag coefficient is C_{D}. The static values of C_{D} were obtained from the MSBS tests for various Reynolds numbers, Re, and for different arrows' configurations. Whereas the instantaneous values of C_{D} were obtained from the acceleration sensor data for each of the shots (Chapter 5) for the A/C/E arrow using straight short and large vanes. Thus, the arrow's governing motion equation can be written as

$$M\frac{\mathrm{d}\boldsymbol{V}}{\mathrm{d}t} = -Mg\boldsymbol{k} + \boldsymbol{F}_{\mathrm{D}} + \boldsymbol{F}_{\mathrm{L}}, \tag{4.6}$$

where M is the arrow's total mass and g is the gravitational acceleration. After considering the Equations 4.4 and 4.5 and carrying out the corresponding algebra, Equation 4.6 becomes

$$\begin{aligned} V \quad & \frac{\mathrm{d}\Phi}{\mathrm{d}t}(-\sin\Theta\sin\Phi\boldsymbol{i} + \sin\Theta\cos\Phi\boldsymbol{j}) + \\ V \quad & \frac{\mathrm{d}\Theta}{\mathrm{d}t}(\cos\Theta\cos\Phi\boldsymbol{i} + \cos\Theta\sin\Phi\boldsymbol{j} - \sin\Theta\boldsymbol{k}) + \\ & \frac{\mathrm{d}V}{\mathrm{d}t}(\sin\Theta\,\cos\Phi\boldsymbol{i} + \sin\Theta\sin\Phi\boldsymbol{j} + \cos\Theta\boldsymbol{k}) = \\ & -g\boldsymbol{k} - \frac{1}{2M}C_D\rho\pi r^2|\boldsymbol{V}|\boldsymbol{V} + \frac{1}{2M}\alpha\rho\pi r^2[|\boldsymbol{V}|^2\boldsymbol{n} - (\boldsymbol{n}\cdot\boldsymbol{V})\boldsymbol{V}]. \end{aligned} \tag{4.7}$$

By multiplying Equation 4.7 by $(-\sin\Theta\sin\Phi\boldsymbol{i} + \sin\Theta\cos\Phi\boldsymbol{j})$, $(\cos\Theta\cos\Phi\boldsymbol{i} + \cos\Theta\sin\Phi\boldsymbol{j} - \sin\Theta\boldsymbol{k})$ and $(\sin\Theta\,\cos\Phi\boldsymbol{i} + \sin\Theta\sin\Phi\boldsymbol{j} + \cos\Theta\boldsymbol{k})$, respectively, is possible to obtain

$$\frac{\mathrm{d}\Phi}{\mathrm{d}t} = \frac{\alpha\rho\pi V r^2}{2M}\frac{[\sin\theta\sin(\phi-\Phi)]}{\sin\Theta}, \tag{4.8}$$

$$\frac{\mathrm{d}\Theta}{\mathrm{d}t} = \frac{g}{V}\sin\Theta + \frac{\alpha\rho\pi V r^2}{2M}[\sin\theta\cos\Theta\cos(\phi-\Phi) - \cos\theta\sin\Theta], \tag{4.9}$$

$$\frac{\mathrm{d}V}{\mathrm{d}t} = -g\cos\Theta - \frac{1}{2}\frac{C_D\rho\pi r^2 V^2}{M}. \tag{4.10}$$

Further, the angular momentum is given by $\boldsymbol{L} = I\boldsymbol{n}\times\mathrm{d}\boldsymbol{n}/\mathrm{d}t + I_3\omega_3\boldsymbol{n}$, where I and I_3 are the moments of inertia around the arrow's center of mass and longitudinal axis, respectively. The rotation rate around the arrow's axis is ω_3. For the case

of still-air conditions, we know the instantaneous value of ω_3 from the free flight tests for each of the shots. The three spatial components of the arrow's rotation were obtained using the acceleration sensor inserted on the arrows at every shot. Therefore, the rate of change of the angular momentum can be computed with

$$\begin{aligned}\frac{\mathrm{d}\boldsymbol{L}}{\mathrm{d}t} &= I\boldsymbol{n}\times\frac{\mathrm{d}^2\boldsymbol{n}}{\mathrm{d}t^2}+I_3\left(\frac{\mathrm{d}\omega_3}{\mathrm{d}t}\boldsymbol{n}+\omega_3\frac{\mathrm{d}\boldsymbol{n}}{\mathrm{d}t}\right)\\ &= \frac{1}{2}\beta\rho\pi r^2 l|\boldsymbol{V}|\boldsymbol{n}\times\boldsymbol{V}+N_3\boldsymbol{n}, \end{aligned} \tag{4.11}$$

where l is the arrow's length and N_3 is the axial component of the torque, $\boldsymbol{N}$, exerted on the arrow during free flight. The right hand side of Equation 4.11 is the pitching moment in its vectorial form. Here β is a numerical parameter related to the pitching moment coefficient by $C_\mathrm{M}=-\beta\gamma$ and valid as long as γ remains small. The magnitudes of C_M for the different arrow configurations were obtained from the MSBS tests and are given in Chapter 5. After solving the corresponding algebra, Equation 4.11 can be written as

$$\begin{aligned}&\Big[-2I\frac{\mathrm{d}\phi}{\mathrm{d}t}\frac{\mathrm{d}\theta}{\mathrm{d}t}\left(\cos^2\theta\cos\phi\boldsymbol{i}+\cos^2\theta\sin\phi\boldsymbol{j}-\sin\theta\cos\theta\boldsymbol{k}\right)+\\ &I\frac{\mathrm{d}^2\phi}{\mathrm{d}t^2}\left(\sin\theta\sin\phi\cos\theta\boldsymbol{i}-\sin\theta\cos\phi\cos\theta\boldsymbol{j}\right)+I\frac{\mathrm{d}^2\theta}{\mathrm{d}t^2}\left(-\sin\phi\boldsymbol{i}+\cos\phi\boldsymbol{j}\right)-\\ &I\frac{\mathrm{d}^2\phi}{\mathrm{d}t^2}\left(\sin\theta\cos\theta\cos\phi\boldsymbol{i}+\sin\theta\sin\phi\cos\theta\boldsymbol{j}-\sin^2\theta\boldsymbol{k}\right)\Big]+\\ &\Big[I_3\frac{\mathrm{d}\omega_3}{\mathrm{d}t}\left(\sin\theta\cos\phi\boldsymbol{i}+\sin\theta\sin\phi\boldsymbol{j}+\cos\theta\boldsymbol{k}\right)+\\ &I_3\omega_3\frac{\mathrm{d}\theta}{\mathrm{d}t}\left(\cos\theta\cos\phi\boldsymbol{i}+\cos\theta\sin\phi\boldsymbol{j}-\sin\theta\boldsymbol{k}\right)-\\ &I_3\omega_3\frac{\mathrm{d}\phi}{\mathrm{d}t}\left(\sin\theta\sin\phi\boldsymbol{i}-\sin\theta\cos\phi\boldsymbol{j}\right)\Big]=\\ &\frac{1}{2}\beta\rho\pi l r^2V^2\Big[(\sin\theta\sin\phi\cos\Theta-\sin\Theta\sin\Phi\cos\theta)\boldsymbol{i}-\\ &(\sin\theta\cos\phi\cos\Theta-\sin\Theta\cos\Phi\cos\theta)\boldsymbol{j}+\\ &(\sin\theta\cos\phi\sin\Theta\sin\Phi-\sin\Theta\cos\Phi\sin\theta\sin\phi)\boldsymbol{k}\Big]+\\ &N_3[\sin\theta\cos\phi\boldsymbol{i}+\sin\theta\sin\phi\boldsymbol{j}+\cos\theta\boldsymbol{k}]. \end{aligned} \tag{4.12}$$

Further, by multiplying Equation 4.12 by ($\cos\theta\cos\phi\boldsymbol{i}$+$\cos\theta\sin\phi\boldsymbol{j}$-$\sin\theta\boldsymbol{k}$) and (-$\sin\theta\sin\phi\boldsymbol{i}$+$\sin\theta\cos\phi\boldsymbol{j}$), respectively, is possible to obtain

$$\frac{d^2\phi}{dt^2} = \omega_3 \frac{I_3}{I\sin\theta}\frac{d\theta}{dt} - 2\frac{\cos\theta}{\sin\theta}\frac{d\phi}{dt}\frac{d\theta}{dt} - \frac{1}{2}\frac{\beta\rho\pi l r^2 V^2}{I\sin\theta}[\sin\Theta\sin(\phi-\Phi)] \tag{4.13}$$

$$\frac{d^2\theta}{dt^2} = \frac{1}{2I}\beta\rho\pi l r^2 V^2[\sin\Theta\cos\theta\cos(\phi-\Phi) - \sin\theta\cos\Theta] + \sin\theta\cos\theta\frac{d^2\phi}{dt^2} - \omega_3\sin\theta\frac{I_3}{I}\frac{d\phi}{dt}. \tag{4.14}$$

Each of the second order differential Equations 4.13 and 4.14 can be expressed as a system of two first order differential equations by introducing the two new dependent variables ω_ϕ and ω_θ; such that $\omega_\phi = d\phi/dt$, $d\omega_\phi/dt = d^2\phi/dt^2$, $\omega_\theta = d\theta/dt$ and $d\omega_\theta/dt = d^2\theta/dt^2$. When the system of differential equations formed by 4.1, 4.2, 4.3, 4.8, 4.9, 4.10, 4.13 and 4.14 is solved, it is possible to know the position and attitude of the arrow at any given instant during its flight. The system of differential equations was computed numerically by using a standard 4th order Runge-Kutta method with a time step $\Delta t = 5 \times 10^{-4}$ s.

A suitable time step was obtained through the corresponding step size analysis [22]. The time step was verified to be adequately small to keep the accuracy up to three significant digits in the mantissa. The values of Δt for the 4th order Runge-Kutta method can be determined with

$$\Delta t = \left(\frac{\xi}{A}\right)^{1/5}, \tag{4.15}$$

where ξ is the desired error and A is a problem dependent constant obtained trough a series of tests using the written computational code. For an error $\xi < 10^{-3}$ the time step must be $\Delta t < 7.5 \times 10^{-4}$. Therefore, it was used an adequately small time step $\Delta t = 5 \times 10^{-4}$ in the computations. Appendix A offers more information related to the Runge-Kutta algorithm.

The value of γ is also important for the transition of the boundary layer from laminar to turbulent state. Miyazaki et al. [22] reported that if the arrow is launched with certain ideal initial conditions, the maximum angle of attack along all the flight of the arrow would be small enough to keep a laminar boundary layer. A transition zone was identified to occur when the maximum angle of attack (γ_{max}) was approximately $0.40^\circ < \gamma_{max} < 0.60^\circ$ with A/C/E for Reynolds number Re= 1.75×10^4. These results were obtained through free flight experiments under no wind conditions and showed a dependence between the boundary layer state and the attitude of the arrow, specifically the relation C_D-γ_{max}.

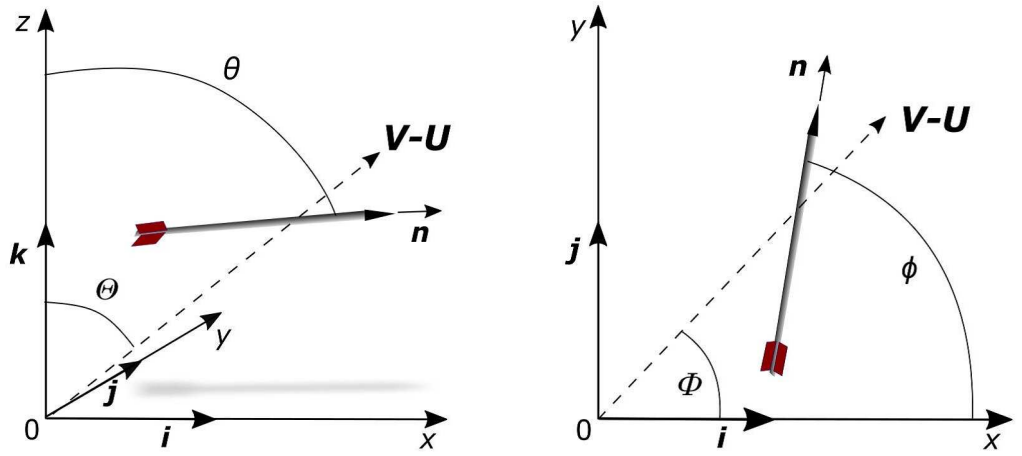

Figure 4.4: Representation of an arrow in free flight and the vectorial magnitudes described in the mathematical model.

Finally, the instantaneous computation of the angle of attack is given by

$$\gamma = \cos^{-1}\left(\sin\Theta\cos\Phi\sin\theta\cos\phi + \sin\Theta\sin\Phi\sin\theta\sin\phi + \cos\Theta\cos\theta\right). \tag{4.16}$$

4.2 Equations of arrow motion considering the background wind

In this section are given the equations of motion for an archery arrow considering the influence of the background wind. In the mathematical model, $\boldsymbol{U}$ represents the background wind and in order to simulate the conditions under which the archery competitions take place, its velocity is considered to show three different types of behaviour, i.e. uniform, non-uniform and the actual behaviour in the area where the archery competition is going to be held in the Summer Olympic games in Tokyo.

Here the relative velocity of the arrow is defined as the vectorial difference of its center of mass' velocity, $\boldsymbol{V}$=$V\sin\Theta\cos\Phi$+ $V\sin\Theta\sin\Phi$+ $V\cos\Theta$ and the background wind component, $\boldsymbol{U}$=u_x+ u_y+ u_z, or $\boldsymbol{V}$-$\boldsymbol{U}$. The angle formed between $\boldsymbol{V}$-$\boldsymbol{U}$ and z is Θ as shown in Figure 4.4. Whereas the angle formed between the projection of $\boldsymbol{V}$-$\boldsymbol{U}$ in the xy plane and x is Φ. The unit vector tangential to the trajectory of the center of mass and parallel to $\boldsymbol{V}$-$\boldsymbol{U}$ is introduced as $\boldsymbol{t}$=$\boldsymbol{V}$-$\boldsymbol{U}$/$|\boldsymbol{V}$-$\boldsymbol{U}|$.

As in the still-air approach, the unit vector along the arrow's axis is $\boldsymbol{n}$=sinθ cosϕ+ sinθsinϕ+ cosθ. The angle θ is formed between $\boldsymbol{n}$ and z, whereas ϕ is the angle formed between the projection of $\boldsymbol{n}$ in the xy plane with x, as shown in Figure 4.4. When considering the background wind influence, the angle of attack is defined as γ=cos$^{-1}(\boldsymbol{n}\cdot\boldsymbol{t})$. The flying arrows that are not pointing along its direction of motion will present an asymmetric profile to the wind, resulting in sidewards motion in the same direction as the rotation. Such behaviour will occur even at still-air conditions. Lateral displacement due to the Magnus effect or gyroscopic precession results are much smaller than the drift provoked by the background wind currents.

When the background wind influence is considered, the aerodynamic forces drag ($\boldsymbol{F}_{\mathrm{D}}$) and lift ($\boldsymbol{F}_{\mathrm{L}}$) in their standard vector forms are expressed as

$$\boldsymbol{F}_{\mathrm{L}} = \frac{1}{2}\alpha\rho\pi r^2[|\boldsymbol{V}-\boldsymbol{U}|^2\boldsymbol{n}-\boldsymbol{n}\cdot(\boldsymbol{V}-\boldsymbol{U})(\boldsymbol{V}-\boldsymbol{U})], \tag{4.17}$$

$$\boldsymbol{F}_{\mathrm{D}} = -\frac{1}{2}C_D\rho\pi r^2|\boldsymbol{V}-\boldsymbol{U}|(\boldsymbol{V}-\boldsymbol{U}). \tag{4.18}$$

The former is exerted in the direction of the relative motion between the arrow and the air flow. Whereas the latter is perpendicular to such relative motion. Here C_{D} represents the drag coefficient, the air's density is denoted by ρ and r is the radius of the arrow. The parameter α is related to C_{L} and obtained using Equation 5.1.

By considering Equations 4.17 and 4.18, after some algebra Equation 4.6 becomes

$$\begin{aligned} V\ & \frac{\mathrm{d}\Phi}{\mathrm{d}t}(-\sin\Theta\sin\Phi\boldsymbol{i}+\sin\Theta\cos\Phi\boldsymbol{j})+ \\ V\ & \frac{\mathrm{d}\Theta}{\mathrm{d}t}(\cos\Theta\cos\Phi\boldsymbol{i}+\cos\Theta\sin\Phi\boldsymbol{j}-\sin\Theta\boldsymbol{k})+ \\ & \frac{\mathrm{d}V}{\mathrm{d}t}(\sin\Theta\,\cos\Phi\boldsymbol{i}+\sin\Theta\sin\Phi\boldsymbol{j}+\cos\Theta\boldsymbol{k})= \\ & -g\boldsymbol{k}-\frac{1}{2M}C_D\rho\pi r^2|\boldsymbol{V}-\boldsymbol{U}|(\boldsymbol{V}-\boldsymbol{U}) \\ & +\frac{1}{2M}\alpha\rho\pi r^2[|\boldsymbol{V}-\boldsymbol{U}|^2\boldsymbol{n}-\boldsymbol{n}\cdot(\boldsymbol{V}-\boldsymbol{U})(\boldsymbol{V}-\boldsymbol{U})]. \end{aligned} \tag{4.19}$$

By multiplying Equation 4.19 by $(-\sin\Theta\sin\Phi\boldsymbol{i}+\sin\Theta\cos\Phi\boldsymbol{j})$, $(\cos\Theta\cos\Phi\boldsymbol{i}+\cos\Theta\sin\Phi\boldsymbol{j}-\sin\Theta\boldsymbol{k})$ and $(\sin\Theta\,\cos\Phi\boldsymbol{i}+\sin\Theta\sin\Phi\boldsymbol{j}+\cos\Theta\boldsymbol{k})$, is possible to obtain

$$\begin{aligned}\frac{\mathrm{d}V}{\mathrm{d}t} &= -g\cos - \frac{1}{2}\frac{C_D\rho\pi r^2}{M}|\boldsymbol{V}-\boldsymbol{U}|(V - u_x\sin\Theta\cos\Phi - u_y\sin\Theta\sin\Phi - u_z\cos\Theta) \\ &+ \frac{1}{2}\frac{\alpha\rho\pi r^2}{M}\{|\boldsymbol{V}-\boldsymbol{U}|^2[\sin\theta\sin\Theta\cos(\Phi-\phi)+\cos\theta\cos\Theta] \\ &- [\boldsymbol{n}\cdot(\boldsymbol{V}-\boldsymbol{U})][V - u_x\sin\Theta\cos\Phi - u_y\sin\Theta\sin\Phi - u_z\cos\Theta]\}, \qquad (4.20)\end{aligned}$$

$$\begin{aligned}\frac{\mathrm{d}\Theta}{\mathrm{d}t} &= \frac{g}{V}\sin\Theta - \frac{1}{2}\frac{C_D\rho\pi r^2}{MV}|\boldsymbol{V}-\boldsymbol{U}|(-u_x\cos\Theta\cos\Phi - u_y\cos\Theta\sin\Phi + u_z\sin\Theta) \\ &+ \frac{1}{2}\frac{\alpha\rho\pi r^2}{MV}\{|\boldsymbol{V}-\boldsymbol{U}|^2[\sin\theta\cos\Theta\cos(\Phi-\phi) - \cos\theta\sin\Theta] \\ &+ [\boldsymbol{n}\cdot(\boldsymbol{V}-\boldsymbol{U})][u_x\cos\Theta\cos\Phi + u_y\cos\Theta\sin\Phi - u_z\sin\Theta]\}, \qquad (4.21) \\ \frac{\mathrm{d}\Phi}{\mathrm{d}t} &= -\frac{1}{2}\frac{C_D\rho\pi r^2}{MV\sin\Theta}|\boldsymbol{V}-\boldsymbol{U}|(u_x\sin\Phi - u_y\cos\Phi) \\ &+ \frac{1}{2}\frac{\alpha\rho\pi r^2}{MV}\{|\boldsymbol{V}-\boldsymbol{U}|^2[\sin\theta\sin(\phi-\Phi)] \\ &- [\boldsymbol{n}\cdot(\boldsymbol{V}-\boldsymbol{U})][u_x\sin\Phi - u_y\cos\Phi]\}. \qquad (4.22)\end{aligned}$$

The rate of change of the angular momentum considering the background wind is therefore given by

$$\begin{aligned}\frac{\mathrm{d}\boldsymbol{L}}{\mathrm{d}t} &= I\boldsymbol{n}\times\frac{\mathrm{d}^2\boldsymbol{n}}{\mathrm{d}t^2} + I_3\left(\frac{\mathrm{d}\omega_3}{\mathrm{d}t}\boldsymbol{n} + \omega_3\frac{\mathrm{d}\boldsymbol{n}}{\mathrm{d}t}\right) \\ &= \frac{1}{2}\beta\rho\pi r^2 l|\boldsymbol{V}-\boldsymbol{U}|\boldsymbol{n}\times(\boldsymbol{V}-\boldsymbol{U}) + N_3\boldsymbol{n}. \qquad (4.23)\end{aligned}$$

Here, M is the mass of the arrow, g is the gravitational acceleration and l is the length of the arrow. β is related to C_M through Equation 5.2. The axial component of the torque is N_3, for which it was not possible to obtain any data from the MSBS nor from the free flight tests. During the still-air conditions we were able to obtain the arrow's rotation rate, ω_3, from the acceleration sensor measurements. Nevertheless, we do not posses experimental data about ω_3 due to the difficulty to design and perform outdoor free flight tests under controlled conditions. The latter means that it was not possible to compute the axial component of the torque. Therefore, it was necessary to introduce the empirical assumption that the arrow's rotation rate is independent of the angle of attack and proportional to $|\boldsymbol{V}-\boldsymbol{U}|$. The spin parameter $S_P = \omega_3 r/|\boldsymbol{V}-\boldsymbol{U}|$ was assumed to remain constant regardless of γ,

as long as it is small, which was verified by the MSBS experiments for $|\gamma| < 3.0°$. The values of S_P for A/C/E and X10 arrows are given in Chapter .

After carrying out the algebra, Equation 4.23 becomes

$$\begin{aligned}
&\Big[-2I\frac{d\phi}{dt}\frac{d\theta}{dt}\left(\cos^2\theta\cos\phi\boldsymbol{i}+\cos^2\theta\sin\phi\boldsymbol{j}-\sin\theta\cos\theta\boldsymbol{k}\right)+\\
&I\frac{d^2\phi}{dt^2}\left(\sin\theta\sin\phi\cos\theta\boldsymbol{i}-\sin\theta\cos\phi\cos\theta\boldsymbol{j}\right)+I\frac{d^2\theta}{dt^2}\left(-\sin\phi\boldsymbol{i}+\cos\phi\boldsymbol{j}\right)-\\
&I\frac{d^2\phi}{dt^2}\left(\sin\theta\cos\theta\cos\phi\boldsymbol{i}+\sin\theta\sin\phi\cos\theta\boldsymbol{j}-\sin^2\theta\boldsymbol{k}\right)\Big]+\\
&\Big[I_3\frac{d\omega_3}{dt}\left(\sin\theta\cos\phi\boldsymbol{i}+\sin\theta\sin\phi\boldsymbol{j}+\cos\theta\boldsymbol{k}\right)+\\
&I_3\omega_3\frac{d\theta}{dt}\left(\cos\theta\cos\phi\boldsymbol{i}+\cos\theta\sin\phi\boldsymbol{j}-\sin\theta\boldsymbol{k}\right)-\\
&I_3\omega_3\frac{d\phi}{dt}\left(\sin\theta\sin\phi\boldsymbol{i}-\sin\theta\cos\phi\boldsymbol{j}\right)\Big]=\\
&\frac{1}{2}\beta\rho\pi r^2 l|\boldsymbol{V}-\boldsymbol{U}|\\
&\Big[(V\sin\theta\sin\phi\cos\Theta-\mathrm{u}_z\sin\theta\sin\phi-V\sin\Theta\sin\Phi\cos\theta+u_y\cos\theta)\boldsymbol{i}-\\
&(V\sin\theta\cos\phi\cos\Theta-u_z\sin\theta\cos\phi-V\sin\Theta\cos\Phi\cos\theta+u_x\cos\theta)\boldsymbol{j}+\\
&(V\sin\theta\cos\phi\sin\Theta\sin\Phi-u_y\sin\theta\cos\phi-V\sin\Theta\cos\Phi\sin\theta\sin\phi+u_x\sin\theta\sin\phi)\boldsymbol{k}\Big]+\\
&N_3[\sin\theta\cos\phi i+\sin\theta\sin\phi\boldsymbol{j}+\cos\theta\boldsymbol{k}].
\end{aligned} \tag{4.24}$$

By multiplying Equation 4.24 by ($\cos\theta\cos\phi\boldsymbol{i}$+$\cos\theta\sin\phi\boldsymbol{j}$-$\sin\theta\boldsymbol{k}$) and considering $I_w = I_3SpV/r$, is possible to obtain

$$\begin{aligned}
\frac{d^2\phi}{dt^2} &= -2\frac{\cos\theta}{\sin\theta}\frac{d\phi}{dt}\frac{d\theta}{dt}+\frac{I_w}{I\sin\theta}\frac{d\theta}{dt}-\\
&\frac{1}{2}\frac{\beta\rho\pi r^2 l}{I\sin\theta}|\boldsymbol{V}-\boldsymbol{U}|[V\sin\Theta\sin(\phi-\Phi)-u_x\sin\phi+u_y\cos\phi].
\end{aligned} \tag{4.25}$$

Further, by multiplying Equation 4.24 by (-$\sin\theta\sin\phi\boldsymbol{i}$+$\sin\theta\cos\phi\boldsymbol{j}$) and considering $I_w = I_3SpV/r$ is possible to obtain

$$\begin{aligned}
\frac{d^2\theta}{dt^2} &= \sin\theta\cos\theta\frac{d^2\phi}{dt^2}-\frac{I_w}{I}\frac{d\phi}{dt}\sin\theta+\frac{1}{2}\beta\rho\pi r^2 l|\boldsymbol{V}-\boldsymbol{U}|\\
&\{V[-\sin\theta\cos\Theta+\sin\Theta\cos\theta\cos(\phi-\Phi)]-\\
&u_x\cos\theta\cos\phi-u_y\sin\phi\cos\theta+u_z\sin\theta\}.
\end{aligned} \tag{4.26}$$

As in the still-air conditions approach, each of the second order differential Equations 4.25 and 4.26 can be expressed as a system of two first order differential equations by recalling that ω_ϕ=dϕ/dt, dω_ϕ/dt=d$^2\phi$/dt^2, ω_θ=dθ/dt and dω_θ/dt=d$^2\theta$/dt^2. When the system of differential equations conformed by 4.1, 4.2, 4.3, 4.20, 4.21, 4.22, 4.25 and 4.26 is numerically computed, it is the possible to know the attitude and position of the arrow at any time. Finally, the instantaneous computation of the angle of attack is given by

$$\begin{aligned}\gamma &= \cos^{-1}\left(\boldsymbol{n}\cdot\frac{\boldsymbol{V}-\boldsymbol{U}}{|\boldsymbol{V}-\boldsymbol{U}|}\right)\\ &= \cos^{-1}(V[\sin\Theta\sin\theta\cos(\Phi-\phi)+\cos\Theta\cos\theta]-u_x\sin\theta\cos\phi\\ &\quad -u_y\sin\theta\sin\phi-u_z\cos\theta/|\boldsymbol{V}-\boldsymbol{U}|).\end{aligned} \tag{4.27}$$

The results for the computations under still-air conditions and taking into account the background wind are given in Chapter 6.

Chapter 5

Results from the experimental tests

In the current chapter, the results obtained from the two experimental procedures are given. The values of the pitching moment, lift and drag coefficients are obtained from the MSBS tests for various angles of attack and Reynolds numbers, Re. In addition, the instant deceleration, velocity, rotation rate and drag coefficient were obtained from the free flight tests using the acceleration sensor and the high-speed video cameras. The current chapter is divided into sections that include the results obtained from the MSBS tests and the free flight tests.

5.1 Lift and pitching moment dependence of the angle of attack

It is recognized that the value of the angle of attack, γ, is crucial in the dynamics of projectiles [27, 28, 37]. The existence of a non-zero value of angle of attack during the arrow's flight induces drag and lift forces on it. The lift is exerted in the direction of the relative motion between the arrow and the air flow, whereas the drag is perpendicular to such relative motion.

The lift force is proportional to the angle of attack and almost independent of the rotation rate of the arrow, as long as γ is small [33, 30]. Both lift and drag forces lead to wind drift, i.e. the lateral displacement of the arrow due to the presence of wind gusts [30].

The results of the MSBS experiments in Figures 5.1, 5.2 and 5.3 show the dependence of the lift (C_{L}) and pitching moment (C_{M}) coefficients on γ. Figure 5.1 illustrates the results for arrows using the A/C/E and X10 shafts, both fletched with SWV for Re=7.7×10^3 and Re=1.0×10^4. Figure 5.2 compares the values of C_{L} and C_{D} for arrows using A/C/E shafts fletched with the two types of curved vanes, SWV and GPV at Re=7.7×10^3, whereas Figure 5.3 shows the results corresponding to short (Figure 5.3a) and large (Figure 5.3b) straight vanes at

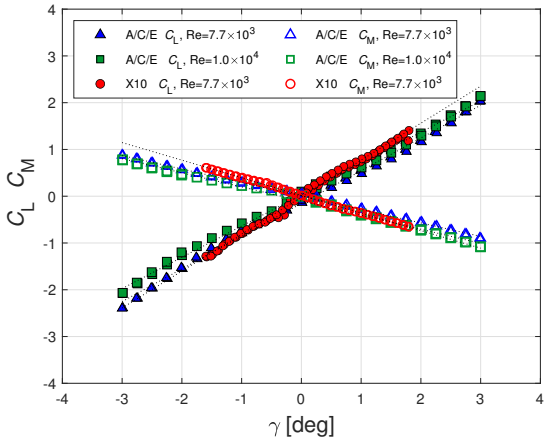

Figure 5.1: Lift (C_L) and pitching moment (C_M) coefficients as function of γ for arrows using A/C/E and X10 shafts at a Reynolds number Re=7.7×10^3 and Re=1.0×10^4.

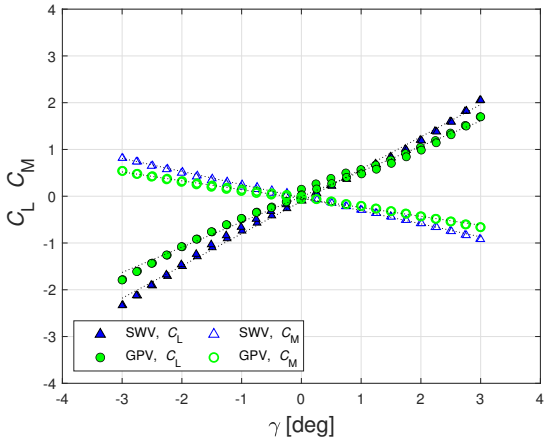

Figure 5.2: Lift (C_L) and pitching moment (C_M) coefficients as function of the angle of attack (γ) for arrows using curved vanes type SWV and GPV at a Reynolds number Re=7.7×10^3.

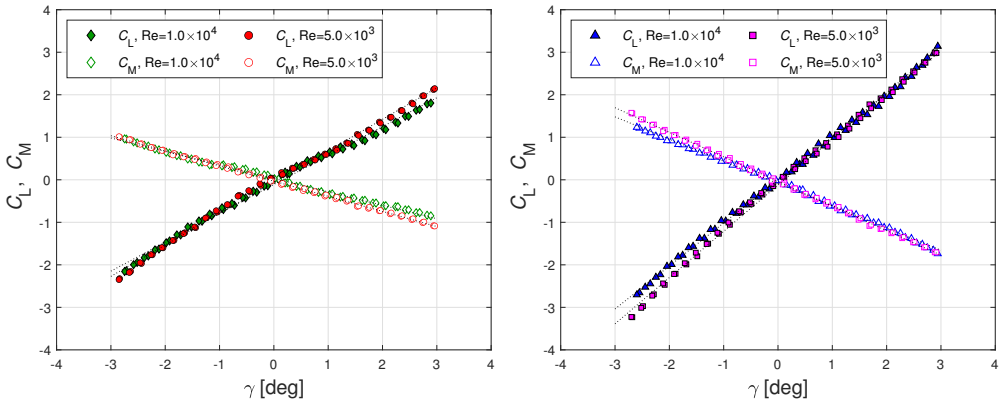

Figure 5.3: Lift (C_L) and pitching moment (C_M) coefficients as function of the angle of attack (γ) for the a) short and b) large straight vanes with a Reynolds number Re=5.0×10^3 and Re=1.0×10^4.

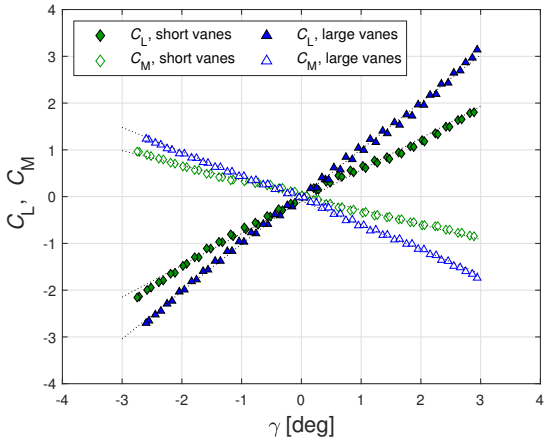

Figure 5.4: Lift (C_L) and pitching moment (C_M) coefficients as function of the angle of attack (γ) for arrows using A/C/E shafts with short and large straight vanes at a Reynolds number Re=1.0×10^4.

Re=5.0×10^3 and Re=1.0×10^4. In Figure 5.4 the results for the short and large vanes at Re=1.0×10^4 are plotted together.

Note that for all the cases a positive lift yields a negative pitching moment. The latter induces an oscillatory behaviour of the arrow in its way to the target. Such characteristic generates a stable arrow's flight. Note that C_L and C_M are proportional to γ. Tables 5.1 and 5.2 show the coefficients of linearity of C_L and C_M at various Reynolds numbers.

In Figure 5.1, larger values of the pitching moment are generated for the case of the arrows using the X10 shaft compared to those using A/C/E. The pitching moment is an important factor to consider in the dynamics of the archery arrows since it stabilizes their flights.

In Figure 5.2, the effect of the two types of curved vanes is compared. The considered vanes are the Spin-Wing Vanes (SWV) and the Gas Pro Vanes (GPV). For both cases the arrows were equipped with A/C/E shafts. Here the difference in C_M and C_L arises from the fact that the SWV have larger area compared to GPV. Vanes with larger area generate larger lift and larger pitching moment. Chapter 6 explains quantitatively the influence of the magnitude of C_M and C_L in the dynamics of flying arrows.

In Figure 5.3 the results corresponding to arrows using short straight vanes and large straight vanes are plotted separately. The values of C_M and C_L for arrows using SWV and straight short vanes were found to show a similar behaviour. The area ratio between the the curved SWV and straight short vanes was around 1.4. Even though the area of vanes is an important factor in the dynamics of arrows, the types of shaft, and therefore the mass, and the moment of inertial appear to be also of importance.

In Figure 5.4 the results corresponding to the short and large straight vanes were plotted together. Larger lift and pitching moments are generated by the arrows using larger straight vanes. The total area ratio of the large to the short straight vanes is around 2.1. It can be expected that arrows with larger vanes show more stable flights than those fletched with shorter ones. The vanes' area is an important factor to be considered by the archers. Assuming the linearity of C_L and C_M with γ,

$$\boldsymbol{C}_L = \alpha\gamma, \tag{5.1}$$

$$\boldsymbol{C}_M = -\beta\gamma, \tag{5.2}$$

it is possible to determine the parameters α and β, which are used in the numerical simulation. They are almost independent of Re, as in Sawada et al.[33]. Therefore, it is reasonable to assume that α and β would not show any significant change in the Re of interest (Re$< 2.01 \times 10^3$). Equations 5.1 and 5.2 are valid as long as γ

Table 5.1: Linear approximation of the lift coefficient C_L for different types of arrows' configurations for $|\gamma| < 3.0°$.

Shaft / point / vanes	Reynolds number (Re)	C_L Linear approximation
X10/ bulge / SWV	7.7×10^3	$0.79\gamma - 0.01$
A/C/E / bulge / SWV	7.7×10^3	$0.70\gamma - 0.15$
A/C/E / bulge / SWV	1.0×10^4	$0.67\gamma + 0.03$
A/C/E / bulge / GPV	7.7×10^3	$0.54\gamma - 0.01$
A/C/E / bulge / short straight	5.0×10^3	$0.68\gamma - 0.11$
A/C/E / bulge / short straight	1.0×10^4	$0.74\gamma - 0.06$
A/C/E / bulge / large straight	5.0×10^3	$1.01\gamma - 0.003$
A/C/E / bulge / large straight	1.0×10^4	$1.09\gamma - 0.13$

Table 5.2: Linear approximation of the pitching moment coefficient C_M for different types of arrows' configurations for $|\gamma| < 3.0°$.

Shaft / point / vanes	Reynolds number (Re)	C_M Linear approximation
X10 / bulge / SWV	7.7×10^3	$-0.38\gamma + 0.02$
A/C/E / bulge / SWV	7.7×10^3	$-0.29\gamma + 0.01$
A/C/E / bulge / SWV	1.0×10^4	$-0.30\gamma - 0.10$
A/C/E / bulge / GPV	7.7×10^3	$-0.19\gamma - 0.05$
A/C/E / bulge / short straight	5.0×10^3	$-0.32\gamma + 0.03$
A/C/E / bulge / short straight	1.0×10^4	$-0.36\gamma - 0.03$
A/C/E / bulge / large straight	5.0×10^3	$-0.52\gamma - 0.09$
A/C/E / bulge / large straight	1.0×10^4	$-0.58\gamma - 0.04$

remains small. In Tables 5.3 and 5.4 the different values of α and β used in the numerical computations are listed.

5.2 Drag coefficient as a function of the angle of attack

The drag exerted on an arrow strongly depends on its attitude or orientation with the fluid flow, as shown in Figures 5.5, 5.6 and 5.7, Here the value of the drag coefficient, C_D, increases with the angle of attack, $|\gamma|$. Figure 5.5 compares the results for arrows using A/C/E and X10 shafts, both with SWV. Besides the type of shaft, two different Reynolds numbers were considered in the experiments. When the arrow was aligned with the wind flow ($\gamma = 0$), there were obtained relatively

Table 5.3: Aerodynamic characteristics of the arrows at Re$= 7.7 \times 10^3$ for arrows using A/C/E and X10 shafts and curved SWV.

Shaft	Vanes	α [1/rad]	β [1/rad]	S_P
A/C/E	SWV	40.2	16.2	0.029
X10	SWV	45.1	21.2	0.034

Table 5.4: Aerodynamic characteristics of the arrows at Re$= 1.0 \times 10^4$ for arrows using A/C/E shaft with short and large straight vanes.

Shaft	Vanes	α [1/rad]	β [1/rad]
A/C/E	Straight small	40.2	16.7
A/C/E	Straight large	55.3	29.1

low values of C_D, which correspond to a laminar boundary layer behaviour. As long as the boundary layer flow remains laminar, C_D changes slightly with Re.

Note that even for small changes in the angle of attack ($\gamma \leq 3.0°$), an abrupt increase in the value of C_D takes place. It is possible to attribute such behaviour to a transition from laminar to turbulent boundary layer flow. However, due to limitations of the experimental apparatus used in the present work, the detailed place along the arrow of the flow transition remains unknown. The latter contrasts with the UV dye/PIV tests carried out by Park et al.[29], where it was identified that the transition to turbulent boundary layer was located at $\sim 2\%$ of the total length of an arrow at Re$\sim 2.74 \times 10^4$ and $\gamma = 0$. The UV dye/PIV tests appear to give more detailed information regarding to the laminar-turbulent transition in the boundary layer.

Figure 5.6 compares the value of C_D as function of γ for A/C/E arrows using the two different types of curved vanes at Re=7.7×10^3. As in the previous case, there exists a laminar-turbulent boundary layer transition when $\gamma \neq 0$. Note that when using the A/C/E shaft, a similar C_D evolution was found, regardless of the types of fletched vanes. This indicates that the vanes are located well inside the turbulent flow region and therefore no important distinction between arrows using curved SWV and GPV is observed.

Figure 5.7a shows the dependence of C_D on γ for a bare A/C/E shaft without vanes at Re=5.0×10^3 and Re=1.0×10^4. It is possible to observe the influence of Re on C_D. Figures 5.7b and 5.7c correspond to the results for A/C/E arrows using short and large straight vanes, respectively, at Re=5.0×10^3 and 1.0×10^4. At Re=1.0×10^4 and with $\gamma = 0$, the values of the drag coefficient were $C_D = 1.5$ and $C_D = 2$ for the arrows using short and large vanes, respectively. In such a case, the

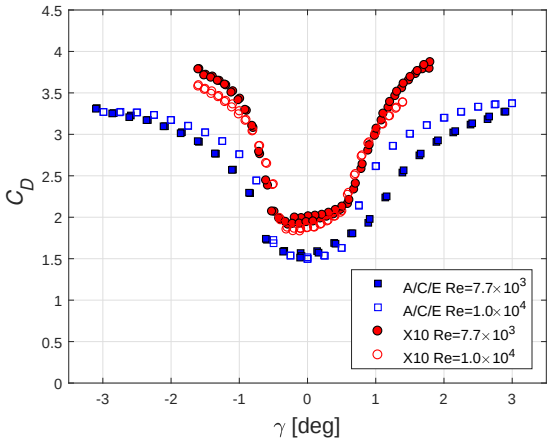

Figure 5.5: Drag coefficient (C_D) as a function of the angle of attack (γ) at Re=7.7×10^3 and 1.0×10^4 for arrows using A/C/E and X10 shafts.

difference in C_D arises from the fact that the total area of the large vanes exceed in around 2.1 times the total area of the short vanes. Previously it was discussed the importance of the stabilizing effect that the vanes generate during the free flight of the arrows. Nevertheless, the vanes are also an important source of drag, as appreciated in Figures 5.7b and 5.7c.

Figure 5.7d illustrates the C_D values of a bare shaft and of arrows with short and large vanes at Re=1.0×10^4. It is possible to observe the delicate relation between the arrow's attitude and the state of an arrow's boundary layer flow. Theoretical studies must be carried out to understand the transition phenomena.

5.3 Drag coefficient as a function of the Reynolds number

The current section gives the relation between the Reynolds number and the value of the drag coefficient, C_D, for arrows using the A/C/E and X10 shafts (Figure 5.8) with SWV. Arrows using A/C/E shafts with two types of straight vanes (Figure 5.9) are also analysed.

Figure 5.8 shows the dependence of C_D on Re obtained from the MSBS experiments and the free flight tests. The MSBS data for an A/C/E shaft (Figure 5.8a) with no vanes (○) showed good agreement with the theoretical solution for the axisymmetric laminar boundary layer on a circular cylinder [16, 34], which is indicated by the solid line (-). The slight difference between the theoretical result and the actual A/C/E shaft without vanes is due to the pressure drag.

For the A/C/E arrow (Figure 5.8a) with (■) and without (○) vanes, it is possible

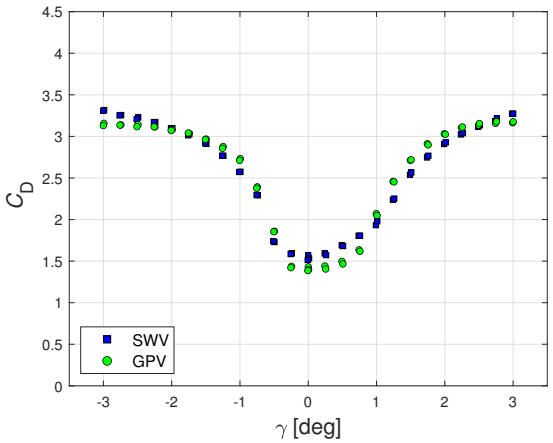

Figure 5.6: Drag coefficient (C_D) as a function of the angle of attack (γ) at Re=7.7×10^3 for arrows using vanes type SWV and GPV.

to compute the total contribution to the drag from the vanes to be $\sim 53\%$. Note that the vanes work as a key element in the stabilization of the arrow's attitude, but also add undesired drag. When the angle of attack is $\gamma = 0.75^\circ$ (+), with increasing Re an earlier transition to a turbulent state occurs, compared with $\gamma = 0^\circ$ (■). For the X10 arrow and its model in Figure 5.8b, laminar values of C_D were found in the Re-range 2.66×10^3 <Re< 2.0×10^4(■, + and ◆).

Figure 5.8 also shows the results from the free flight tests, in which the arrows' attitude cannot be controlled. The initial and final velocities were obtained from the high-speed video camera recordings. No flexural oscillation occurs in the arrows shot by the compressed air launching system [23], in contrast to those shot using a recurve bow [18]. For the A/C/E arrow (Figure 5.8a) at Re= 1.06×10^4 only laminar values of C_D (●) were obtained. As Re increases, scatter in C_D (large vertical error bars) arises indicating that the boundary layer remains laminar for some shots, whereas it becomes turbulent for others. The distribution of C_D was analysed by increasing the number of shots (Re= 1.8×10^4 for A/C/E and Re= 1.0×10^4 for X10, indicated by $\rightarrow$ in Figure 5.8). The C_D distributions are shown in the inserted histograms. The detailed conditions that allow the presence of both laminar and turbulent C_D at the identical Re remain unknown. When Re= 2.43×10^4, the small vertical error bars in Figure 5.8a indicate the dominance of turbulent boundary layers. For the X10 arrow (●) in Figure 5.8b, turbulent values of C_D were found for 1.37×10^4 <Re< 2.1×10^4.

The obtained C_D values when a national level archer, equipped with a recurve bow, performed the shots (×) are shown in Figure 5.8. The turbulent values $C_D =$ 2.69 and $C_D = 3.23$ were obtained for A/C/E (Re= 2.01×10^4) and X10 (Re= 1.75×10^4), respectively. These are introduced as turbulent C_D in the numerical

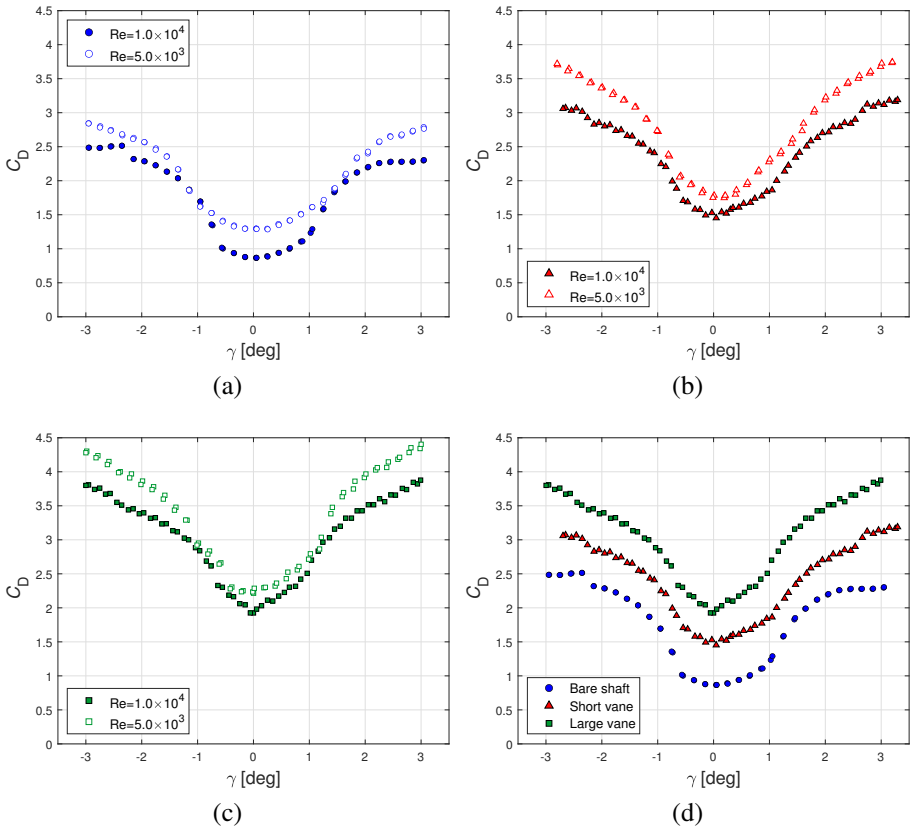

Figure 5.7: Drag coefficient (C_D) as a function of the angle of attack (γ) at Re=5.0×10^3 and 1.0×10^4 for A/C/E arrows a) without vanes (bare shaft) and using b) short straight vanes and c) large straight vanes. d) Corresponds to the arrows without vanes and using short and large straight vanes at Re=1.0×10^4.

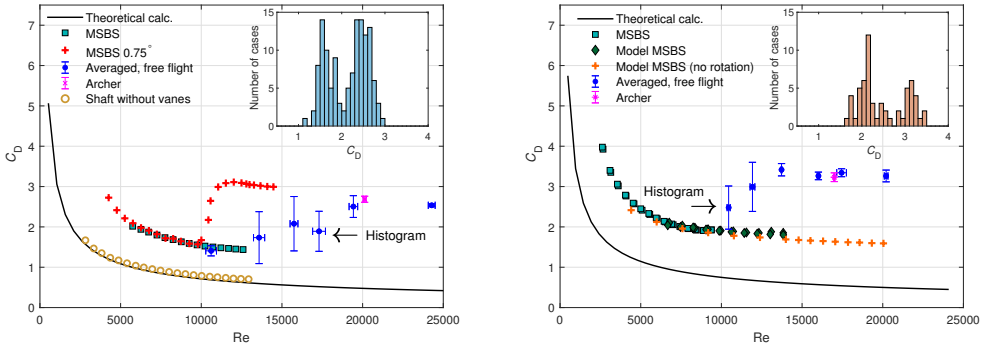

(a) (b)

Figure 5.8: C_D as a function of Re: a) A/C/E and b) X10.

computations. The ratio of the turbulent C_D multiplied by the squared values of r and V_0 for X10 to A/C/E is around 1, indicating that the drag forces exerted on the two arrows were almost identical. The averaged laminar $C_D = 1.50$ was used in the computations for the A/C/E arrow. Whereas for the X10 arrow, the laminar $C_D = 1.63$ was obtained from the MSBS tests at Re$= 1.75 \times 10^4$ (Re for the actual archer).

Figure 5.9 shows the values of C_D as a function of Re for arrows using the A/C/E shaft with the straight short and large vanes. With the solid line are shown the theoretical values corresponding to a semi-infinite cylinder with the same radius as the A/C/E shaft. The closed circles (●) represent the experimental results for the bare shaft without vanes, which shows good agreement with the theoretical result. The slight difference is attributed to the pressure drag. The closed squares (■) show the value of C_D when an arrow fletched with the short vanes was aligned with the wind flow. At Re$= 1.2 \times 10^4$, the value of C_D was almost doubled compared with the case of the bare shaft. The contribution of the drag generated by the vanes is around 50% of the total drag.

The closed triangles (▲) show the generated drag on the arrow with large vanes. Arrows with larger vanes are more stable during their flights, but larger drag is exerted on them. The open diamonds (◇) show the results when the arrow was fixed at an angle of attack of $\gamma = 0.75°$ with the wind flow. At around Re$= 1.1 \times 10^4$ there was an abrupt increase in the value of C_D. Such increase in C_D suggests the earlier transition to a turbulent boundary layer. From our experiments, it was not possible to observe in detail the boundary layer transition point, as has been observed by Park et al. [16]. Nevertheless, the attitude of the arrow was confirmed to play a key role in the transition.

Figure 5.10 compares the results obtained from the MSBS tests of the values of

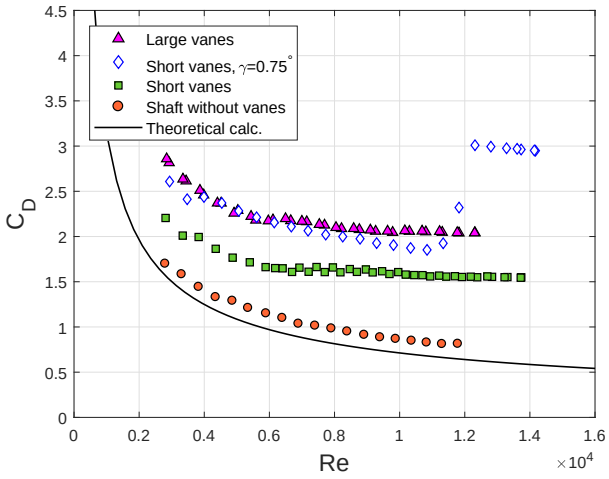

Figure 5.9: MSBS results: C_D as a function of Re for A/C/E arrows using short and large straight vanes.

C_D as function of Re for two types of A/C/E arrows with the curved SWV and with straight short vanes. It is appreciated that both types of arrow configurations show similar behaviour when they were aligned with the wind flow. For both arrows, the laminar values of the drag coefficient was $C_D \sim 1.5$ for $1.0 \times 10^4 <$Re$< 1.2 \times 10^4$. In the presence of an angle of attack ($\gamma = 0.75°$), an earlier transition from laminar to turbulent boundary layer was observed, in comparison with the cases in which the arrows were aligned with the wind flow. The transition for arrows fletched with the curved SWV occurred at a Reynolds number of Re$= 1 \times 10^4$, whereas the transition for the arrows with straight small vanes occurred at Re$= 1.12 \times 10^4$. The earlier transition for the curved arrows might arise due to the perturbation of the flow induced by the rotation of the arrow shaft. For both types of arrow configurations the turbulent drag coefficient was about $C_D = 3$ for $1.3 \times 10^4 <$Re$< 1.4 \times 10^4$.

5.4 Smoothing the acceleration sensor data

In order to obtain reliable information from the acceleration sensor data, it is important to remove the noise from the data set, allowing the important patterns to stand out. There exist different data smoothing techniques described in the literature, each of them with advantages over the others and differing in their concepts. In the current work two different methods were tested. The first is the moving weighted average (Figure 5.11a), which is a simple method to smooth the experimental data by replacing a data point ($0.5 \times a_i$) with the weighted average of its two neighbours ($0.25 \times a_{i-1}$ and $0.25 \times a_{i+1}$). The moving weighted average is a

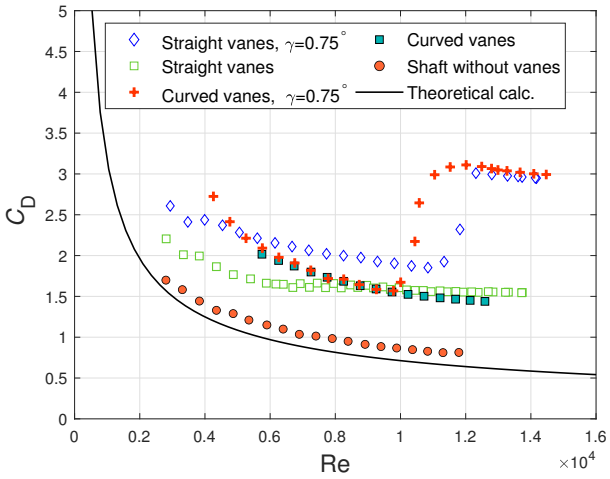

Figure 5.10: Drag coefficient (C_D) as a function of the Reynolds number (Re) for arrows using straight short and curved vanes.

type of low pass filter in which the higher frequencies are attenuated. The second type of method is the Savitzky-Golay filter. In this case, each value of the data set is replaced with a new value obtained from a polynomial approximation fit to $2n+1$ neighbouring points. Where $n = 2$, i.e. a second order polynomial is used. Due to such characteristic, the Savitzky-Golay filter is also named a digital smoothing polynomial filter. Figure 5.11 shows several examples where a weighted average filter (Figure 5.11a) and a Savitzky-Golay filter using polynomials of different degree, second (Figure 5.11b), third (Figure 5.11c) and fifth (Figure 5.11d), are implemented. Note that a higher degree polynomial makes it possible to achieve a high level of smoothing without the attenuation of data features. In the current work, a 5th order polynomial is used in the Savitzky-Golay filter to smooth the acceleration sensor data. Figure 5.11 shows the normalized deceleration experienced by an arrow in free flight for a shot with an initial velocity $V_0 = 57.9$ ms^{-1}.

5.5 Instantaneous deceleration and velocity measured with the acceleration sensor

Figure 5.12a shows the measured instantaneous deceleration ($\alpha > 0$) experienced by the arrows in the x' direction for multiple shots with different initial conditions. In the free flight tests with the acceleration sensor the A/C/E arrows with large and short straight vanes were tested. Since the initial velocity (V_0 at t=0) is known from the high-speed video camera recordings' analysis, the instantaneous velocity

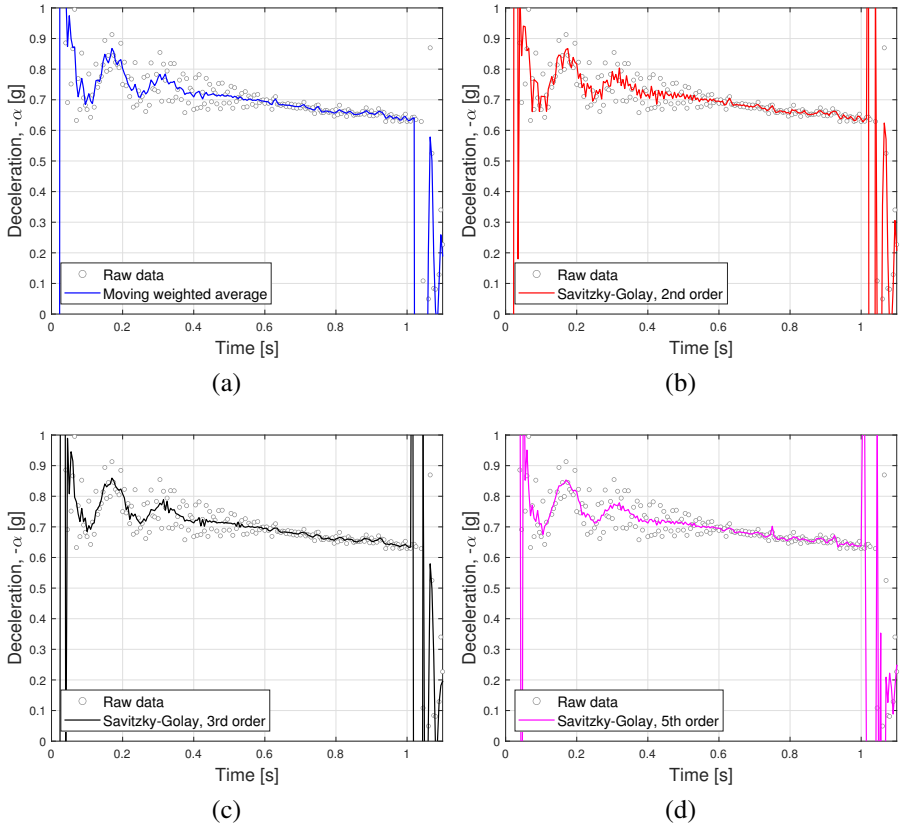

Figure 5.11: Smoothed data using a) a moving weighted average, b) the Savitzky-Golay 2nd order, c) the Savitzky-Golay 3rd order and d) the Savitzky-Golay 5th order corresponding to a shot with an initial velocity $V_0 = 57.9$ ms^{-1}.

(V_{inst}) was computed by integrating the deceleration information with

$$V_{\text{inst}}(t) = V_0 - \int_0^t \alpha(t')\mathrm{d}t'. \tag{5.3}$$

The end velocity is obtained by $V_{\text{end}} = V_{\text{inst}}(t_{\text{end}})$, where the arrow hits the target at $t = t_{\text{end}}$. The computed instantaneous velocity was plotted in Figure 5.12b. Figure 5.13 shows the instantaneous value of the drag coefficient, C_{D}, computed as

$$C_{\text{D}} = \frac{F_{\text{D}}}{0.5\pi\rho_{\text{air}} r^2 V_{\text{inst}}^2}, \tag{5.4}$$

where ρ_{air} is the air's density and the instantaneous drag force is $F_{\text{D}} = M\alpha$ and M is the total mass of the arrow.

Let us discuss first the results corresponding to arrows using small straight vanes. Relatively low deceleration, less than 0.2 g, is experienced by an arrow with initial velocity $V_0 = 34.1$ ms^{-1} during the whole flight. The shots were carried out in the 17.7 m archery range. The flying time was around 0.5 s. In Table 5.5 all the initial and end velocities for the considered shots are shown. Further, the initial and end kinetic energy (with the percentage of retained energy) and the flying times are listed. The relatively small values of drag coefficient of $C_{\text{D}} = 1.6$ (Figure 5.13) correspond to a laminar boundary layer flow along the whole trajectory. Note the good agreement with the results obtained from the MSBS tests for the laminar case.

When the initial velocity was increased up to $V_0 = 44.7$ ms^{-1} in a shot carried out in the 17.7 m range, a non-uniform deceleration was experienced during the entire arrow's flight. In such a case, the deceleration ranged from around 0.22 g to 0.5 g. The obtained values of C_{D} indicated a typical behaviour of a boundary layer in transition (Figure 5.13).

When the initial velocity was increased up to $V_0 = 59.1$ ms^{-1} in a shot carried out in the 55 m archery range, the deceleration exerted on the arrows increased up to 0.8 g. The initial and final velocities were $V_0 = 59.1$ ms^{-1} and $V_{\text{end}} = 52.7$ ms^{-1}, respectively, which represents a retained kinetic energy of 79.6%. For these shots, turbulent values of around $C_{\text{D}} = 2.6$ were obtained for the Reynolds number range $1.8 \times 10^4 <$Re$< 2.1 \times 10^4$.

The shots with initial velocities $V_0 = 53.8$ ms^{-1} and 52.9 ms^{-1} shown in Figure 5.12a, experienced similar magnitudes of deceleration for $t < 0.5$ s. Note that for the shot with $V_0 = 52.9$ ms^{-1}, during 0.6 s$< t <$ 0.8 s, the experienced deceleration reduces to around 0.3 g, which may indicate a relaminarization of the

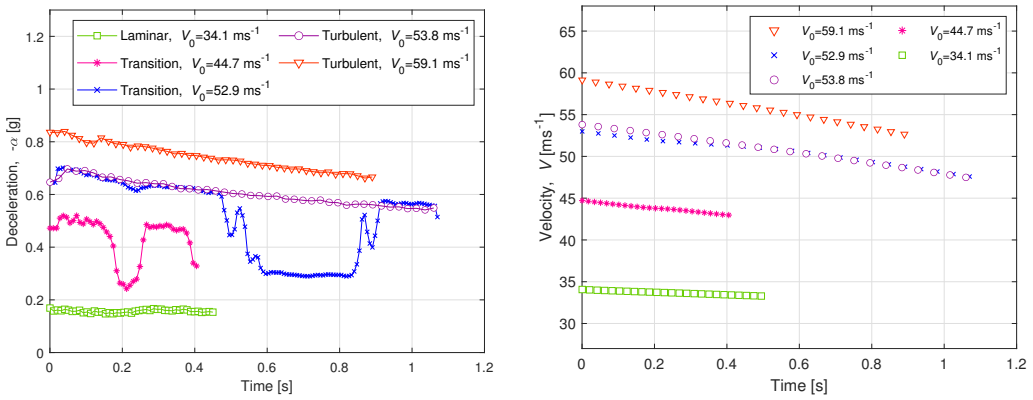

(a) (b)

Figure 5.12: Free flight experiments: a) time evolution of the arrow's deceleration and b) time evolution of the arrow's velocity for an A/C/E shaft and short straight vanes.

boundary layer during the latter half of the arrow's flight. The rapid change in the exerted force on the arrow might be characteristic of a boundary layer transition. The shot with $V_0 = 53.4$ ms^{-1} showed values of C_D corresponding to a turbulent boundary layer flow during the entire flight. A larger percentage of the kinetic energy was delivered to the target by the arrow which experienced a re-laminazarization during free flight.

From Figure 5.13, it is possible to appreciate that the transition zone from a laminar to a turbulent flow was found to be in the Reynolds number range $1.45 \times 10^4 < \text{Re} < 1.8 \times 10^4$. Only turbulent values of C_D were found for $\text{Re} > 1.8 \times 10^4$. In general, good agreement was found between the data provided by the MSBS and the obtained using the acceleration sensor.

Figure 5.14 shows C_D as a function of Re obtained for arrows with the streamlined point compared with a shot of an arrow with the bulge point. Observe that even at high Re$\sim 2.0 \times 10^4$, laminar values of $C_D \sim 1.3$ were found for the arrows using the streamlined point. Whereas only turbulent values $C_D \sim 2.7$ were found for the arrows with bulge points at similar Re. These findings agree with the results of Miyazaki et al.[23] and Park et al.[29], where it is noted that the shape of the point is crucial to determine the boundary layer characteristics. Park et al. indicated that when using bulge points at Re$= 2.74 \times 10^4$, the flow separation occurred in the area of maximum diameter and the recirculation area was located where the point and the shaft joint. Downstream of the recirculation area, the boundary layer was turbulent. By using the streamlined point the boundary layer transition appears to be retarded, allowing the presence of laminar boundary

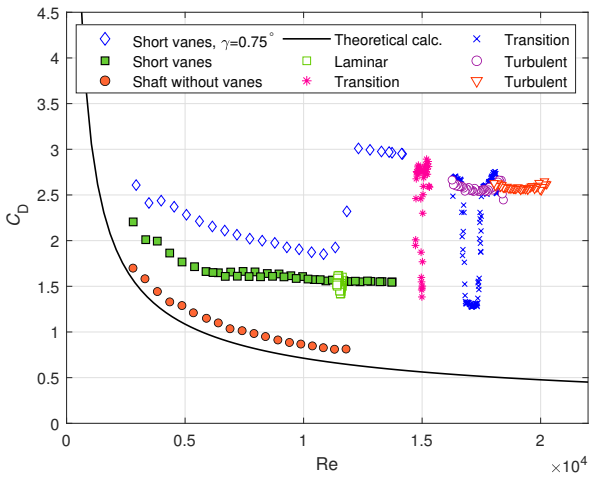

Figure 5.13: C_D as a function of Re for arrows using the A/C/E shaft with short straight vanes.

layers even at large values of Re. By carefully choosing the type of point, the archers might be able to control the boundary layer transition.

In Figure 5.15 we show the obtained instantaneous deceleration and velocity for A/C/E arrows using large straight vanes. Four different shots carried both in the 17.7 m and 55 m archery ranges were considered. It is observed that when a shot with initial velocity $V_0 = 31.7$ ms^{-1} was performed, a deceleration of less than 0.2 g was experienced along most of the trajectory. Therefore relatively low values of C_D were obtained (Figure 5.16). Nevertheless, it is possible to observe large scattering in C_D at around Re=1.15×10^4. For such a Re, the laminar values from the MSBS was around $C_D = 2$, whereas in the the case of the data provided by the acceleration sensor the magnitude of the drag coefficient was found to scatter in the range $1.85 < C_D < 2.7$. When the initial velocity was increased up to $V_0 = 36.8$ ms^{-1}, the deceleration changes in the range 0.2 g to 0.4 g. The scattering of the C_D values increased to be in the range $2 < C_D < 3.3$ at Re=1.25×10^4. The large scattering in C_D was attributed to a boundary layer flow transition. Note that the transition region for arrows using large straight vanes occurs at lower Re compared to those arrows using short straight vanes.

Two shots with a similar initial velocity of around $V_0 = 49.6$ ms^{-1} were carried out in the 55 m archery range. It is possible to observe in Figure 5.15 that the aerodynamic load exerted for those two shots were appreciably different. In the first of the shots a deceleration less than 0.4 g was experienced along the entire trajectory of the arrow and monotonically decreasing with time. Whereas in the second shot, a larger deceleration located in the range $0.45g < \alpha < 0.6g$ was observed. Using the instantaneous deceleration and velocity information, it was

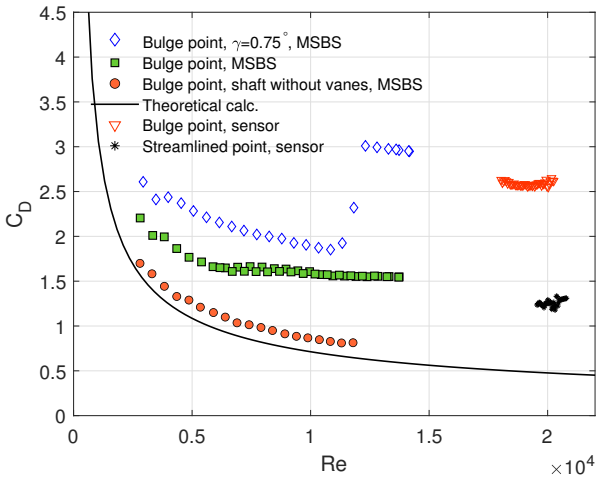

Figure 5.14: C_D as a function of Re for arrows using the A/C/E shaft with short straight vanes and streamlined point.

Table 5.5: Initial velocity (V_0), kinetic energy (KE) and flying time measured with the acceleration sensor for arrows fletched with short vanes.

V_0 [ms^{-1}]	V_{end} [ms^{-1}]	KE $_0$ [J]	KE $_{end}$ [J]	Rtnd. KE [%]	Flying time [s]
34.1	31.3	8.3	7.0	84.3	0.50
44.7	43	14.3	13.2	92.3	0.40
52.9	47.6	20.0	16.2	81.0	1.08
53.8	47.5	20.7	16.2	78.3	1.07
59.1	52.7	25.0	19.9	79.6	0.89

possible to compute the values of C_D as a function of Re. From Figure 5.16, it is possible to observe that those two different behaviours correspond to separately laminar and turbulent flows at relatively large Reynolds numbers of Re $> 1.5 \times 10^4$. The percentage of retained kinetic energy during the flight was 84% and 77.1% for the complete laminar and turbulent cases, respectively (Table 5.6). The presence of shots with both laminar or turbulent boundary layer flows at the same Re suggest that the transition takes place at this Re range. The magnitude of the velocity is not the only factor that determines the state of the boundary layer, as observed. The orientation of the arrow with respect to its movement plays a determinant role to trigger the laminar-turbulent transition mechanism. In Chapter 6 such idea is explored by complementing the experimental results with the numerical simulations.

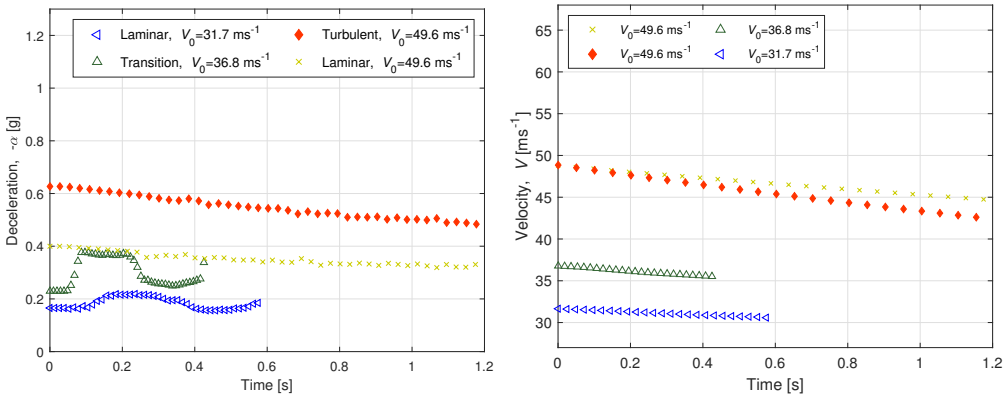

(a) (b)

Figure 5.15: Free flight experiments with arrows fletched with large straight vanes: a) time evolution of the arrow's deceleration and b) time evolution of the arrow's velocity.

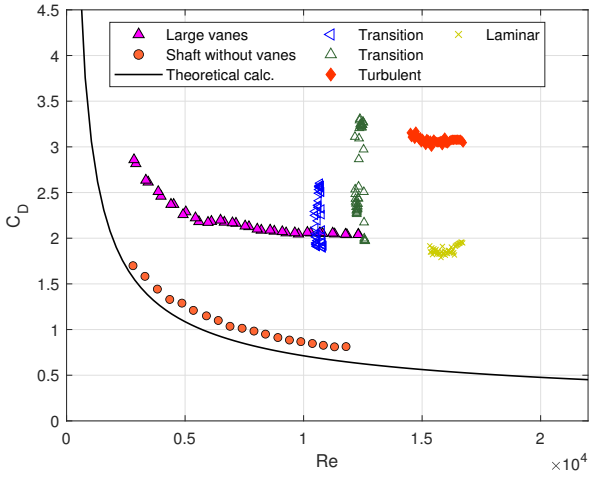

Figure 5.16: C_D as a function of Re for arrows using the A/C/E shaft with large straight vanes.

Table 5.6: Initial velocity (V_0), kinetic energy (KE) and flying time measured with the acceleration sensor for arrows fletched with large vanes.

V_0 [ms^{-1}]	V_{end} [ms^{-1}]	KE $_0$ [J]	KE $_{end}$ [J]	Rtnd. KE [%]	Flying time [s]
31.7	30.6	7.7	7.2	93.5	0.56
36.8	35.5	10.4	9.6	92.3	0.42
49.6	43.6	18.8	14.5	77.1	1.2
49.6	47.1	18.8	15.8	84.0	1.14

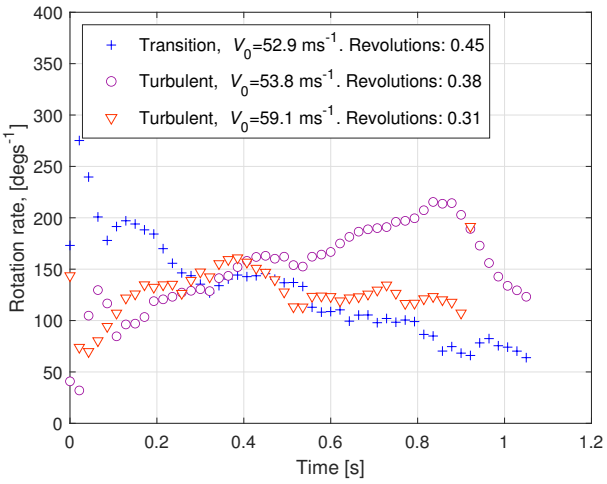

Figure 5.17: Instantaneous rotation rate measured with the acceleration sensor for arrows using short vanes.

5.6 Instantaneous rotation rate measured with the acceleration sensor

In this section the rotation rates of A/C/E arrows using short straight vanes are analysed. The rotation rates were obtained from the acceleration sensor measurements. Here three cases previously studied in Section 5.5 are considered. The studied shots were performed in the 55 m archery range and correspond to the cases with transition and turbulent boundary layers. For all the cases, low rotation rates were found. The arrows barely completed one revolution around their axes. Such low rotation rate was realized by fletching the arrows with the short straight vanes. For arrows using SWV, appreciably larger rotation rates might be expected (Table 5.3). Since the rotation rate was pretty similar in the three studied cases, it is not possible to find any correlation between the rotation rate and the transition from laminar to turbulent boundary layer from the acceleration sensor information. Further theoretical studies must be carried out to explore the influence of the rotation rate in the mechanism of boundary layer transition.

Chapter 6

Results from the numerical computations

The current chapter provides the results from the computations of the equations of arrow motion described in Chapter 4. The initial conditions and the characteristics of the background wind are also described. In the first part of this chapter, the results obtained from the acceleration sensor for an A/C/E arrow with straight short and large vanes are compared with the numerical simulations which also provides a validation of the mathematical model.

Later in this chapter, shots carried out in a 70 m archery range with the A/C/E and X10 arrows with attached bulge points and SWV are simulated. Those arrows' configurations were chosen because in the actual archery competitions the archers would choose SWV over straight vanes. The rotation provided by the SWV would stabilize the arrows in a better way than if straight vanes were used.

Several types of background winds were considered in the numerical computations. Firstly, a uniform-type background wind was taken into account. Such wind type corresponds to a behaviour in which the wind velocity remains unchanged along the whole trajectory of the arrow. The wind velocity remains constant regardless the position of the arrow. Side-, head- and tail-winds with different magnitudes were studied.

Secondly, a non-uniform type wind was considered in the computations. Here we proposed a sinusoidal-type wind behaviour in which the side component of the velocity changes with position, having a maximum at the center of the archery range. In this type of wind, the flying arrows would experience a different type of wind than the archer. Since the position of the archer is fixed in the shooting area, the arrows are subjected to an unknown wind behaviour. The latter is important because this might be a common situation that could arise during outdoor archery competitions in which the velocity field of wind gusts may change rapidly. The arrows' attitude and trajectory are then affected by the wind properties that the

archer can not feel at the moment of performing the shots.

Finally, actual background wind characteristics were considered in the computation of the equations of arrow motion. Here we considered the wind characteristics from the location where the Olympic archery competition is supposed to take place in the summer Tokyo Olympic Games. Such wind information was computed and provided by the Japan Agency for Marine-Earth Science and Technology (JAMSTEC) using a Large Eddy Simulator (LES). The most important characteristic under such wind behaviour is the time and position dependency of the wind velocities. The latter allowed us to test the response of different arrow configurations to various realistic background wind conditions. In order to obtain results that describe the actual behaviour of arrows used in real competitions, the physical and aerodynamic properties described in Chapters 3 and 4 were considered.

6.1 Initial conditions

In this section the initial conditions necessary to carry out the numerical computations are given. The set of initial conditions is given by the initial arrow's center of mass position (x_0, y_0 , z_0), the initial velocity (V_0), the initial arrow's attitude or orientation ($\Theta_0, \theta_0, \Phi_0$, ϕ_0) and the initial angular velocities with respect to the z and y axes (ω_ϕ, ω_θ). Shots in three different archery ranges were simulated. The considered cases for the numerical computations are firstly shots carried out in the 17.7 m and 55 m, as in the experimental procedures. The latter to compare the results from the numerical computations and the data obtained from the experimental procedures for validation of the mathematical model. Finally, shots carried out in 70 m archery ranges were simulated to reproduce the conditions occurring during actual archery competitions. The initial conditions are given separated in the following subsections for clarity.

6.1.1 Arrow's center of mass

The initial position of the arrow's center of mass is given by $x_0 = 0$ and $y_0 = 0$. The initial arrow's vertical distance from the floor is $z_0 = 0.3$ m and $z_0 = 1.5$ m for the cases corresponding to the simulated free flight tests and in the actual archery competition, respectively. The vertical height of the target was $z_{\text{tar}} = 1.3$ m.

6.1.2 Arrow's attitude and velocity

The initial orientation or attitude of the arrow is given by the angles Θ_0,θ_0,Φ_0 and ϕ_0. The initial arrow's attitude is crucial in the evolution of the fluid flow around

the arrow's body and therefore in its dynamics during free flight. On the one hand, the angles Θ_0 and θ_0 were obtained from the recorded videos during the free flight tests and used as input parameters in the numerical computations corresponding to the shots that took place in the archery ranges with 17.7 m and 55 m. On the other hand, for the simulated shots taking place in the 70 m archery range, the value of Θ_0 was obtained by carrying out an iterative process so that under no wind conditions the arrow hits the center of the target.

As for the case of the orientation with respect to the x axis, during the experimental procedures the arrows were carefully aligned horizontally with the center of the target so that $\Phi_0 = \phi_0 = 0$.

The initial velocity (V_0) was obtained from the high-speed video camera recordings for every shot in the experimental procedures. It was verified that the velocity decay from the shooting point to the camera position (2 m) is less than 1%. Whereas in the simulated shots in the 70 m archery range were taken into consideration the typical values of $V_0 = 57.3$ ms^{-1} and $V_0 = 56.7$ ms^{-1} for the A/C/E and X10 arrows using SWV, respectively.

6.1.3 Arrow's angular velocity

The angular velocity of an arrow as it leaves the bow has an important role in determining the the dynamics of the arrows during free flight. It has been studied the influence of the initial arrow's attitude in developing angles of attack close to zero by Park [26, 27, 28] and Zanesvky [37]. In Chapters 5 and 6 the importance of the magnitude of the angle of attack is discussed. Further, during actual archery shots, a non-zero angular velocity is necessary for the arrow to clear the bow without undesired contact.

In the current work two sets of initial angular velocities are analysed. In the first, the initial angular velocities with respect to z and x (the initial rate of change of θ and ϕ with respect to z and x, respectively) are zero. Such conditions at the beginning of the shot are the so called zero initial angular velocities and can be expressed as $(\mathrm{d}\boldsymbol{n}/\mathrm{d}t)_0$=0 or

$$\omega_{\phi 0} \quad = \quad \omega_{\theta 0} = 0. \tag{6.1}$$

In the second set of initial conditions, the initial angular velocities are considered to be non zero and have the precise magnitude so that that the arrow's axis approximately aligns with $\boldsymbol{V}$ or $(\mathrm{d}\boldsymbol{n}/\mathrm{d}t)_0$=$[\mathrm{d}(\boldsymbol{V}\,|\boldsymbol{V}|^{-1})/\mathrm{d}t]_0$ under the still-air conditions. Whereas when the background wind is considered the ideal initial angular velocities can be expressed as $(\mathrm{d}\boldsymbol{n}/\mathrm{d}t)_0$=$[\mathrm{d}(\boldsymbol{V}-\boldsymbol{U})|\boldsymbol{V}-\boldsymbol{U}|^{-1}/\mathrm{d}t]_0$. If the ideal initial angular velocities are achieved during the shooting stage, the angle

of attack remains close to zero and therefore a laminar boundary layer might be developed, as shown in Chapters 5 and 6. Nevertheless, the precise control by the archers of the initial angular velocities appears to be highly challenging in actual competitions.

6.2 Results corresponding to computations considering the still-air conditions

The current section contains the results from the numerical computations under the still-air conditions. Therefore, the influence of the background wind is not taken into account in the following results.

6.2.1 Decay of the velocity and increasing in Θ and θ at the different camera positions

Figure 6.1 shows the computation of the percentage of decay in the velocity at three distances from the shooting positions (1.5 m, 2.5 m and 3.5 m) as function of the initial velocity, V_0, for A/C/E arrows with SWV and in still air conditions. Such distances correspond to the different positions at which the high-speed video cameras were located. For the three cases the change in the velocity are of the order of around 1%. Despite the small decay percentage in the velocity measurement at the camera positions, such difference must be taken into consideration when defining the initial velocities for each simulated shot. Along all the present work such considerations were taken into account.

Figure 6.2 shows the increase of the angles Θ and θ in percentage at the same three mentioned positions for different initial velocities. It can be observed that the difference $\Theta - \theta$ increases as the arrows moves downrange. Such differences become smaller as the initial velocity increases. The rate of change of Θ and θ is a dominant factor for the flight characteristics of the arrows as well as for the transition of the boundary layer flow. Therefore, it is of great importance to measure such quantities in a precise way using the high-speed video camera recordings. Once the values of Θ and θ were obtained from the video recordings at the camera positions, the actual Θ_0 and θ_0 were computed.

6.2.2 Arrow's attitude under still-air conditions

In the current section, the time evolution of the pitch and yaw angles developed under still air conditions is studied. Recall from Figure 4.1 that during the pitch and yaw, the arrows rotate around the y and z axes, respectively. We consider an

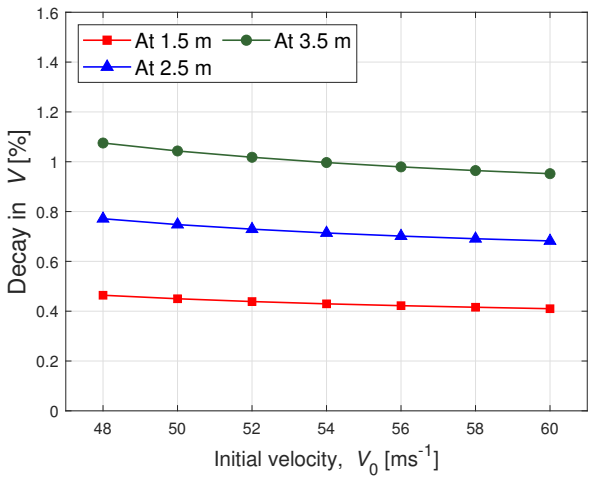

Figure 6.1: Decay of velocity V at 1.5 m, 2.5 m and 3.5 m.

A/C/E arrow with a bulge point and the straight short (Figure 6.3a) and large vanes (Figure 6.3b). Two different initial velocities were considered for both types of arrows to study the influence of the initial conditions on the arrow's dynamics. The considered initial velocities were $V_0 = 53$ ms^{-1} and $V_0 = 59$ ms^{-1}. The shots were simulated for a a 55 m archery range.

Figure 6.3 shows the time evolution of the pitch and yaw angles for both types of arrow configurations with the different initial velocities. Observe that the pitch angles were several orders of magnitude larger than the yaw angles in all the cases. Yaw angles close to zero were developed during the complete simulated arrows' flights. Note that the amplitude of the angles reduces with increasing velocity for both types of arrows. The latter is explained partially by the fact that the pitching moment is proportional to the square of the velocity, as shown in Equation 2.3. With a larger pitching moment exerted on the arrows, larger lift is exerted likewise, which brings about a reduction of the pitch angle. In Section 6.2.5 the importance of the magnitude of the pitching moment and lift exerted on the arrows is explored in detail.

Observe that the arrows with large vanes (Figure 6.3b) have more stable flights than those arrows with short vanes (Figure 6.3a). This arises from the larger total area that generates a larger pitching moment exerted on the arrows. Again, the lift here plays an important role to enhance the damping in the arrows' oscillatory movement during free flight. Such consideration must be taken into account by the archers in deciding the types of vanes.

Figure 6.4 shows the time evolution of the angles of attack (γ) for shots under the previously described conditions. As seen from Figure 6.3, the arrows' movements take place mainly in the vertical plane, rotating around the y axis.

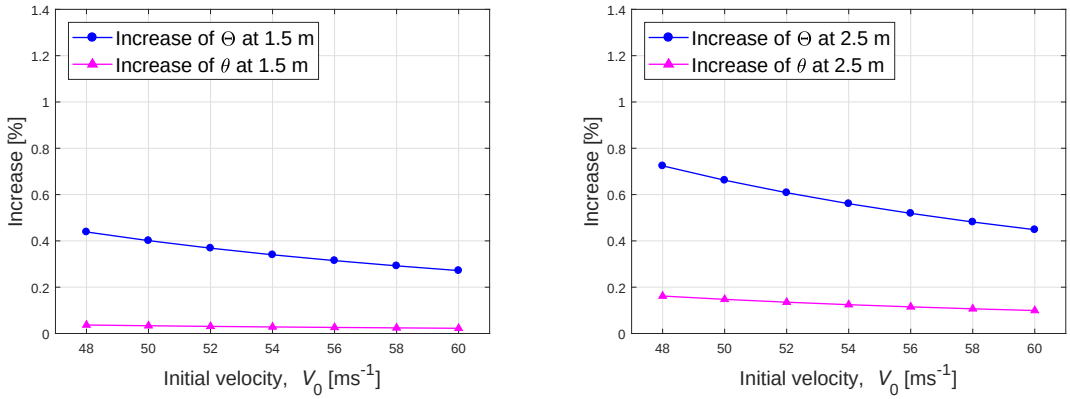

Figure 6.2: Increase in angles θ and Θ [%] at a) 1.5 m, b) 2.5 m and c) 3.5 m.

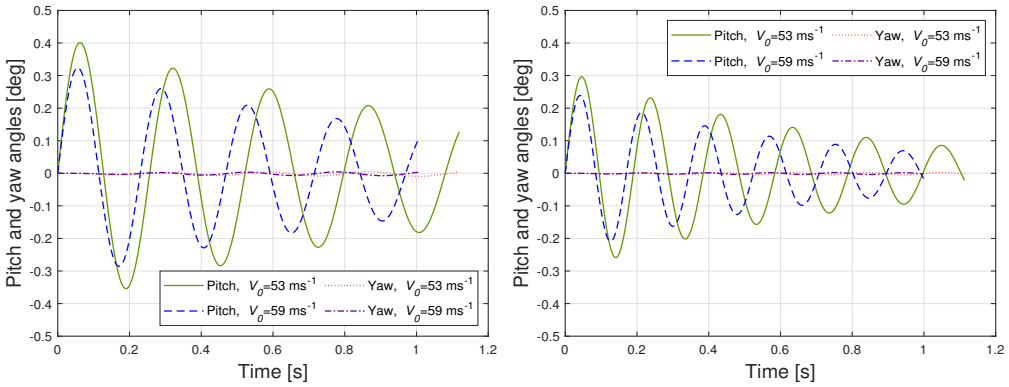

(a) (b)

Figure 6.3: Time evolution of the pitch angle ($\Theta - \theta$) for arrows with a) short and b) large vanes with initial velocities V_0=53 ms^{-1} and V_0=59 ms^{-1}.

Therefore, the angle of attack for these cases was $\gamma \sim |\Theta - \theta|$, where $\Theta - \theta$ is the pitch angle. Further, the angle of attack is a crucial influence that triggers the laminar-turbulent boundary layer transition, as seen in Figure 5.5. Smaller values of γ are desirable to keep the drag exerted on the arrows as low as possible. Although the larger vanes generate smaller values of γ, it is also important to note that the drag generated is proportional to the vanes' area.

6.2.3 Unexpected boundary layer transition during free flight

Figure 6.5 shows the time evolution and the striking points of the archery arrows when the ideal angular velocities were set for an A/C/E arrow with SWV. Still-air conditions were considered in the computations. When the boundary layer remained laminar (●), the striking point is almost in the center of the target, as the archers may expect. Nevertheless, when there existed an unexpected transition to turbulent boundary layer (■) at t_{trans}=0.15 s, the arrow deviated vertically by $\delta z = 0.29$ m. Such a sudden drop is induced by the unexpected boundary layer transition, while the archer would assume that the boundary layer remains laminar during the whole arrow's flight. In a real competition, such unanticipated transition might be triggered by the unknown wind conditions along the archery range. Assuming a turbulent boundary layer during the entire trajectory might be wiser for archers to obtain better shots.

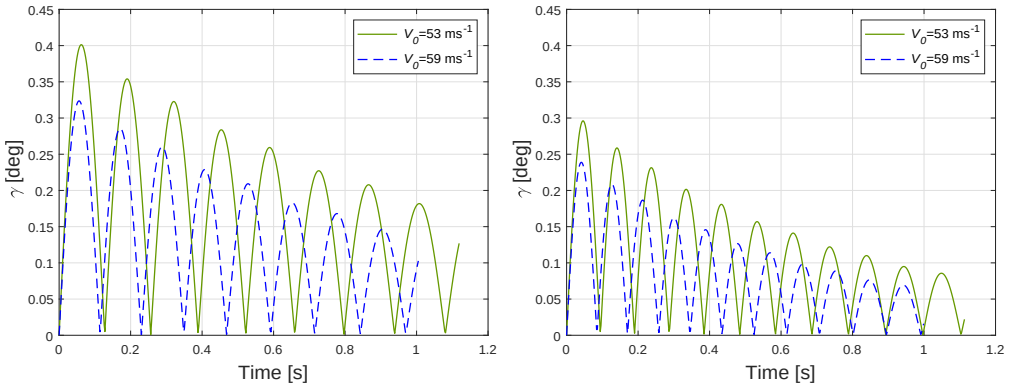

Figure 6.4: Time evolution of the angle of attack (γ) for arrows with a) short and b) large vanes with initial velocities V_0=53 ms^{-1} and V_0=59 ms^{-1}.

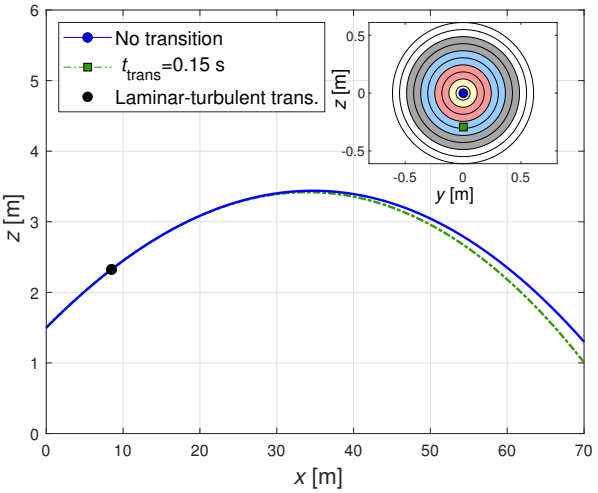

Figure 6.5: Shots without transition and with transition to turbulent boundary layer at t_{trans}=0.15 s during free flight, using the ideal initial angular velocity.

6.2.4 Influence of the time-dependent and constant values of C_D

In the current section the results obtained from the acceleration sensor and compared with the numerical simulations are discussed. The data from the acceleration sensor correspond to the A/C/E arrow with straight short vanes and with a bulge point (Figure 5.12 in Chapter 5). Here we show the differences in the trajectory and the arrows' attitude when in the numerical computations the values of the drag coefficient, C_D, were considered to be constant along the complete arrow's trajectory and when the time-dependent values of C_D, obtained from the acceleration sensor, were taken into account. From the data plotted in Figure 5.12, the two shots that had only turbulent behaviours with initial velocities $V_0 = 53.8$ ms^{-1} and $V_0 = 59.1$ ms^{-1} were selected. Figures 6.6a and 6.6b illustrate the time evolution of the angle of attack, γ, for the slower ($V_0 = 53.8$ ms^{-1}) and the faster shots ($V_0 = 59.1$ ms^{-1}), respectively. In the inserted panel we show the impact points for the mentioned shots in a target located at 55 m from the shooting position and 0.8 m from the floor.

When the constant value of the drag coefficients was taken into account in the computations, the turbulent value of $C_D = 2.6$ was assumed along the entire trajectory of the arrows. Whereas in the time-dependent scenario, the computed values obtained from the acceleration sensor (Figure 5.12) were introduced in the simulation.

For the slower case in Figure 6.6a, the difference between the impact points of the time-dependent and constant scenarios was 40×10^{-3} m, whereas such difference was negligible for the faster case in Figure 6.6b. A final difference of 40×10^{-3} m might be important in the archery competition. By considering the time-dependent C_D values in the computations, it is possible to obtain results that adjust to actual shots. No significant difference can be appreciated in the time evolution of the angle of attack in the analysed cases.

Figure 6.7 shows the time evolution of the pitch and yaw angles, considering the constant and time-dependent values of C_D for the slower (Figure 6.6a) and the faster (Figure 6.6b) shots. As in the angle of attack, the magnitude of pitch and yaw angles were not affected considerably by the instantaneous change of the C_D value. The values of the pitch angles were several orders of magnitude larger than the values of the yaw angles for all the cases.

6.2.5 The influence of the parameters α and β

The influence of the parameters α and β in the dynamics of the archery arrows is studied in this section. The simulations were carried out for an A/C/E arrow with SWV. Nevertheless, it was confirmed that the results presented in this sec-

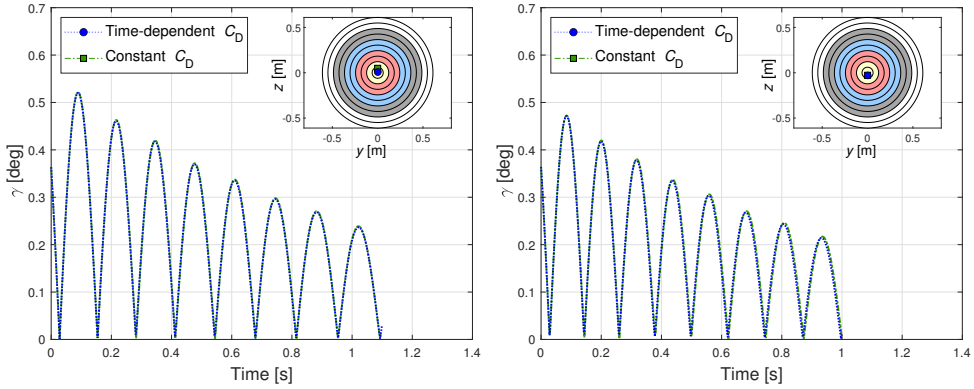

(a) (b)

Figure 6.6: Comparison of the time evolution of the angle of attack when the value of C_D is considered constant and variable for shots with initial velocities a) $V_0 = 53.8$ ms^{-1} and b) $V_0 = 59.1$ ms^{-1} with the impact points on a target located at 55 m from the shooting position and 0.8 m from the floor.

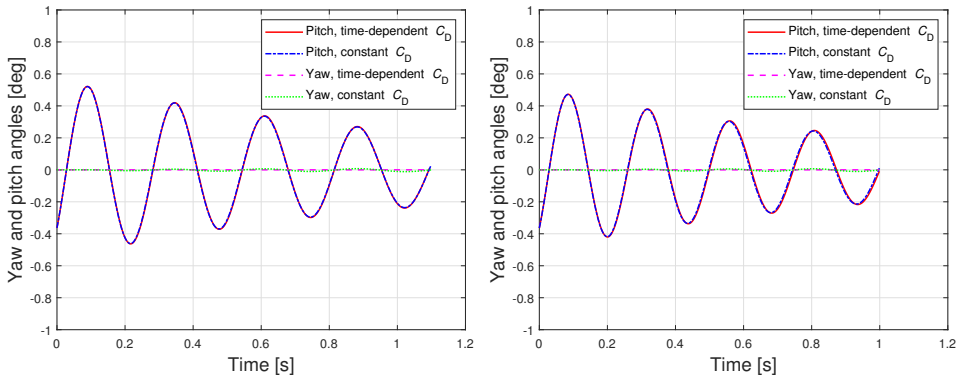

(a) (b)

Figure 6.7: Comparison of the time evolution of the pitch and yaw angles when the value of C_D is considered constant and variable for shots with initial velocities a) $V_0 = 53.8$ ms^{-1} and b) $V_0 = 59.1$ ms^{-1}.

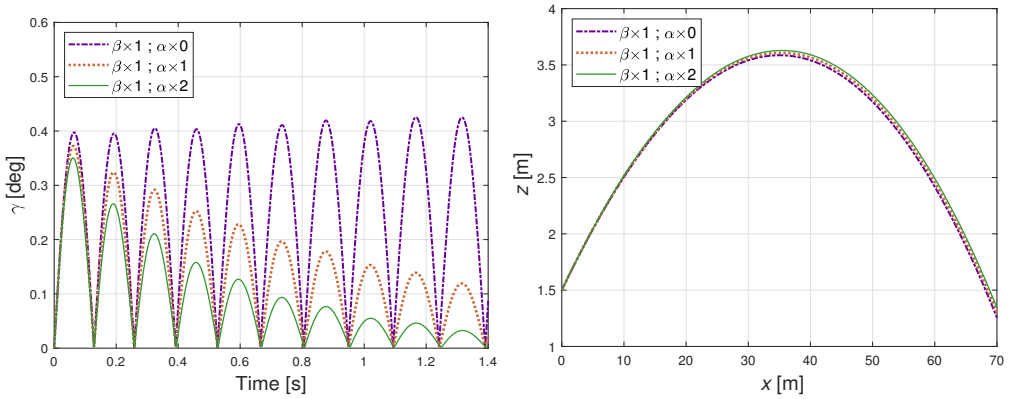

(a) (b)

Figure 6.8: a) Time evolution of the angle of attack and b) trajectory of the arrow when α is changed whereas β remains constant in still air using an A/C/E arrow.

tion apply as well for the other arrow configurations. The parameters α and β are related with the lift coefficient (C_L) and the pitching moment coefficient (C_M) through Equations 5.1 and 5.2. In Figure 6.8a, β was kept constant whereas α was taken to be zero, its original value and twice that value. If no lift was exerted (α=0) the oscillation in the angle of attack, γ, would prevail with almost constant amplitude. When the value of α was doubled, the amplitude decay rate increased and γ reduced faster than in the case when α had its regular value. The lift exerted on the vanes of the arrows contribute to their stabilization by reducing the magnitude of γ during the flight. In Figure 6.8b the trajectories for the cases previously mentioned are shown. The arrows' striking points were computed to be around 0.04 m below and over the center of the target for the cases when α was zero and twice the original value, respectively.

Figure 6.9a shows the time evolution of γ and the trajectory followed by the arrow when α remained constant. Here β was considered to be zero, its original value and doubled. From Figure 6.9a is possible to observe that if the pitching moment were considered to be zero, γ would increase monotonically. Note the change in the order of magnitude of γ. The oscillatory behaviour in γ arises as a result of the pitching moment exerted on the arrows. The oscillation frequency increases with the pitching moment (inserted panel in Figure 6.9a). Figure 6.9b shows that the arrows with negligible pitching moment would experience uncontrolled flights provoked by the increasing γ. Such behaviour would be a convenient result in other sporting projectiles, e.g. the javelins. In javelin throw, one tries to maximize the range of the projectile. For javelins the induced pitching moment during free flight is almost negligible [12, 13].

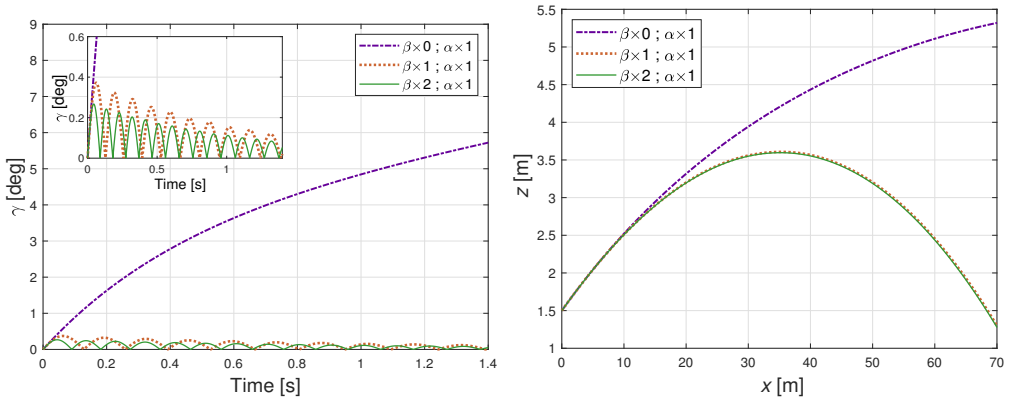

(a) (b)

Figure 6.9: a) Time evolution of the angle of attack and b) trajectory of the arrow when α remains constant whereas β is changed in still air using an A/C/E arrow.

6.2.6 Velocity decay under still air conditions

Figure 6.10 shows the velocity decay under still-air conditions for the A/C/E and X10 arrows shot with an arbitrary initial velocity of $V_0 = 57$ ms^{-1} using zero and ideal initial angular velocities in a 70 m archery range. It is possible to appreciate that arrows that keep an angle of attack close to zero, and therefore a laminar boundary layer, deliver more energy into the target than those with a turbulent boundary. The latter effect arises from the fact that larger drag is exerted on the arrows turbulent boundary layers. The percentages of retained velocity were found to be of around 84% and 91% for A/C/E arrows with turbulent and laminar boundary layers, respectively. Whereas for the X10 were 88% and 94% for the arrows with turbulent and laminar boundary layers, respectively. The X10 arrows appear to be more efficient in retaining larger amounts of their kinetic energy than A/C/E arrows.

6.2.7 Oscillation frequency and amplitude decay rate of the angle of attack

In order to explore in more detail the influence of the initial launching velocity in the dynamics of the arrows, the oscillation frequency and the amplitude decay rate were of the angle of attack (γ) computed under the still-air scenario using zero initial angular velocities. The results are shown in Figure 6.11a. Increasing V_0 leads to higher oscillation frequency as a consequence of the larger pitching moment exerted on both arrows. For A/C/E, the average oscillation frequency increased monotonically from 3.16 Hz to 4.52 Hz as the initial velocity increased from 50

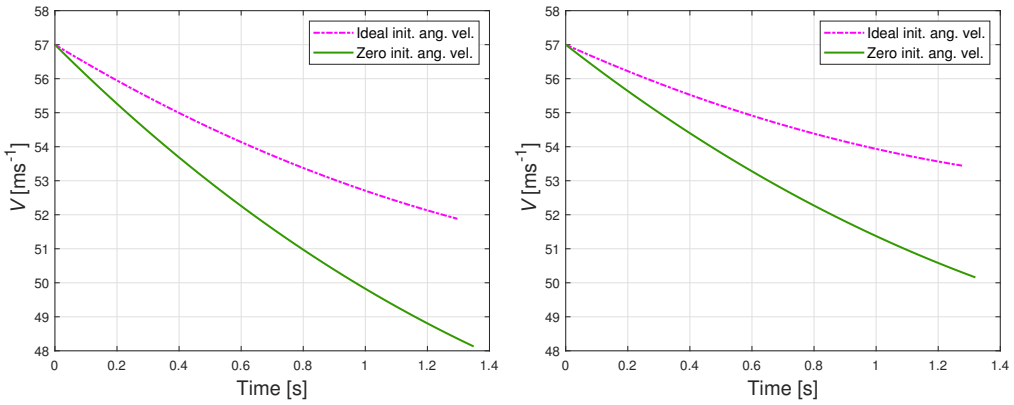

(a) (b)

Figure 6.10: Time evolution of the velocity for shots with the ideal and zero initial angular velocities at still-air conditions for a) A/C/E and b) X10 with SWV.

ms^{-1} to 71 ms^{-1}. In the case of the X10 arrow, the oscillation frequency increased from 3.02 Hz to 4.32 Hz in the same V_0 range. The A/C/E arrow provides larger stabilizing effects than the X10 under still-air conditions

In Figure 6.11b we show the decay rate of the damped oscillation of γ. We notice that the amplitude decay rate increases with V_0 in the initial velocity range 50 $ms^{-1} < V_0 <$ 71 ms^{-1}. Using the A/C/E arrow, the amplitude decay rate increased monotonically from 0.77 s^{-1} to 1.10 s^{-1}. In the case of the X10 arrow, the amplitude decay rate increased from 0.53 s^{-1} to 0.77 s^{-1}.

6.2.8 Comparison between the velocity decay obtained from the acceleration sensor and the numerical simulations at still-air conditions

In the current section the results obtained from the data provided by the acceleration sensor and the numerical simulations under still-air conditions are compared. The chosen shots were the same as in Section 5.5 for A/C/E arrows using straight short and large vanes. From the high-speed video recordings it was possible to obtain the initial conditions for each of the shots. Once the initial conditions were known, it was possible to simulate each of the shots to observe in detail some of the flight characteristics that otherwise would be complicated to grasp due to the rapid arrows' movements. Further, by comparing the obtained results through the experimental procedures and the numerical simulations it was possible to validate the mathematical model used along the current work. The initial velocity (V_0) for each shot was obtained from the high-speed video camera recordings.

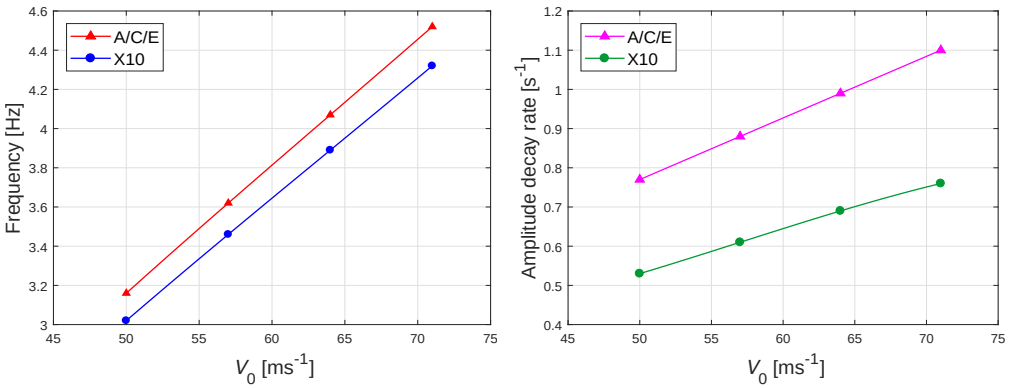

(a) (b)

Figure 6.11: a) Oscillation frequency and b) amplitude decay rate of the angle of attack, γ, as a function of the initial velocity, V_0, under still-air conditions with zero initial angular velocities.

Figure 6.12 shows the time evolution of the velocity for the referred shots in Section 5.5. The data obtained from the acceleration sensor was plotted together with the computed velocity decay for comparison for the A/C/E arrows using the short (Figure 6.12a) and large (Figure 6.12b) straight vanes. Note that good agreement between the data provided by the acceleration sensor and the numerical simulations was found for all the cases.

6.2.9 Time evolution of the pitching angle and the angle of attack during the free flight tests

This section provides the time evolution of the pitching angle and the angle of attack for three selected shots carried out during the free flight tests. The initial angles formed with the z axis (θ_0 and Θ_0) were obtained from the analysis of the high-speed video camera recordings. The selected cases correspond to shots with turbulent and transition boundary layers (Figure 5.13).

For the cases with turbulent and transition boundary layers, no appreciable differences were found in the angle of attack's magnitude. The latter means that the transition phenomena cannot be explained uniquely by the arrow's attitude.

It is of importance to note that the simulation results shown in Figure 6.13 might differ from the actual shots. Despite all the ventilation systems were turned off during the free flight tests, unexpected convective currents may arise due to the influence of the illumination systems located in the different points along the whole trajectory of the arrow. During our experiments, it was possible to note the increase of the temperature in the surroundings of the illumination apparatus,

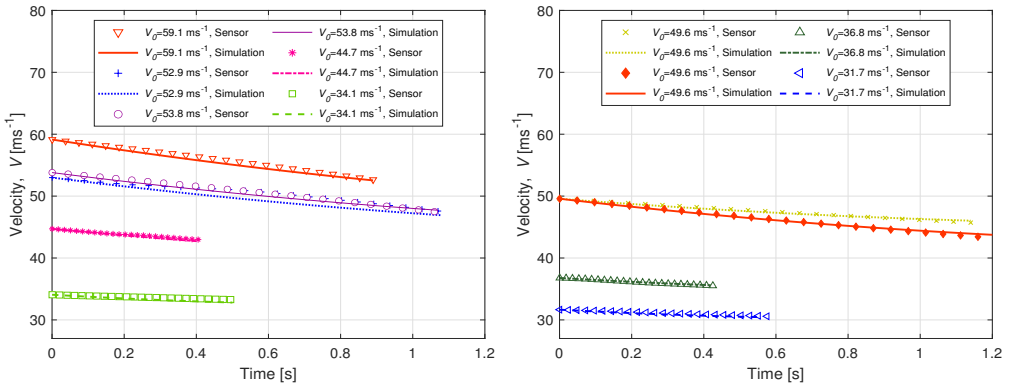

(a) (b)

Figure 6.12: Time evolution of the velocity (V) for shots using short (a) and large (b) vanes.

which may produce weak air disturbances that are difficult to predict. Such subtle wind currents might affect the attitude of the arrows.

6.3 Results corresponding to computations considering the uniform background wind

When the uniform background wind is considered, it is assumed that the wind velocity remains constant during all the trajectory of the arrow regardless of the position and time. The latter means that an observer located at a distance from the target would feel exactly the same wind velocity irrespective of her/his position. At the moment of the shooting stage this might be helpful, because the archer would be able to adjust the bow's position and modify the arrow's trajectory based on the experience of previous shots. Regarding to the direction in which the wind blows, there were set three different uniform wind patterns: side- (u_y), tail- ($u_x > 0$) and head-winds ($u_x < 0$). Here, u_y refers to the case when the wind flows along the y axis, $u_x > 0$ in and $u_x < 0$ against the x direction. The studied wind velocities for the uniform cases were 1 ms^{-1} and 3 ms^{-1}.

6.3.1 Time evolution of the angle of attack under uniform sidewind

In Figure 6.14 the time evolution of the angle of attack, γ, under uniform sidewinds, $u_y > 0$, is shown. The maximum value of the angle of attack, $\gamma_{\max}$, increases

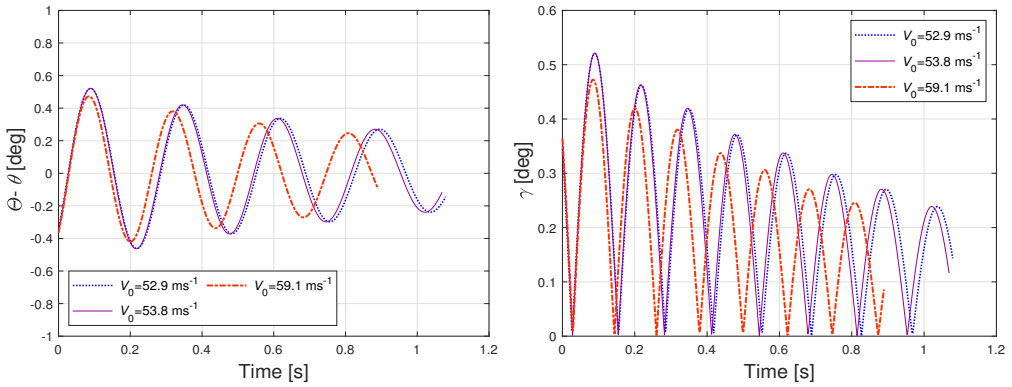

(a) (b)

Figure 6.13: Time evolution of the a) pitch angle ($\Theta - \theta$) and b) angle of attack (γ) for A/C/E using short straight vanes.

with the wind velocity. When u_y=3 ms^{-1}, for both the A/C/E and the X10 arrows with SWV is about $\gamma_{\max} \sim 3.0^\circ$ (–), resulting from the initial misalignment between the arrow and its velocity vector. The oscillatory behaviour of γ is observed due to the pitching moment restoring effect. In Section 6.2.5, the major importance of the pitching moment and the lift force has been shown. The oscillation frequency of the angle of attack is 3.59 Hz and 3.41 Hz for the A/C/E and X10 arrows for a side-wind of u_y = 3 ms^{-1}, respectively. It is smaller for X10 than for A/C/E due to its larger mass and moment of inertia. The damping of oscillation in γ arises from the lift force exerted on the vanes (see Section 6.2.5), which reduces the misalignment between the arrow's axis ($\boldsymbol{n}$) and the velocity direction ($\boldsymbol{t}$).

The amplitude decay rate of γ is 0.87 s^{-1} and 0.60 s^{-1} for the A/C/E and X10 arrows, respectively. Here, the superior moment of inertia also yields the smaller value corresponding to the X10 arrow. The influence of the side-wind velocity on the amplitude decay rate is negligible. Note that the curves are truncated at slightly different time. The end of each curve represents the instant when the arrow strikes the target, located 70 m away from the launching position. Staying in the air longer results in more wind drift. Thus, the arrow shows stronger deviation from the center of the target.

The inserted panels in Figure 6.14 show the time evolution of the angle of attack when the ideal initial angular velocities were set as initial conditions. It is observed that the value of γ is reduced by two-orders of magnitude compared to those results when the initial angular velocities are taken to be zero. The angle of attack is a crucial factor for the boundary layer flow transition. Therefore, it is desirable to keep γ as small as possible, so that the boundary layer remains laminar.

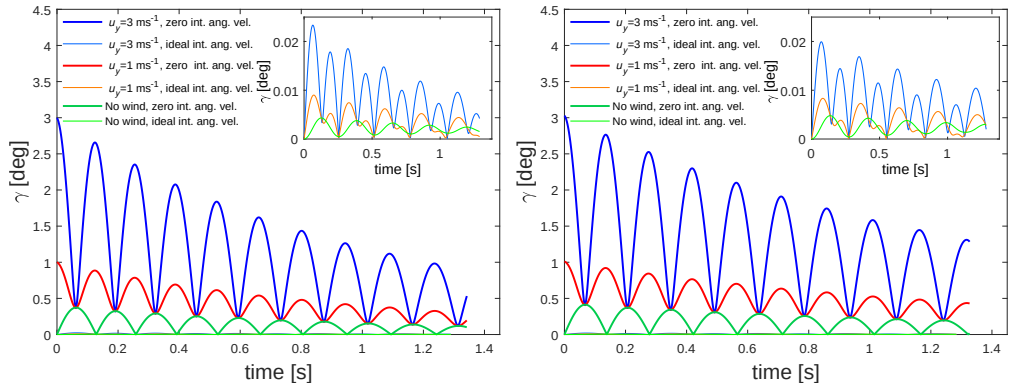

(a) (b)

Figure 6.14: Time evolution of the angle of attack when uniform side-winds were considered and zero initial angular velocities were set as initial conditions for an a) A/C/E arrow and a b) X10 arrow. Inserted panels: close up for the cases when the ideal initial angular velocities were set in the initial conditions.

6.3.2 Arrow trajectories under uniform side-, head- and tail-winds

Figure 6.15 shows the trajectories for both the A/C/E and X10 arrows with SWV under the influence of side-winds with magnitudes u_y=1 ms^{-1} and 3 ms^{-1}. Note that the lateral deviation from the center of the target, δy, increases with the wind's velocity, u_y, as might be expected. This can be understood by a rough estimate given in Equation 6.2, which is based on the fact that the wind drift is mainly induced by the lateral component of the drag F_{D}:

$$\delta y \sim \frac{F_{\mathrm{D}}}{2M}\frac{u_y}{\sqrt{V_0^2+u_y^2}}(L_{\mathrm{range}}/V_0)^2 \sim \frac{C_D\rho\pi r^2}{4M}\frac{u_y}{V_0}L_{\mathrm{range}}^2, \tag{6.2}$$

where L_{range} is the archery range's total length. Equation 6.2 indicates that a larger magnitude of δy can be observed for lighter arrows. To reduce such undesired lateral deviation the archer should use heavier arrows. The deviation δy increases with the ratio of drag force to mass (gravitational force), which is in agreement with the fact reported by Park [30]. For the A/C/E arrow with an initial velocity V_0=57 ms^{-1} the ratio would be 0.45 and 0.80 for laminar and turbulent cases, respectively. For the X10 arrow, the ratio of drag force to mass would be 0.30 and 0.60 for laminar and turbulent cases, respectively.

Consider now the cases in which the ideal initial angular velocities were set in the computations. For such cases, smaller values of δy would be observed than

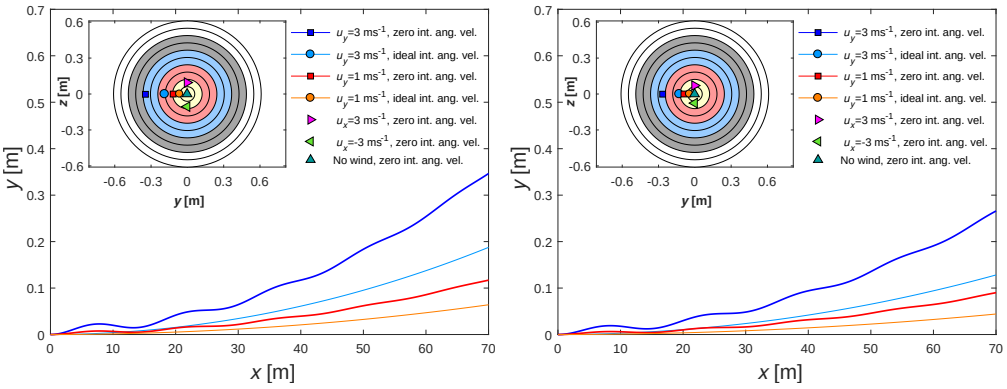

Figure 6.15: Trajectories with uniform side-wind for a) A/C/E and b) X10 arrows with SWV. Ideal initial angular velocity and zero initial angular velocity were considered in the computations. Inserted panels: impact points under uniform side-, tail- and head-winds.

when the initial angular velocities were set to be zero. This behaviour arises from the fact that the arrow's shaft and the wind flow almost align. Thus the boundary layer flow remains laminar and therefore yielding smaller drag. The lateral component of the drag force for the case of laminar boundary layer is smaller than for the case of turbulent boundary layer. The heavier X10 arrow would yield smaller values of the wind drift, δy.

Note that in Figure 6.15 the arrows show an oscillating trajectory. Such oscillatory behaviour arises from the presence of a non-zero angle of attack along the arrows' flights. During the initial 20 m such behaviour can be observed more clearly, induced by the larger γ in the first 0.40 s of the trajectory compared to the remaining flying time (see Figure 6.14). By setting the ideal initial angular velocities, the arrows would almost align themselves with the wind component and angles of attack close to zero might be expected, which reduces the so-called "fish tailing" or "porpoising". In such cases nearly parabolic trajectories could be obtained. It can be observed that the archers might be able to carry out their shots with less deviated trajectories by precisely adjusting the angular velocities to the ideal values. Unfortunately, such a task might be highly challenging to achieve in practice.

In the inserted lateral panels of Figure 6.15 the impact points on the target were estimated, when uniform side-, tail- and head-winds were considered. For the A/C/E arrow, the maximum radial deviation from the center of the target δr=0.34 m occurred when the side-wind was u_y=3 ms^{-1} (■). By setting tail-, $u_x > 0$, and head-winds $u_x < 0$, it yielded radial deviations δr=0.09 m (▶) and δr=0.10 m (◀),

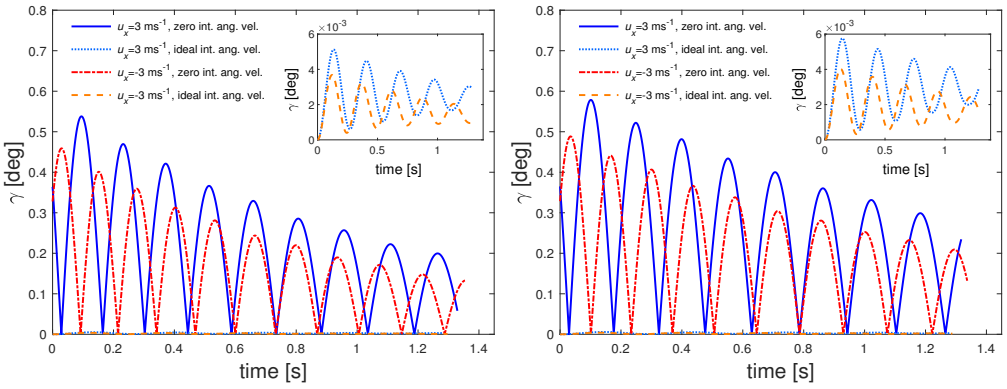

(a) (b)

Figure 6.16: Time evolution of the angle of attack when purely head- ($-u_x$) and tail-winds (u_x) were considered for a) A/C/E and b) X10 arrows with SWV.

respectively, for $|u_x|$=3 ms^{-1}.

In Figure 6.15, we can see that the influence of the side-wind on the trajectory of the arrows brought about more deviated trajectories than the cases when the tail- and head-winds were considered. For the heavier X10 arrow (Figure 6.15b), the maximum radial deviation δr=0.26 m was computed for the case of u_y=3 ms^{-1} (■). These findings show the importance of careful choice of arrows with larger mass.

For the side-winds of u_y=3 ms^{-1}, the difference in the radial deviations between the shots carried out with zero (■) and ideal (●) initial angular velocities were 0.16 m for the A/C/E arrow and 0.14 m for the X10 arrow, respectively. Such differences are not negligible in winning the archery competition.

When the flight of an A/C/E arrow was simulated with zero initial angular velocities and tail- and head-winds were considered ($|u_x|$=3 ms^{-1}), the maximum angle of attack was computed to be $\gamma_{\max} = 0.45^\circ$ and $\gamma_{\max} = 0.54^\circ$ for the head- and tail-winds, respectively. For the X10, $\gamma_{\max} = 0.48^\circ$ and $\gamma_{\max} = 0.58^\circ$ were obtained for the head- and tail-winds, respectively.

These values of γ are located in the boundary layer flow transition zone identified by Miyazaki et al.[22]. In their work, Miyazaki et al. reported that the transition to a turbulent boundary layer may occur if the magnitude of the angle of attack was located in the range $0.40^\circ < \gamma_{\max} < 0.60^\circ$ at Re$= 1.75 \times 10^4$ for an A/C/E arrow fletched with SWV. Due to such small values of the angle of attack, relatively weak lift and drag forces would be exerted over the arrows under the influence of pure head- (◀) and tail-winds (▶), compared to those cases when the arrows are subjected to side-winds, and thus in smaller values of the radial deviation.

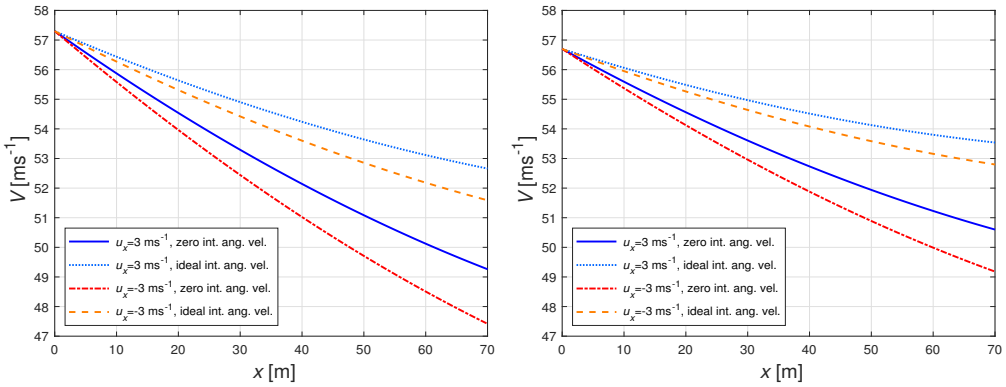

(a) (b)

Figure 6.17: Velocity decay under the influence of uniform head- and tail-winds for a) A/C/E and b) X10 arrows with SWV and an initial velocity $V_0 = 56.6$ ms^{-1}.

6.3.3 Velocity decay under uniform head- and tail-winds

Figure 6.17 shows the velocity decay when the A/C/E (Figure 6.17a) and the X10 (Figure 6.17b) arrows with SWV are subjected to uniquely head- ($u_x < 0$) and tail-winds ($u_x > 0$) in a 70 m archery range. The influence of head-winds enhances the velocity decay for both types of arrows, irrespective of the initial conditions. When the ideal initial angular velocities were set as initial conditions, the angles of attack would remain close to zero and therefore less drag exerted on the flying arrows. In such scenario, the velocity would decay slower. The boundary layer flow would remain laminar and less kinetic energy would be dissipated. In all the studied cases, the X10 arrows were associated with less kinetic energy dissipation compared with the A/C/E for identical initial conditions.

6.3.4 Radial and vertical deviations as functions of uniform side-, head- and tail-winds

The current section provides the computed vertical (Figure 6.18a and Figure 6.18b) and the radial deviations (Figure 6.18c and Figure 6.18d) from the center of the target located at 70 m from the shooting position. We consider the presence of uniform side- head- and tail-winds for both A/C/E and X10 arrows with SWV, and for both the zero and ideal initial angular velocities. The wind velocity was set in the range $0 < U < 3$ ms^{-1}. Note that the vertical deviation from the center of the target is mostly brought about by the head- and tail-winds. The head-winds appears to affect in a more important way than the tail-winds if the wind velocity is identical.

Such behaviour becomes more evident as the wind velocity increases. The vertical deviations would be reduced when the ideal initial conditions were achieved during the shooting stage. The arrows subject to pure side-winds showed negligible deviations in the vertical direction.

Consider now that the innermost ring, the so-called 10 ring, has a diameter of 0.12 m. From Figures 6.18a and 6.18b, it is possible to learn that purely uniform tail- or head-winds with a magnitude larger to $|U| > 1.5$ ms^{-1} would be enough to take out the A/C/E arrow (with the zero initial angular velocity) from the maximum scoring ring. Considering that the flight of an arrow with initial velocity of $V_0 = 57$ ms^{-1} stays in the air around 1.3 s, wind gusts with such characteristics might not be unusual. The arrows' trajectories are highly affected by the background winds. In the case of the X10 arrow shot with zero initial angular velocity a better behaviour compared with the A/C/E arrow is observed. The X10 arrows would stand head- and tail-winds of up to $|U| > 2$ ms^{-1} until leaving completely the area of maximum score.

Figures 6.18c and 6.18d show the computed radial deviations from the center of the target (δr) for identical background wind conditions. It is possible to observe that the side-winds disturb in a more important way the shots. Take the case of the A/C/E (Figure 6.18c) arrow with a wind velocity of $U = 3$ ms^{-1}. When the zero initial angular velocity was considered, the deviation from the center of the target was $\delta r = 0.35$ m under the influence of pure side-winds. Such value is at least three times larger than $\delta r = 0.09$ m when pure tail-winds are present. Regardless of the wind speed, the direction from which it blows seems to be of more importance at quantifying the shot's drift. In all the studied cases, the X10 arrows showed less deviated trajectories (Figure 6.18d).

6.3.5 Maximum lateral displacements as function of the initial velocity under uniform side-winds

In this section, the influence of the initial velocity on the lateral displacement δy is discussed for arrows flying subject to a uniform side-wind of $u_y = 3$ ms^{-1}. In the computations, two initial conditions, i.e. the zero initial angular velocities and the ideal initial angular velocities were set for A/C/E and X10 arrows with SWV.

Figure 6.19 shows the final lateral displacements on the target position located at 70 m from the shooting location and 1.3 m from the floor. In all the considered cases an identical background wind was taken into account. It is possible to observe that δy decreases with V_0. When the A/C/E arrow was shot with an initial velocity of $V_0 = 50$ ms^{-1} and zero initial angular velocities, a lateral deviation of $\delta y = 0.40$ m would take place. On the other hand, for the X10 arrow such deviation would reduce to $\delta y = 0.30$ m.

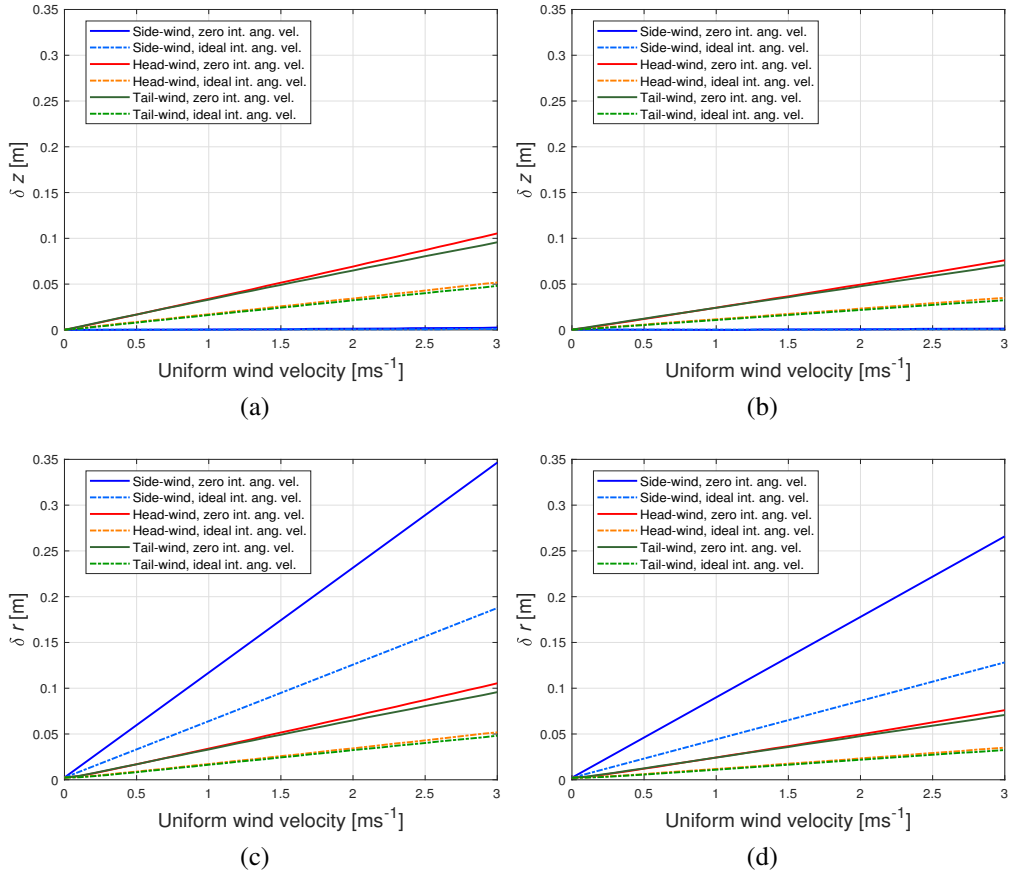

Figure 6.18: Vertical deviations, δz, as function of the wind velocity for a) A/C/E and b) X10. Radial deviations, δr, as function of the wind velocity for c) A/C/E and d) X10 arrows. In all the simulated cases the arrows used SWV.

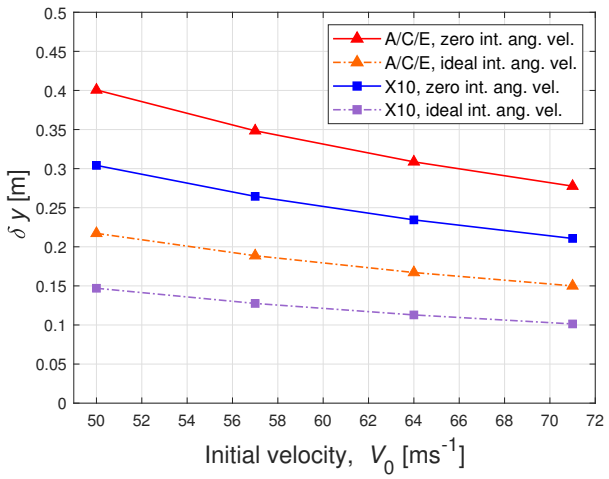

Figure 6.19: Maximum deviation from the center of the target in the y direction, δy, as a function of the initial velocity, V_0, for the A/C/E and X10 arrows with SWV.

If the initial velocity is increased from 50 ms^{-1} to 71 ms^{-1} for the X10 arrow, the final lateral deviation is reduced by around 0.09 m, which is not a negligible distance considering the importance of the precision required in the archery competition. The archers may choose bows and strings that allow them to maximize the initial velocities in their shots.

From Figure 6.19, it is possible to observe that if the ideal initial angular velocities were set as initial conditions, the lateral deviations also would reduce due to the lower values of the angle attack and therefore the drag exerted on the flying arrows. In all the studied cases, the X10 arrows showed less deviated trajectories.

6.3.6 Comparison of the lateral deviation computed numerically with the rough estimation under the influence of uniform side-winds

Figure 6.20 shows the lateral deviation as a function of the initial velocity of the A/C/E and X10 arrows with SWV. In all the cases, the presence of a side-wind of 3 ms^{-1} was considered along the entire trajectory in an archery range of 70 m. The turbulent constant C_D values 2.69 and 3.23 were considered for A/C/E and X10, respectively. The plotted results in solid lines correspond to the numerical solution of the equations of arrow motion, whereas the dotted lines correspond to the rough estimation obtained by Equation 6.2. It is possible to appreciate that the final lateral displacement, δy, at 70 m reduces as the initial velocity of the arrows increases. Arrows with larger kinetic energy are less drifted by background winds.

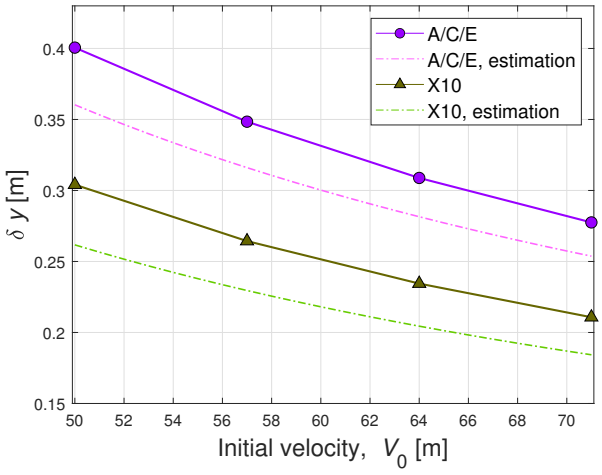

Figure 6.20: Dependence of the lateral deviation in the trajectory on the initial arrow's velocity. Not ideal initial angular velocity and a side-wind of 3 ms^{-1} were considered for A/C/E and X10 arrows with SVW.

Note the importance of the design of archery bows that have high efficiency. The efficiency of a bow is evaluated by the maximum energy transferred from the bow itself to the archery arrow. If larger portion of the potential energy stored in the bow system (limbs and string) is transferred to the arrows, the initial velocity of the projectile increases and therefore the final deviation from the center of the target reduces.

The difference between δy corresponding to the results from the numerical computation and the rough estimations arise from the fact that in Equation 6.2 the velocity is assumed to remain constant along the complete trajectory of the arrow. However, in an actual shot the arrow's velocity decays in its way to the target due the dissipation of energy through the interaction with the surrounding air as seen in Section 6.3.7.

6.3.7 Arrows' velocity decay under the influence of uniform side-wind

Figure 6.21a shows the time evolution of the velocity (V) for shots with different initial velocities (V_0) for the A/C/E and X10 arrows with SWV. In all the shots, a side wind 3 ms^{-1} was considered along the trajectory. The turbulent constant C_D values 2.69 and 3.23 were considered for A/C/E and X10, respectively. In all the studied cases, the smaller mass of the A/C/E arrows caused a faster velocity decay in these types of arrows for shots with identical V_0. The better capacity to retain its kinetic energy by the X10 arrows allows them to have less deviated trajectories

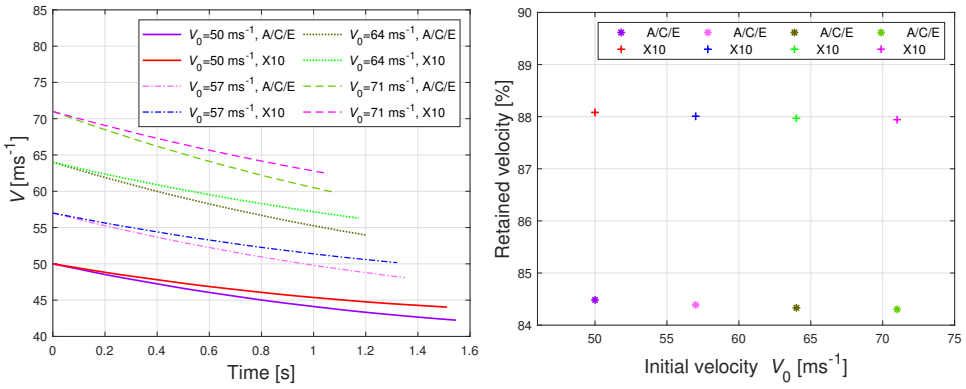

(a) (b)

Figure 6.21: a) Time evolution of the arrow's velocity under the influence of a side wind of 3 ms^{-1} for shots with different initial velocities for the A/C/E and X10 arrows using SWV in a 70 m archery range and b) the percentage of retained velocity at the target position for the same shots and arrows' configurations.

under the influence of background wind, which was appreciated in Section 6.3.2.

Figure 6.21b shows the percentage of retained velocity for the shots with identical characteristics as shown in Figure 6.21a. As previously mentioned, the X10 arrows (with the cross symbols) show a better capacity in storing their kinetic energy than the A/C/E arrows (with asterisk) for all the studied cases. The percentage of retained velocity was found to be between the range of 84.5%-84.3% for the A/C/E arrows. As for the X10 arrows, the percentage of retained velocity was located in the range of 88%-87.9%. The percentage of retained velocity slightly depends on the initial velocity. The arrows with higher initial velocities release their kinetic energy faster than the slower ones as the drag force is proportional to the the square of the arrow's velocity. By comparing the results from the computations under still-air conditions (Section 6.2.6) and considering uniform background wind, it is shown that the wind velocity has little influence in the arrows' velocity decay.

6.4 Results corresponding to computations considering the non-uniform background wind

We devote this subsection to the influence on the trajectory of an A/C/E arrow with SWV subject to a non-uniform background wind described by Equation 6.3. Here, the wind velocity is assumed to have a sinusoidal-type evolution with the position, as shown in Figure 6.22. The wind velocity at any position of the archery

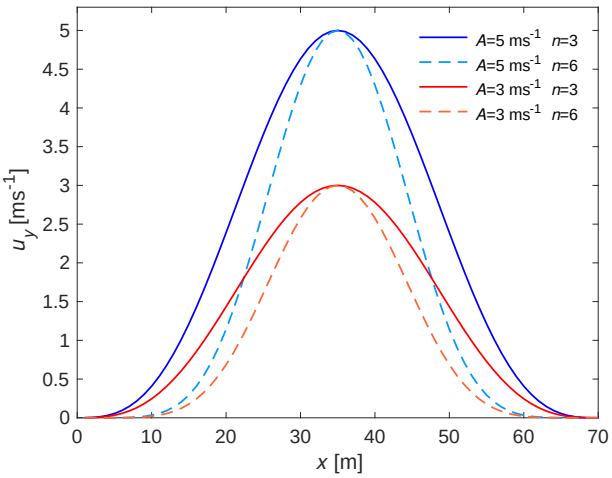

Figure 6.22: Non-uniform side-wind profiles u_y.

range is given by

$$u_y = A\sin^n\left(\frac{\pi x_a}{L}\right). \tag{6.3}$$

Here A is the amplitude (set to 3 ms^{-1} and 5 ms^{-1}), n represents the order of the localization, parameter that we vary for comparison purposes ($n = 3$ and 6). L denotes the length of the archery range (70 m in this particular case) and x_a the instantaneous position of the arrow. Under the non-uniform background wind, the wind's velocity felt by an observer would depend on her/his position with respect to the target. This implies that an athlete performing an outdoors shot may feel the wind with a different strength to that existing along all the trajectory of the projectile. The archer would not have detailed information about the wind behaviour besides to that in her/his position. This uncertainty must be taken in serious consideration by the archers and serves to simulate an archery field located outdoors.

It is important to remark the strong dependency of the wind behaviour on external factors like the local plant canopy [35], possible stadium architecture [11], seasonal wind patterns [20] and time of the day. In a real sports competition performed outdoors, a similar wind pattern to the one introduced in this work would not be unusual as pointed out by Yaghoobian and Mittal [36]. Yaghoobian and Mittal described the changing wind velocities ranging, in average, from 2.90 ms^{-1} to 8.80 ms^{-1} in a golf field with around 90 m between holes. Based on these findings, the non-uniform wind behaviour is considered.

As described before, in the simulations the values of Θ_0, θ_0, Φ_0 and ϕ_0 were adjusted so that under the no wind scenario the arrow hits the center of the target. Nevertheless, once the presence of the background wind is considered, deviations in the y and z directions are expected as the arrow drifts under the wind's influence. Such deviations are defined as δy and δz. Here the lateral deviation from the center of the target, δy, is presented as the time integrated effect of side-wind on the arrow. The radial distance between the impact point and the center of the target is expressed as $\delta r = (\delta y^2 + \delta z^2)^{1/2}$.

Figure 6.23a shows the time evolution of the angle of attack (γ) for different wind patterns ($A = 3,5$ ms^{-1} and $n = 3$ and 6) and zero ideal initial angular velocities. The maximum value of the angle of attack $\gamma_{\max}$ =0.46 $^\circ$ was obtained when A=5 ms^{-1} and $n = 6$. Figure 6.23b shows the time evolution of the angle of attack γ setting the ideal initial angular velocities. Here the maximum angle of attack was $\gamma_{\max}$ =0.41 $^\circ$ for A=5 ms^{-1} and $n = 6$. Notice that the magnitudes of γ are appreciably smaller than those corresponding to a uniform side-wind influence (see Figure 6.14a).

It is possible to appreciate that the values of $\gamma_{\max}$ for the ideal initial angular velocities are smaller than to those shown in the zero initial angular velocities. However, they remain of the same order of magnitude. Such behaviour differs from that shown by the arrows exposed to uniform side-winds, in which γ gets reduced in two orders of magnitude if the ideal initial angular velocities were set. The obtained values of $\gamma_{\max}$ under the non-uniform wind influence are comparable to those when still-air conditions with zero initial angular velocities were considered. One could argue that this small value of γ would correspond to a laminar state in the boundary layer, from the MSBS results shown in Figure 5.5. However, the maximum Re number in the MSBS was 1.0×10^4, which is smaller than the typical value of Re$\sim 2.0 \times 10^4$ for an actual shot. Such uncertainty led us to deal with the behaviour under non-uniform background wind conditions in a more careful way.

It is possible to learn from Figures 6.23a and 6.23b that the maximum angle of attack $\gamma_{\max}$ was located totally (or at least partially) in the transition zone described by Miyazaki et al. [22]. In their work, Miyazaki et al. found that the *threshold* value of the angle of attack, $0.40^\circ < \gamma_{\text{thr}} < 0.60^\circ$, at which the transition from a laminar to a turbulent boundary layer would take place, decreases with the value of Re. At a high Reynolds number of Re$> 2 \times 10^4$, it is possible to assume that $\gamma_{\text{thr}} \sim 0.4^\circ$. Observe that in the case of zero initial angular velocities, very early in the trajectory (flying time$<$ 0.2 s) relatively large values of the angle of attack were computed $\gamma > 0.35^\circ$. We set such values of γ as the threshold values. Once such values exceeded, the boundary layer was thought to become turbulent and therefore larger drag forces were experienced by the arrows.

In the case when the ideal initial angular velocities were set as initial condi-

tions, at the beginning of the trajectory relatively low values of γ were computed. Only after a flying time of around 0.4 s, relatively large values of γ can be found. In such a case, an unexpected transition to a turbulent boundary layer might occur in the middle of the flight. Some other arrows never exceed the value of γ_{thr}, which means that the boundary layer would remain laminar along the complete trajectory ($A = 3$ ms^{-1} and $n = 6$). Such characteristic allowed us to quantify the influence of earlier and retarded laminar-turbulent boundary layer transitions. Note that such γ_{thr} can be modified arbitrarily in the numerical simulations and therefore we are able to alternate between laminar and turbulent values of C_{D}.

Figure 6.23c shows the trajectories followed by the arrows for A=3 ms^{-1} and 5 ms^{-1} with n=6. Both, the zero initial angular velocities (solid lines) and the ideal initial angular velocities (dotted lines) were considered. The lateral arrow deviations were larger for the cases when turbulent boundary layers were assumed than for the laminar cases, due to the larger drag exerted on the arrow.

In the inserted panels in Figure 6.23c (closed circles), the positions where the arrows would hit the target are depicted. The values of the radial deviations from its center, δr, for these cases were smaller in magnitude compared to those obtained when a uniform side-wind influences the flight of the arrows (Figure 6.23a). It comes from the non-uniformity in the background wind velocity, which reduces the total sideward impulse on the arrow. In the case of $A = 5$ ms^{-1}, the radial deviation from the center of the target was $\delta r = 0.18$ m (●), which is smaller than the $\delta r = 0.34$ m in the presence of a uniform side-wind of $u_y = 3$ ms^{-1}.

If the boundary layer remains laminar along the entire trajectory, we would expect small deviations from the center of the target (▲) of around $\delta r = 0.06$ m. Nevertheless, when an unexpected transition from laminar to turbulent boundary layer occurred at ~ 0.6 s, a vertical drop occurs (▲) and therefore an importantly deviated shot. The state of the boundary layer influenced directly the final outcome. Even though the behaviour of the changing wind gusts in the actual outdoor competitions are unpredictable, the current computations give us a first approximation to understand the response of two different archery arrows subject to unexpected background winds.

Even a weak breeze, as such represented by the non-uniform side-wind, may trigger the transition to turbulent boundary layer. If we consider that the archery competition is performed outdoor, it is possible to assume that in occasions the background wind will not be as tender as the one represented in the current computations. We may assume that in most of the shots there will be transition to turbulent boundary layer, showing the importance of understanding the mechanism that triggers such transition.

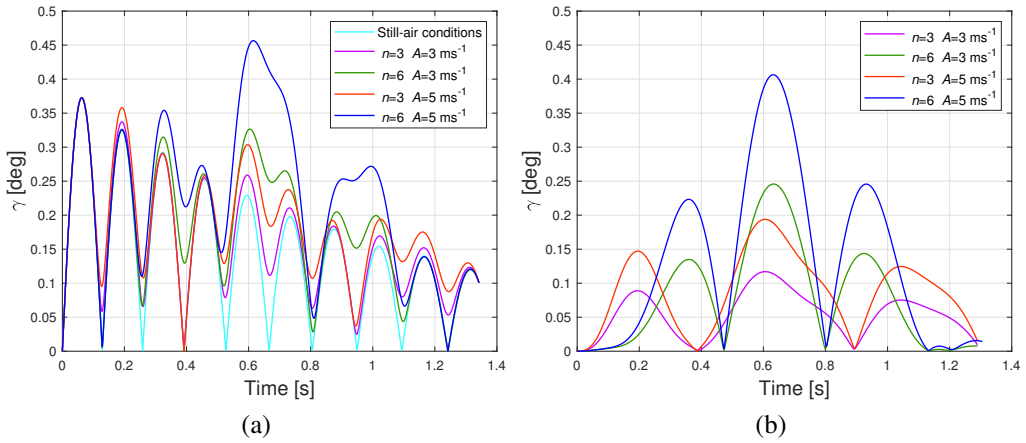

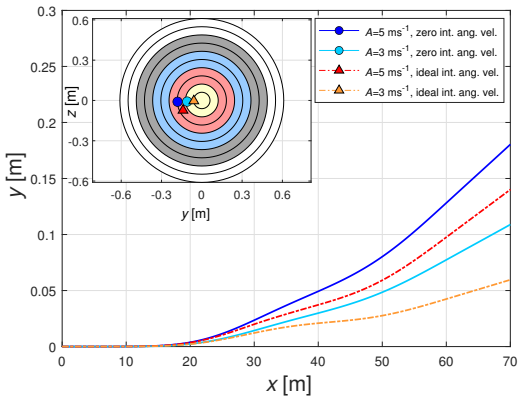

Figure 6.23: Time evolution of the angle of attack of an A/C/E arrow with SWV under non-uniform side-wind using a) the zero initial angular velocities, b) ideal initial angular velocities and c) the computed trajectories and impact points using $A = 3,5$ ms^{-1} and $n = 6$.

Figure 6.24: Yumenoshima Park in the bay of Tokyo, where the archery competitions take place in the Olympic Games in Tokyo 2021. The pictures correspond to the state of October 2018.

6.5 Results corresponding to computations considering the actual background wind occurring in the Olympic archery range

The last type of wind behaviour is considered in this subsection. The three spatial components of the wind velocity vary with time and position, allowing to test the response of the arrows under environments similar to those occurring in real outdoor archery competitions. The data corresponding to the actual wind conditions present in the archery range where Olympic archery competition will take place in the City of Tokyo in the summer of 2021 (the Summer Olympic Games for 2020 were postponed due to the global pandemic of COVID-19).

The outdoor archery range Olympic competitions in Tokyo will take place in the semi-closed bay area. The name of the designated area is Yumenoshima Park. A satellite picture from the location is shown in Figure 6.24. The area is located in the central east part of the Tokyo Metropolitan Area close to the sea. Its total surface is of around 95,000 m^2. Two main competition areas were considered, the first of them is referred as the *final round area* (F.R.A.) in the Fields I, II and III, whereas the second is referred as the *ranking round area* (R.R.A) in the fields IV, V and VI, as shown in Figure 6.25. Each of the six outdoor tracks are north

Figure 6.25: Illustration of the considered archery ranges. The fields I-III correspond to the final round area, whereas the fields IV-VI are the ranking round area.

oriented. The shooting direction was arbitrarily modelled to be South-North and the dimensions of each track are 70 m$\times$5 m. At the end of the track, 70 m away from the shooting position, a target with 1.22 m in diameter is located. The archers aim to strike the innermost circle of such a target to collect the maximum number of points during the competition. Figures 6.24 and 6.25 were obtained from the satellite images in Google Earth Pro (corresponding to the physical conditions present in October 2018).

The data from the wind behaviour in the Yumenoshima Olympic venue was provided by the Japan Agency for Marine-Earth Science and Technology (JAMSTEC). The wind information was obtained by carrying out high resolution numerical computations using a Large Eddy Simulator (LES). JAMSTEC used the Multi-scale Simulator for the Geoenvironment (MSSG) model [30]. By using the MSSG, it is possible to take into consideration the local building shapes present in urban areas in the computations of the atmosphere-ocean circulation model. From the wind information, it was observed that the wind velocity components vary with time and position. In this way, we can estimate the response of commercial arrows under wind conditions that may be faced in an actual archery arrow competition carried out outdoors. The wind information corresponds to a typical clear day of summer in Tokyo bay during August 2007 at noon. The wind information on a horizontal plane located at 2.5 m from the ground was provided with a horizontal

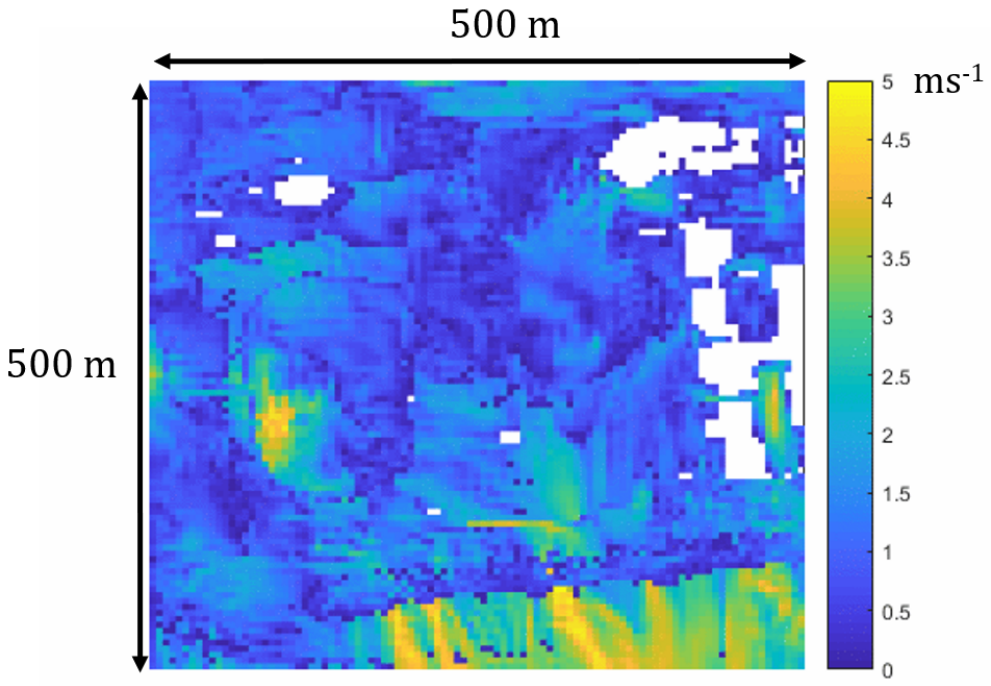

Figure 6.26: Wind velocity information corresponding to the horizontal plane (u_x and u_y).

spatial resolution of 5 m. The three spatial components of the background wind velocity change with time during 30 s with a time step of 0.1 s.

Figure 6.26 shows the wind velocity information at a certain instant on the horizontal plane parallel to the ground. The information corresponds to the horizontal wind magnitude given by $u_{\text{hor}} = \sqrt{u_x^2 + u_y^2}$. The velocity range in the horizontal wind magnitude was $0 < u_{\text{hor}} < 5$ ms^{-1}. The maximum velocity is shown with light yellow, whereas the lower velocity is represented with dark blue. The areas shown with white correspond to the places in which buildings were located, therefore there is no wind information for such spaces. Note that there is a region in the southern part of the studied area with presence of relatively high values of the horizontal wind magnitude of $V_{\text{hor}} \sim 5$ ms^{-1}, strengthened by the presence of buildings. The presence of structures influence importantly the wind patterns observed in the archery range. Such a fact must be taken into consideration when designing the structure of the stadium in which the Olympic competition will take place.

Figure 6.27 shows the vertical component (u_z) of the wind velocity provided by JAMSTEC. For such a case is possible to observe that the range in the vertical

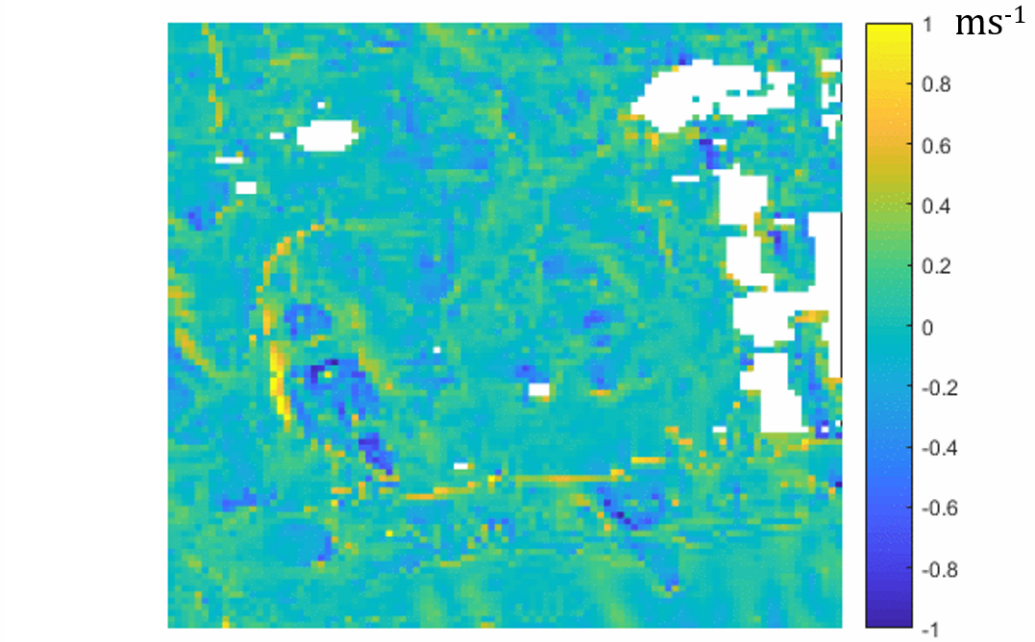

Figure 6.27: Wind velocity information corresponding to the vertical plane (u_z).

velocities was $|u_z| < 1$ ms^{-1}. The positive values of u_z correspond to upward wind currents, whereas the negative values correspond to downward winds. The vertical wind direction changes with the location. From the analysis of the complete wind data, it was possible to observe how the magnitude and direction of the wind changes with time and position during the analysed 30 s, both for the horizontal and vertical wind components.

Figure 1.1 shows that the trajectories of the arrows are semi-parabolic. Nonetheless, the wind information provided by JAMSTEC for the Olympic venue corresponds uniquely to a horizontal plane located at 2.5 m from the ground, as previously stated. Consequently, it was necessary to compute the three components of the wind velocity (u_x, u_y and u_z) at any position in which the arrow was located, as shown in Figure 6.28.

To compute the wind velocity at any location using the JAMSTEC data on a horizontal plane, it was necessary to consider the concept of the surface layer approach. In the surface layer approach, the velocity components of the wind in the vertical direction are given by the logarithmic wind profile which is $u_x = u_{x*}/\kappa \ln(z_a/z_{rl})$ and $u_y = u_{y*}/\kappa \ln(z_a/z_{rl})$, where κ is the universal von Karman constant with a value of 0.4. The value of z_a is the position of the arrow's center of mass in the z direction with respect to the ground and z_{rl} corresponds to the roughness length, for which a typical value for a surface covered with grass is

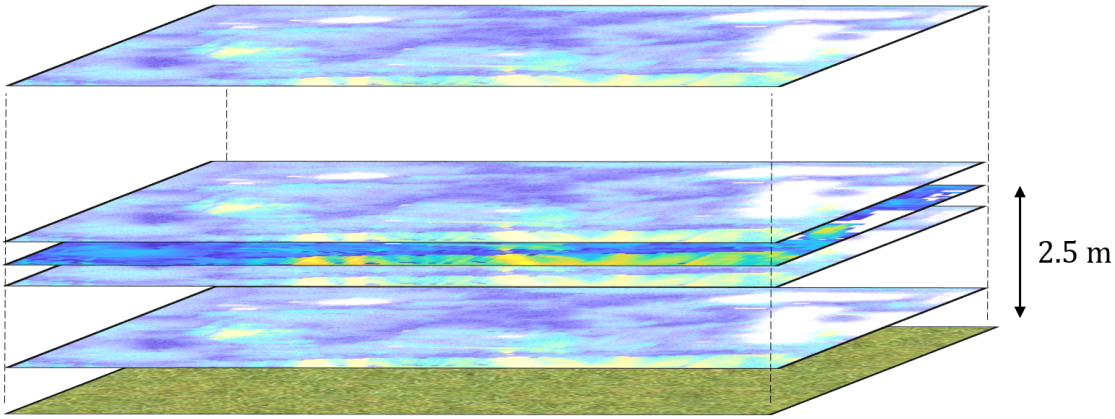

Figure 6.28: The data provided by JAMSTEC correspond to a horizontal plane located at 2.5 from the ground level.

$z_{\mathrm{rl}} = 0.01$ m. The variables u_{x*} and u_{y*} correspond the the friction velocities, which can be computed with

$$u_{x(2.5)} = \frac{u_{x*}}{\kappa} \ln\left(\frac{2.5}{z_{\mathrm{rl}}}\right), \tag{6.4}$$

$$u_{y(2.5)} = \frac{u_{y*}}{\kappa} \ln\left(\frac{2.5}{z_{\mathrm{rl}}}\right). \tag{6.5}$$

By solving Equations 6.4 and 6.5 for u_{x*} and u_{y*} at every iteration, the values of the friction velocities were obtained. Here $u_{x(2.5)}$ and $u_{y(2.5)}$ are the x and y components, of the wind at 2.5 m from the ground level. The x and y components of the wind velocity at any instant and location can be obtained with

$$u_x = \frac{u_{x(2.5)} \ln\left(\frac{z_{\mathrm{a}}}{z_{\mathrm{rl}}}\right)}{\ln\left(\frac{2.5}{z_{\mathrm{rl}}}\right)}, \tag{6.6}$$

$$u_y = \frac{u_{y(2.5)} \ln\left(\frac{z_{\mathrm{a}}}{z_{\mathrm{rl}}}\right)}{\ln\left(\frac{2.5}{z_{\mathrm{rl}}}\right)}. \tag{6.7}$$

In Equations 6.6 and 6.7 the values of z_a are numerically computed from the equations of arrow motion, as described in Section 4.2. As for the case of the vertical component of the wind velocity, it can be obtained by the process explained below. When the continuity condition is considered,

$$\frac{\partial u_x}{\partial x} + \frac{\partial u_y}{\partial y} + \frac{\partial u_z}{\partial z} = 0, \tag{6.8}$$

and taking into account Equations 6.6 and 6.7, it is possible to realize that the x and y wind components are roughly proportional to $\ln\left(\frac{z}{z_{rl}}\right)$ or $\frac{\partial u_x}{\partial x} + \frac{\partial u_y}{\partial y} \propto \ln\left(\frac{z}{z_{rl}}\right)$ and therefore Equation 6.8 can be used to compute u_z with

$$\begin{aligned} u_z &\propto \int_{z_{rl}}^{z} \ln\left(\frac{z}{z_{rl}}\right) dz, \\ &\propto z\ln\left(\frac{z}{z_{rl}}\right) - (z - z_{rl}). \end{aligned} \tag{6.9}$$

Since the vertical component of the wind at 2.5 m from the floor $[u_{z(2.5)}]$ is known from the data provided by JAMSTEC, it is possible to obtain the vertical component of the wind at any location with

$$u_z = u_{z(2.5)} \frac{z\ln\left(\frac{z}{z_{rl}}\right) - (z - z_{rl})}{2.5\ln(250) - 2.5 + 0.01}, \tag{6.10}$$

or

$$u_z = 0.0884\, u_{z(2.5)} \left[z \ln\left(\frac{z}{z_{rl}}\right) - z + z_{rl} \right]. \tag{6.11}$$

By computing Equations 6.6, 6.7 and 6.11 the three spatial components of the background wind can be obtained along the complete trajectory of the arrow. Nevertheless, it was confirmed that the change in the arrow's center of mass location is computed in orders of millimetres $[O(10^{-3})]$, whereas the spatial resolution of the wind information is 5 m. Therefore it is necessary to obtain the wind components for such resolution by spatially interpolating the correspondent wind values. Further, the time step for the wind information provided by JAMSTEC is of 0.1 s, whereas the time step in the Runge-Kutta computations is 5×10^{-4} s. Thus, it is also necessary to perform a time interpolation of the wind components at each

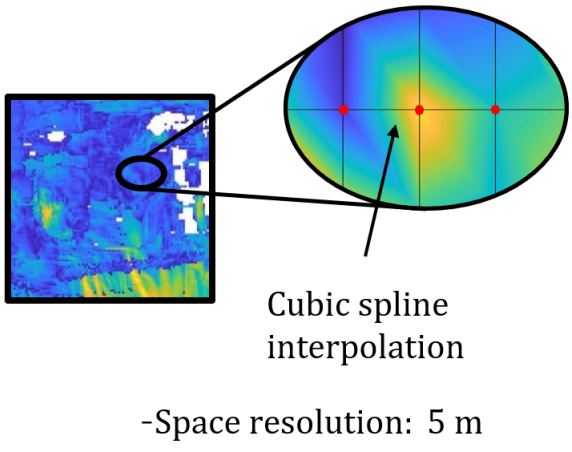

Figure 6.29: Local space interpolation of the wind information using a spline interpolation scheme.

time step of the numerical computation. For both the spatial and time interpolations, a numerical cubic spline interpolation scheme was carried out in every step as shown in Figures 6.29 and 6.30.

Figures 6.31, 6.32 and 6.33 show the time evolution of each of the three wind components (u_x, u_y and u_z) in three different positions of the six projected archery fields. The three selected positions were the shooting location (x =0 m), the middle (x =35 m) and at the end of the archery range (x =70 m). All the plotted data correspond to a horizontal plane located at z=1.5 m from the ground. Such distance was selected because it is approximately the vertical location at which the shoots are carried out by the archers. The time evolution of each of the wind components is given for the available wind data during 30 s. Thus, such wind velocities are likely to be experienced by the archers, but not by the arrows themselves (since the arrows posses a semi-parabolic trajectory as Figure 1.1 shows). Note that such velocities may vary in the vertical direction (or different horizontal planes), which becomes important if we recall that the maximum vertical distance reached by the arrows shot in a 70 m archery range would be $z_{\max} \sim 3.5$ m.

Let us focus on u_x in the field I (Figure 6.31a) at an arbitrarily chosen time of 10 s. In such a case the positive values of u_x correspond to tail-winds, whereas the negative values of u_x correspond to the head-winds. At the specified time we should note that the wind velocity in the three locations has a different magnitude, i.e. u_x =0.6 ms^{-1}, u_x =1.4 ms^{-1} and u_x =3.2 ms^{-1} at $x = 0$ m, $x = 35$ m and $x = 70$ m, respectively. This means that the archer would experience a wind velocity that is actually weaker than the wind velocity blowing at the middle and at the end of the archery range. Such characteristic differs from the uniform background

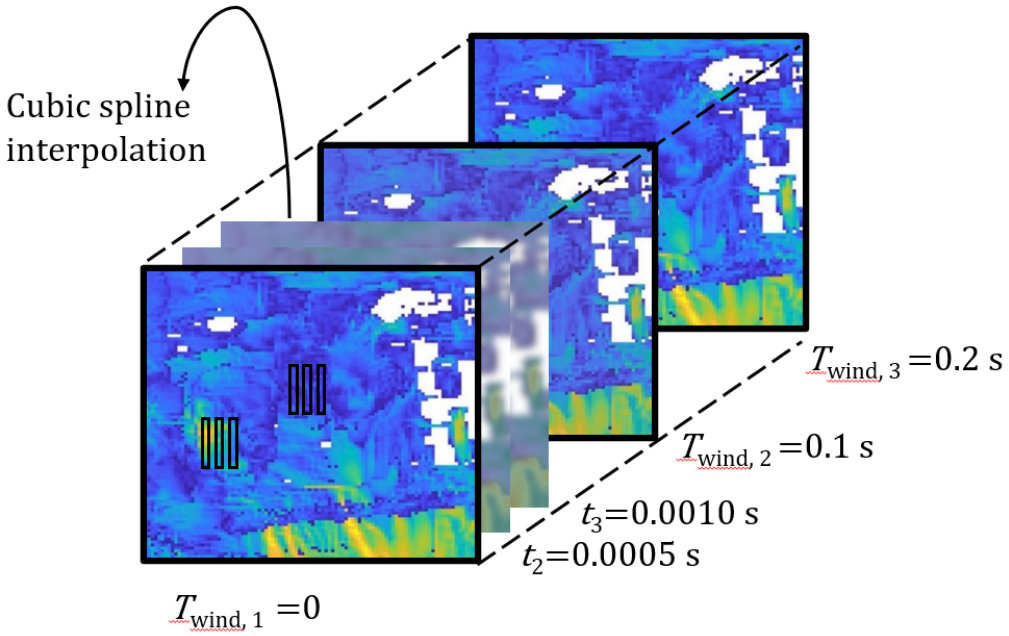

Figure 6.30: Time interpolation of the wind information using a spline interpolation scheme.

wind scenario, in which the arrow would experience the same wind velocity along all its flight, regardless the position and instant. In the case of the u_y component at the shooting position ($x = 0$ m), the wind velocity reduces from around 2 ms^{-1} to 1 ms^{-1} during the 30 s of available data. In such a case the archer would better wait so that it exists a weaker side-wind and therefore less disturbance in the initial stage of the shot. Nevertheless, the wind direction and velocity is unknown by the archer. There is no way in which the archer could know in advance what the wind would be like at any instant and position. The latter characteristic might be common in actual outdoor archery ranges. Such behaviour appears to describe better the actual wind than the uniform and non-uniform background winds previously considered.

The u_z component (Figure 6.31e) remains relatively low ($|u_z| < 1$ ms^{-1}) during the studied 30 s. Such behaviour can be observed in all the six archery fields. Let us look at the wind information for field III. As for the horizontal velocity u_y, it is possible to observe that at the middle of the archery field (35 m) it oscillates between positive and negative values ($|u_y| < 1$ ms^{-1}), which is interpreted as a rapid change in the wind direction. Observe that the u_y wind component behaviour is different at the shooting and target positions. In the former, an almost uniform

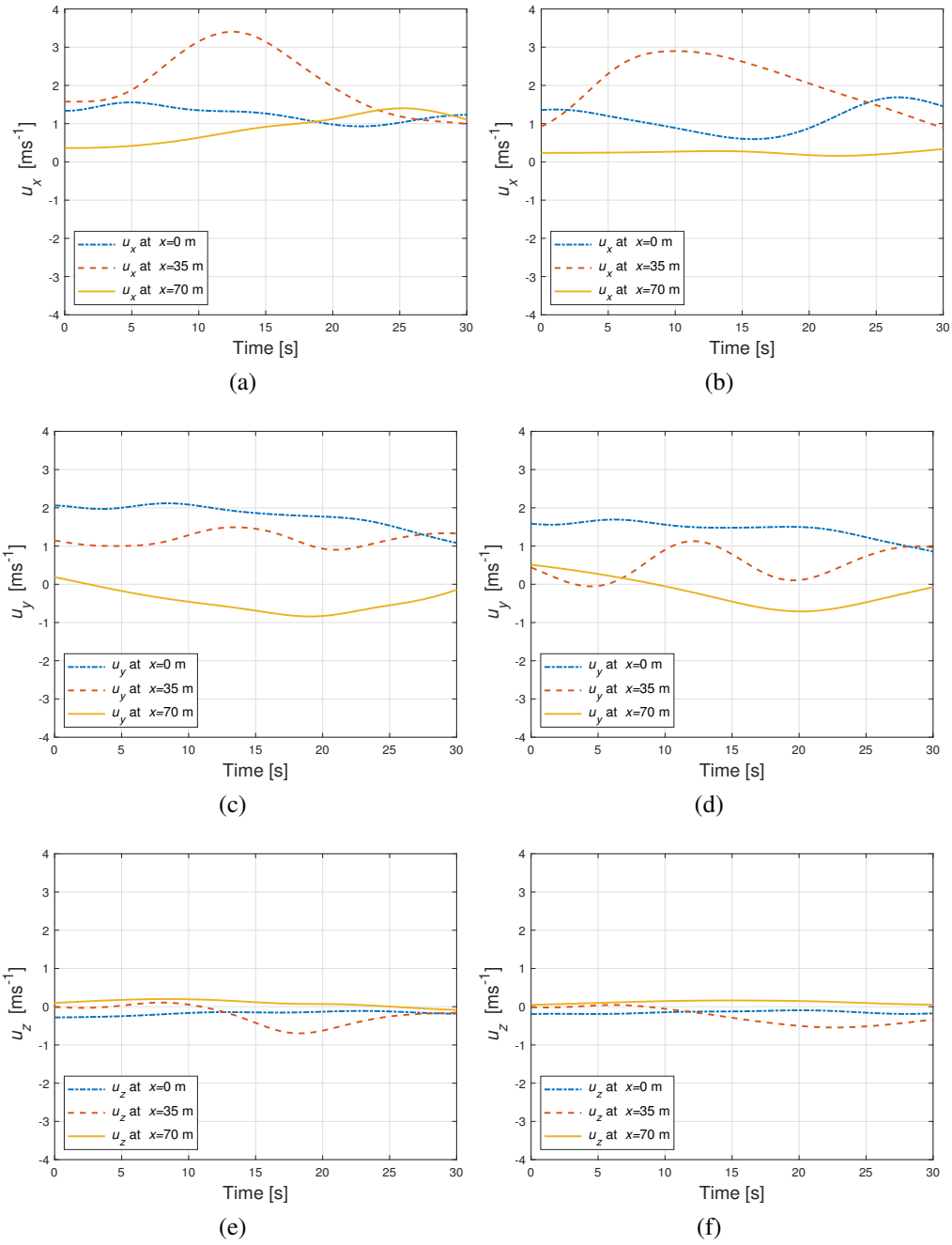

Figure 6.31: Wind information components at three different positions of the archery range for field I (a, c and e) and the field II (b, d and f) at z =1.5 m from the ground.

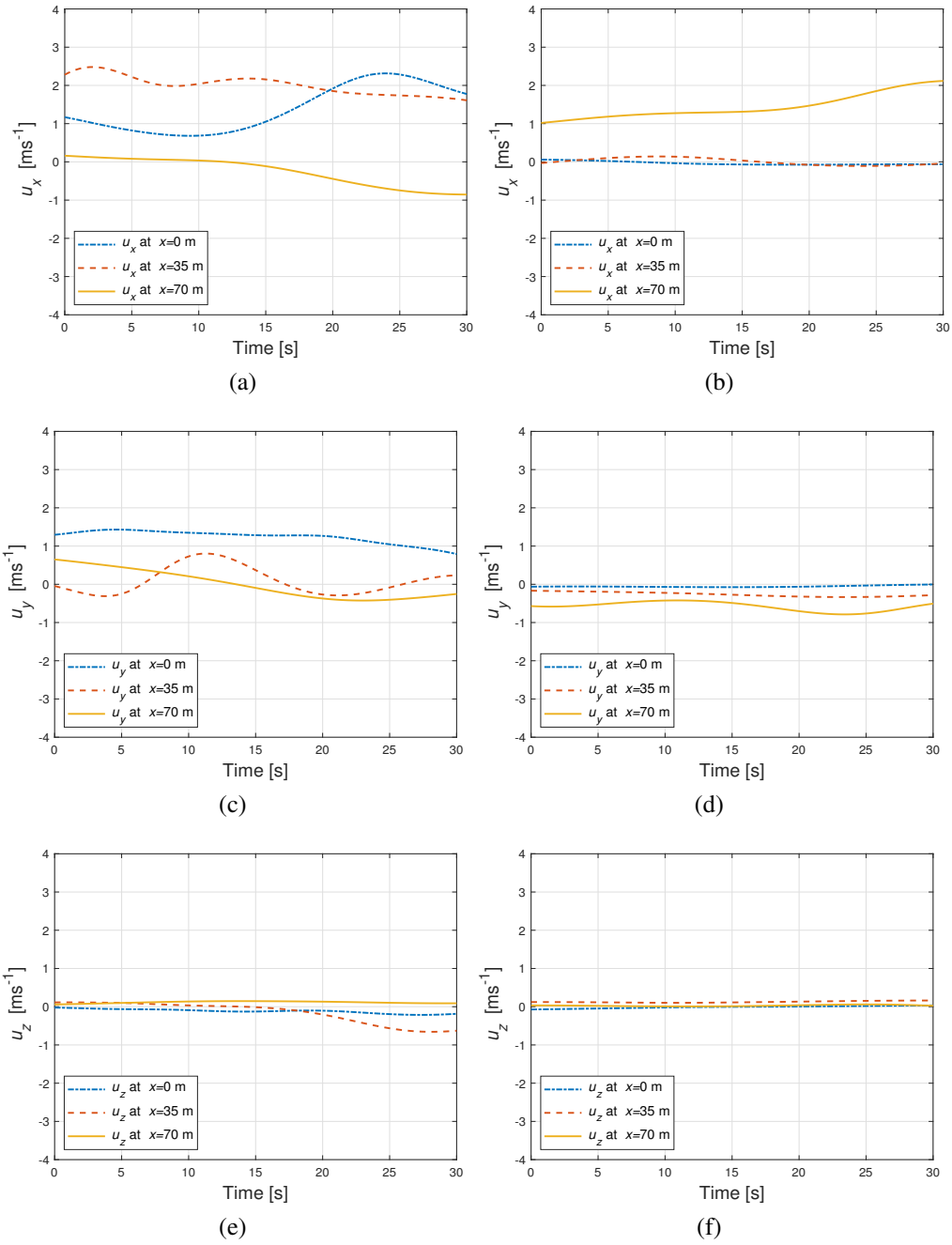

Figure 6.32: Wind information components at three different positions of the archery range for field III (a, c and e) and the field IV (b, d and f) at z =1.5 m from the ground.

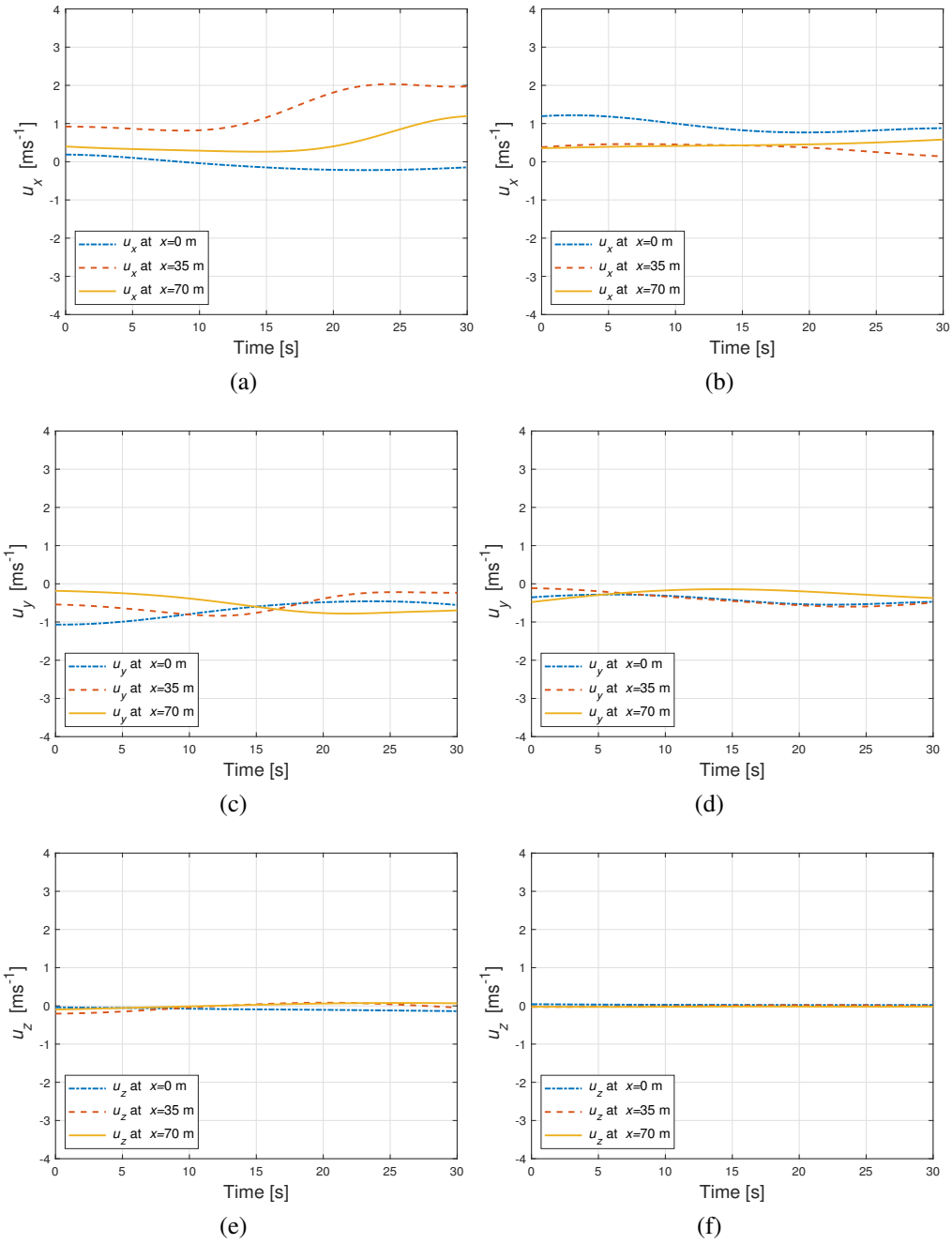

Figure 6.33: Wind information components at three different positions of the archery range for field V (a, c and e) and the field VI (b, d and f) at z =1.5 m from the ground.

wind of $u_y \sim 1.4$ ms^{-1} blows during first 20 s of the total time. In the remaining time, its velocity decays monotonically to 0.95 ms^{-1}. At the target position, the wind velocity decays monotonically from 0.65 ms^{-1}. At around 13 s, its direction is inverted. Then it is possible to appreciate that in actual outdoor archery ranges, the wind information sensed by the archer might be different to the actual wind characteristics at the middle and the end of the archery range. Such unexpected wind characteristics might disturb importantly the shots.

Figures 6.34, 6.35 and 6.36 illustrate the location dependences of the three components of the wind during the 30 s of the wind information provided by JAMSTEC along the complete 70 m of the archery range and on a horizontal plane located at 2.5 m from the ground. The wind velocity ranges from -1 ms^{-1} to 3.5 ms^{-1}. It is possible to observe the temporal and spatial non-uniformity of the wind velocity along the archery range, as expected from an archery field located outdoors. The latter is of importance because it reflects that the flying arrows will experience certain wind characteristics along their flights depending on the moment at which the archers perform the shots. Consider the u_x wind component in field I. Observe that around the middle area of the archery range, at around 30 m from the shooting position, relatively large values of the tail-winds ($u_x > 3$ ms^{-1}) are present for around 10 s. After such time span, the velocity value decays rapidly in the middle area. The latter behaviour arises partially as a result of flow disturbances occurring due to the air-ground interaction.

The presence of trees and other buildings in the area intensify non-uniformities in the wind behaviour. Further, the fact that the Olympic archery venue is close to the sea might represent an important factor to be considered. The testimony of the archers regarding to the wind behaviour during the Summer Olympic Games in Rio de Janeiro in 2016, would be useful to acknowledge from a first-hand witness how the arrows responded in outdoors archery ranges close to the ocean. During the 2016 Olympic archery competition, the archery venue, El Sambodromo, was located 3 km away from the sea. Differently, during the Olympic Games in London 2012, the archery range, Lord's Cricket Ground, was located around 50 km from the sea. By comparing the experience of the archers in those two archery venues would be possible to grasp the arrows' response under the influence of the sea-breeze in a better way. In the case of the Olympic archery venue in Tokyo, which is in the coastal area, the wind conditions might be similar to those occurring in the Brazilian venue, due to the proximity with the ocean. Figures 6.34a, 6.34b, 6.35a, 6.35b, 6.36a, 6.36b indicate the predominance of wind gusts blowing in the South-North direction ($u_x > 0$) due to the presence of the ocean mostly at the southern part of the archery venue.

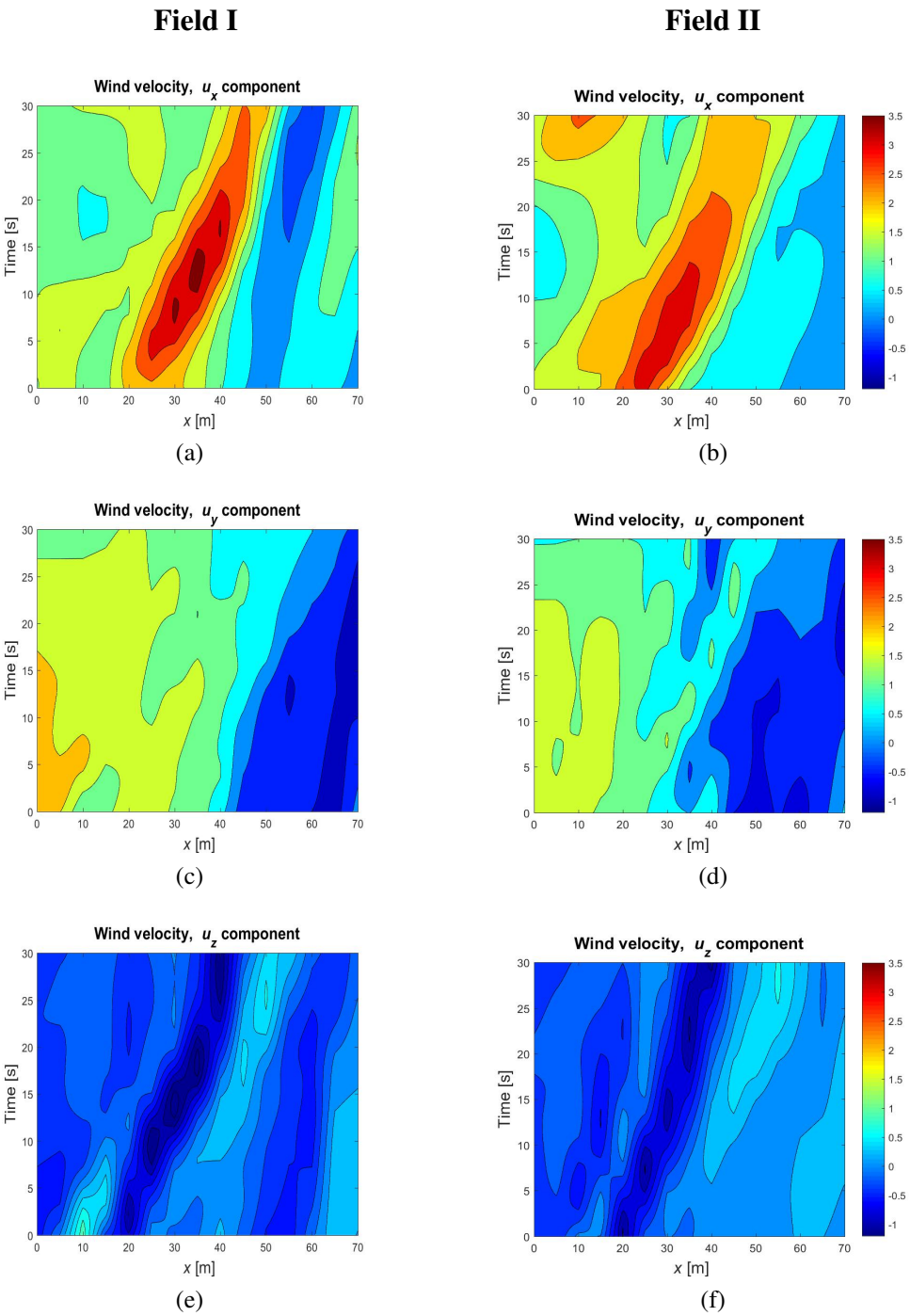

Figure 6.34: Wind velocity time evolution according to the position for field I (a, c and e) and field II (b, d and f) at z =2.5 m.

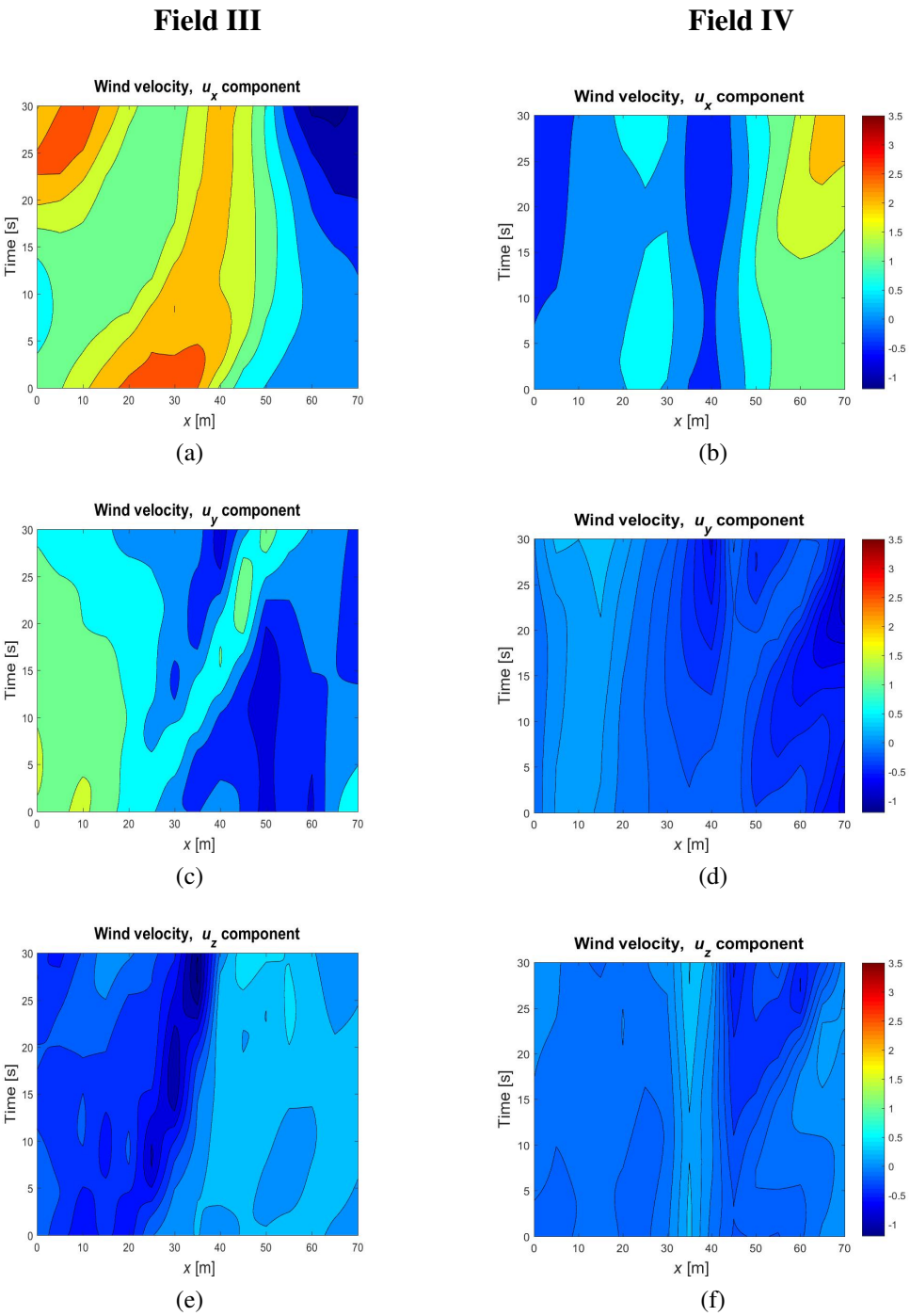

Figure 6.35: Wind velocity time evolution according to the position for field III (a, c and e) and field IV (b, d and f) at z =2.5 m.

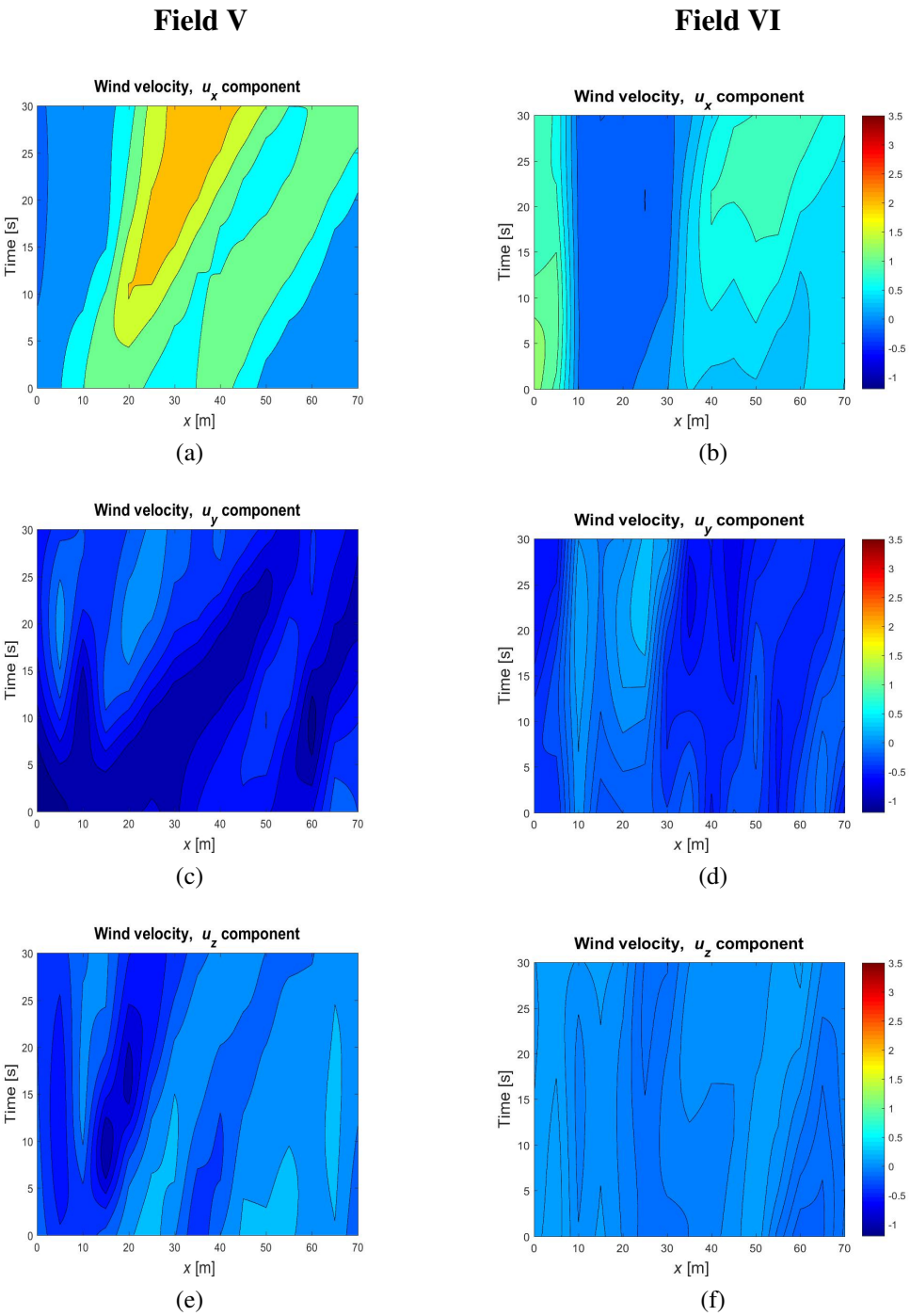

Figure 6.36: Wind velocity time evolution according to the position for field V (a, c and e) and field VI (b, d and f) at z =2.5 m.

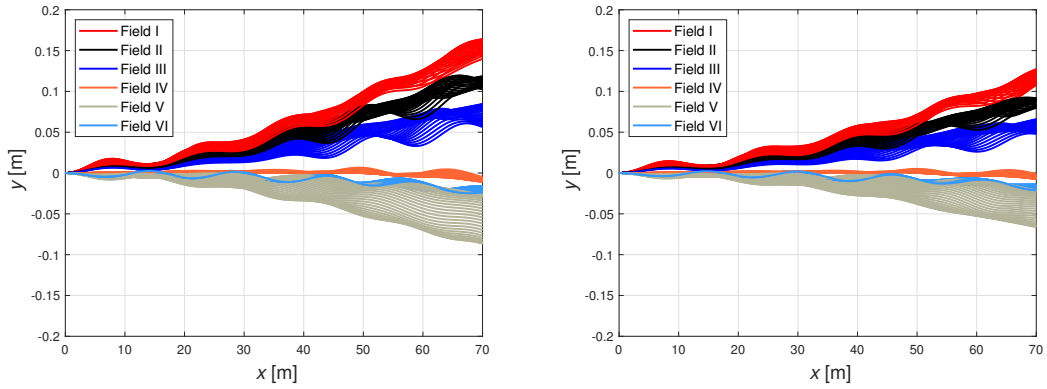

Figure 6.37: Computed trajectories in the six considered fields using different shooting moments for the a) A/C/E and b) X10 arrows.

6.5.1 Trajectories in the Olympic archery range

Figure 6.37 shows the upper view of multiple computed trajectories for the A/C/E and X10 arrows with zero initial angular velocities. With the different colors the trajectories corresponding to the six different selected archery ranges are shown. Multiple starting times were considered for each range to make sure that the arrows would experience different wind fields during their flights in the same archery range. The delay between shots was arbitrarily chosen to be 1 s. Regardless of the selected archery range, the X10 arrows with larger mass showed less lateral wind drift (δy) (Figure 6.37a) than the lighter A/C/E (Figure 6.37b).

In the Final Round Area (F.R.A.), mainly east-west ($u_y > 0$) side-winds were experienced by the arrows, resulting in a positive wind drift. Whereas for the Ranking Round Area (R.R.A.), negative values of wind drift were obtained due to the dominance of west-east wind currents ($u_y < 0$). The averaged values of δy were computed to be 0.15 m, 0.11 m and 0.07 m for the fields I, II and III, respectively, for the A/C/E arrows. Note that the trajectories varied more importantly in the field V than in the field VI, regardless their proximity, for both the lighter A/C/E and the heavier X10 arrows.

There were selected two shots from the computed trajectories for the A/C/E arrow. They are represented with solid and dashed lines in Figure 6.38. The selected shots correspond to those with the largest and smallest lateral deviation in the F.R.A. A difference of around 0.12 m between these shots is not negligible in the archery competition. Therefore, it is of interest to elucidate the mechanism by which the arrows are displaced in such a different way. In Figure 6.39 we plot the background wind components experienced by the arrows in both shots.

As the arrows translate in the archery range, the wind velocity changes with the position. For the case yielding a maximum δy in the field I (Figure 6.39a), the maximum side-wind's velocity was u_y =2.07 ms^{-1}. Such a wind velocity was experienced by the arrow for just a fraction of a second, in contrast to the cases of uniform side-wind, in which the arrow experienced a uniform wind velocity along all its trajectory. After reaching the maximum u_y, the velocity if the side-wind experienced by the arrow decays monotonically along the rest of the trajectory and changing the direction to $-u_y$ in the last 15 m of the trajectory. Relatively low tail winds ($u_x \sim$1 ms^{-1}) were experienced by the arrow in the first 20 m of the trajectory and at around 40 m from the shooting position, a maximum tail-wind of u_x =3.71 ms^{-1} occurred. Nevertheless, from the uniform background wind computations it was observed that the tail-winds are less disturbing for the shots than the side-winds. Due to the major contribution to the total drift by the side-winds, a rough estimation of the drift could be obtained by integrating side-wind component with

$$\delta y = \int_0^{t_{\text{end}}} u_y \mathrm{d}t. \tag{6.12}$$

Regarding to the case in which the minimum δy was experienced in the field III (Figure 6.39b). In such a case the arrow was subject to a relatively weak side-wind of $u_y \sim$1 ms^{-1} along the entire trajectory. The maximum side-wind experienced by the arrow was u_y =1.23 ms^{-1} at around 50 m from the shooting position. This is smaller than the previous case, yielding the smaller lateral deviation. As in the previous case, the wind's velocity and direction changes along the trajectory. Such wind behaviour might be commonly experienced by arrows during the outdoors archery competitions.

6.5.2 Shots with maximum and minimum radial deviation in the Olympic archery range

In the current section, several scenarios for shots with different characteristics are studied. The analysed cases correspond to simulations of shots carried out in the fields II, IV and V. These cases were selected because the flight characteristics are of interest. An A/C/E arrow with SWV and ideal initial angular velocities as initial conditions was considered. Therefore a laminar boundary layer was assumed initially. In these computations we recall the concept of the threshold angle of attack, γ_{thr}. In the three mentioned cases, its value was set to be $\gamma_{\text{thr}} \sim 0.4^\circ$. Therefore it was assumed that the transition from laminar to turbulent boundary layer took place if the angle of attack exceeded γ_{thr}. As in Section 6.5.1, several

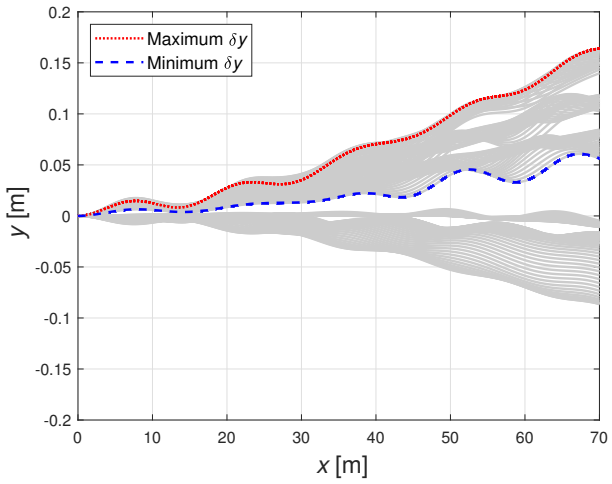

Figure 6.38: Maximum and minimum lateral wind drift (δy) in the final round area for the A/C/E arrows.

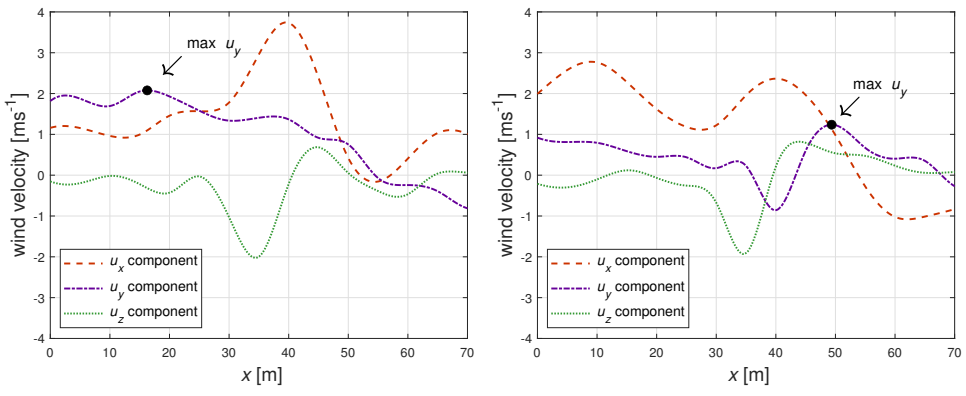

(a) (b)

Figure 6.39: Wind velocities experienced by the A/C/E arrows for two selected shots with a) maximum and b) minimum values of δy.

shots were simulated with different shooting times for which the interval was 1 s. From such set of shots, there were selected those with larger radial deviation from the center of the target δr.

Figures 6.40, 6.41 and 6.42 illustrate the time evolution of the angles of attack for the selected shots with maximum and minimum δr obtained in the fields II, IV and V. In the inserted panels are shown the positions were the arrows would impact for such shots. Further, the wind velocity components experienced by the arrows with maximum and minimum δr are plotted. Let us consider the simulations corresponding to the field II (shown in Figure 6.40). This is the shot with a maximum δr, in which the transition to turbulent boundary layer (●) occurred at around ~ 0.1 s (early transition), leading to a final radial deviation from the center of the target of $\delta r = 0.31$ m (■). This result is compared with the case with minimum δr, for which the transition to a turbulent boundary layer took place at around 0.4 s. In such a case the radial deviation from the center of the target was $\delta r = 0.14$ m. A delay of around 0.15 s was enough to greatly improve the final outcome. The difference between both shots is not negligible and might be crucial during the competition.

Figures 6.40a and 6.40b show the time dependant magnitudes of the head-, tail- and side-winds experienced in the shots with maximum and minimum δr, respectively. Closed dots (●) indicate the moments in which the maximum values of the side-wind are experienced by the arrows. The maximum values of the side-wind experienced were u_y =1.93 ms^{-1} and u_y =1.24 ms^{-1}, for the shots with maximum and minimum δr, respectively.

For both scenarios, the vertical wind's component has relatively low values ($|u_z| \sim 0$) with the exception for an instant located at around 0.4 s and 0.7 s, in which it reaches its maximum. The negative direction (downward) at such maximum values might be partially responsible for the vertical drop in both shots. For both shots, the wind changed rapidly its direction during the entire arrows' flights.

Figure 6.41 shows the shots carried out in the field IV. Note the relatively low values ($\gamma < 0.5\,^\circ$) of the angle of attack that were developed in the first half for both cases. The laminar-turbulent boundary layer transition (●) occurred at around 0.65 s for both shots. Such late transition led to a small radial deviation which allowed the archer to hit the innermost ring ($\delta r < 0.06$ m). Note the low values of side- and vertical-winds experienced by the arrows during the entire trajectory ($|u| < 1$ ms^{-1}). Such low values of the background wind velocity yielded less disturbed shots.

Figure 6.42 shows the computations for shots simulated in the field V. Here for the shot with the maximum δr, the laminar-turbulent transition (●) occurred very early in the flight, leading to an important drop in the vertical direction and a radial deviation from the center of the target $\delta r = 0.41$ m. In such a case, most of

the trajectory the arrow's boundary layer presented a turbulent behaviour due to the large values of the angle of attack, for which the archer might not be prepared. The unexpected boundary layer transition yielded in large drag force exerted on the arrow during most of its flight. The rapid change of the wind components in the first 0.2 s might be partially responsible for the important perturbations in the boundary layer, which may trigger the transition. Contrary, in the case when the transition took place at around 0.48 s, the final deviation from the center of the target was $\delta r = 0.11$ m. By retarding the laminar-turbulent transition around 0.45 s, the archer was able to obtain more points by reducing the drop of the arrow.

6.5.3 Influence of the threshold value of the angle of attack on the arrows' dynamics in the Olympic archery range

In the current section the influence of the threshold value on the final trajectory of the arrows is studied. Figure 6.43 shows the time evolution of the angle of attack and the impact points for the studied cases. The shots in the field II were simulated for the A/C/E arrow with SWV. One corresponds to a shot with zero initial angular velocities (▲) and the other two to shots with the ideal initial angular velocities (■ and ●). For the latter two types of shots, different threshold values of the angle of attack were considered, $\gamma_{\text{thr}} = 0.4^\circ$ and $\gamma_{\text{thr}} = 0.6^\circ$. Identical background wind conditions were taken into account for these three shots.

The shot with zero initial angular velocities has a relatively high initial angle of attack of $\gamma > 1.6^\circ$. For such a shot, a fully turbulent boundary layer was developed, since no control of the initial angular velocities, and therefore of the arrow's attitude, was carried on. In such a case the archers may assume that a fully turbulent boundary layer should be developed during the entire arrow's flight. The final deviation from the center of the target was $\delta r = 0.12$ m (▲). In such a case, the deviations in the trajectory arose from the side-wind influence and the drag exerted on the arrow. No unexpected transitions of the boundary layer took place under this scenario.

Consider now the cases on which the ideal initial angular velocities were set and two threshold values of the angle of attack were taken into account in the numerical computations. Note that for both shots, smaller initial angles of attack were developed in the beginning the arrows' flights compared to the case in which zero initial angular velocities were considered. The laminar-turbulent transitions took place at $\sim$0.12 s and $\sim$0.27 s for the cases with $\gamma_{\text{thr}} = 0.4^\circ$ and $\gamma_{\text{thr}} = 0.6^\circ$, respectively. The final radial deviations from the center of the target were $\delta r = 0.29$ m (■) and $\delta r = 0.20$ m (●). In both cases the boundary layer remained turbulent along most of the trajectory, a delay of $\sim$0.15 s in the transition time reduced the radial deviation from the center of the target by $\sim$0.09 m.

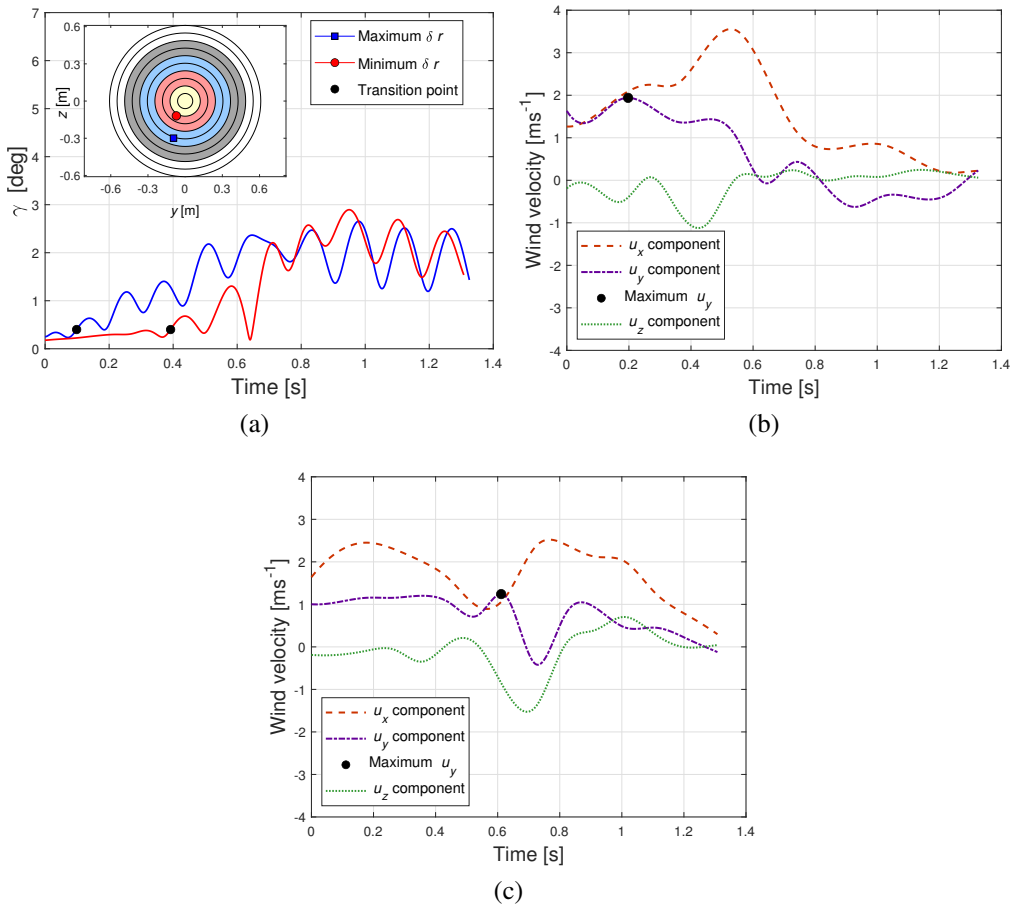

Figure 6.40: a) Time evolution of the angle of attack and impact points for shots with maximum and minimum δr in the field II using an A/C/E arrow with SWV and ideal initial angular velocities. b) Time evolution of the three components of the background wind experienced by the shot with maximum δr. c) Time evolution of the three components of the background wind experienced by the shot with minimum δr.

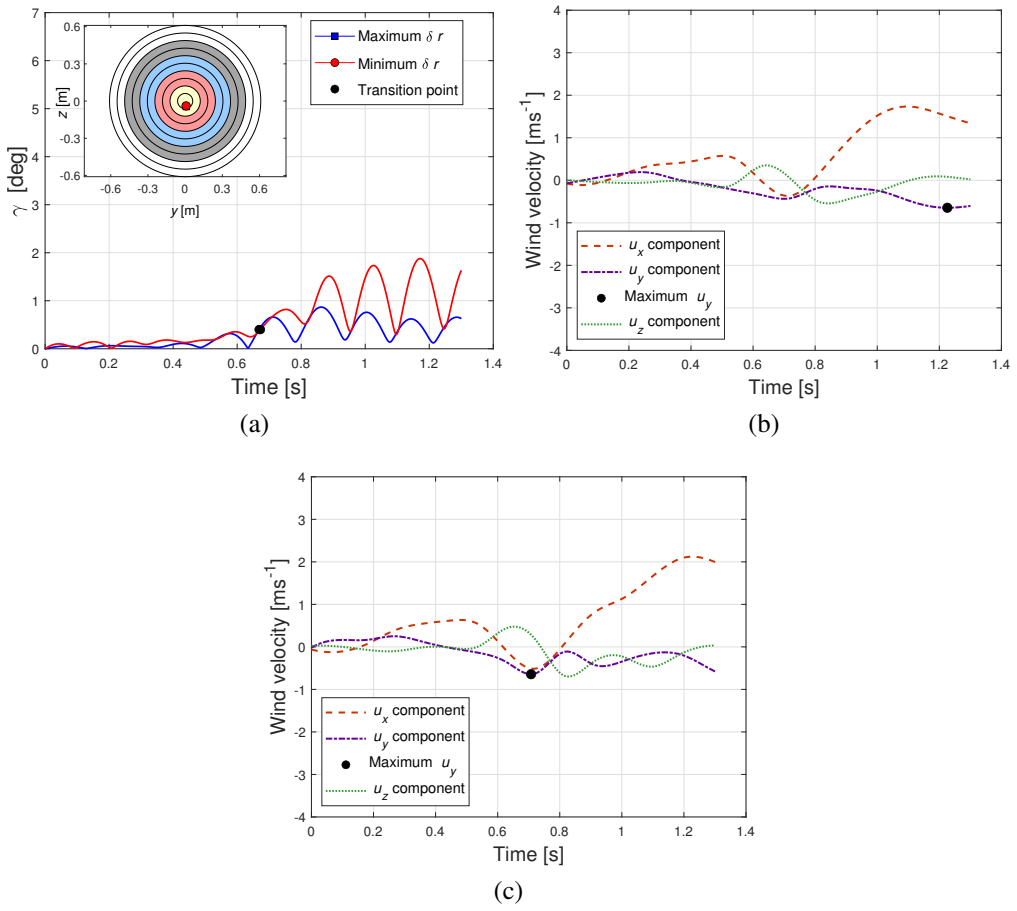

Figure 6.41: a) Time evolution of the angle of attack and impact points for shots with maximum and minimum δr in the field IV using an A/C/E arrow with SWV and ideal initial angular velocities. b) Time evolution of the three components of the background wind experienced by the shot with maximum δr. c) Time evolution of the three components of the background wind experienced by the shot with minimum δr.

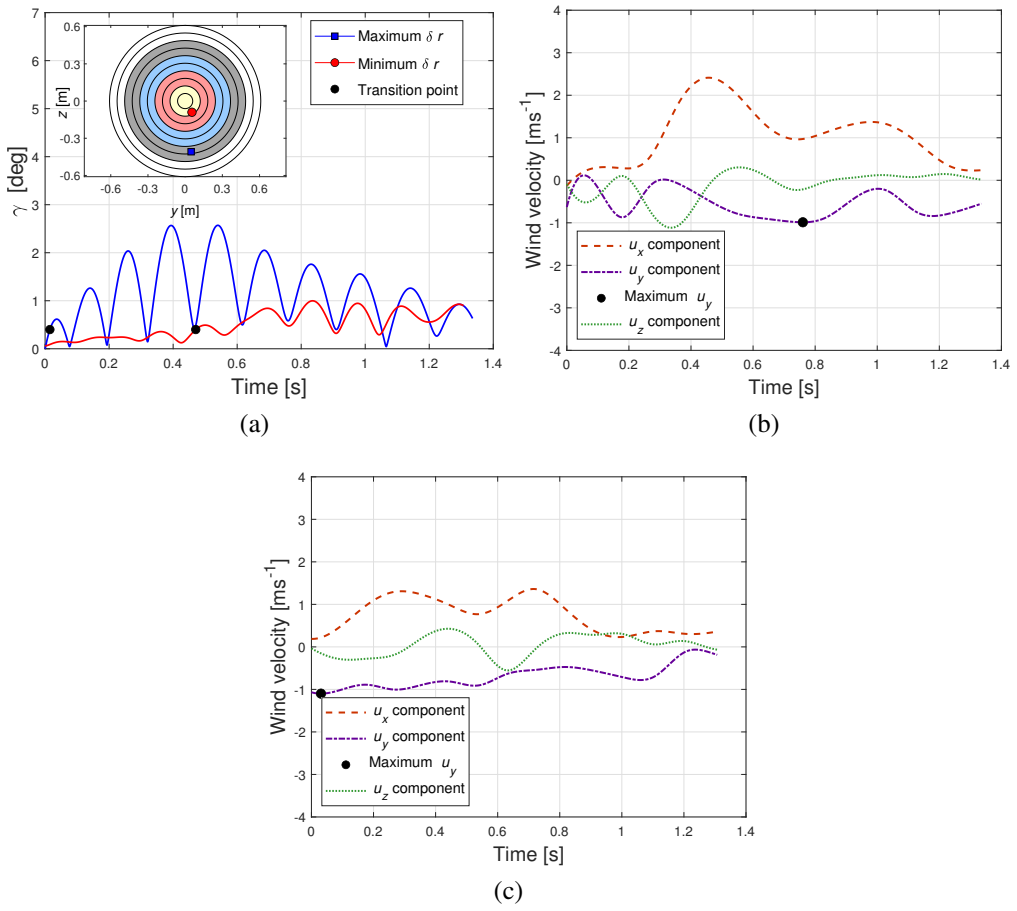

Figure 6.42: a) Time evolution of the angle of attack and impact points for shots with maximum and minimum δr in the field V using an A/C/E arrow with SWV and ideal initial angular velocities. b) Time evolution of the three components of the background wind experienced by the shot with maximum δr. c) Time evolution of the three components of the background wind experienced by the shot with minimum δr.

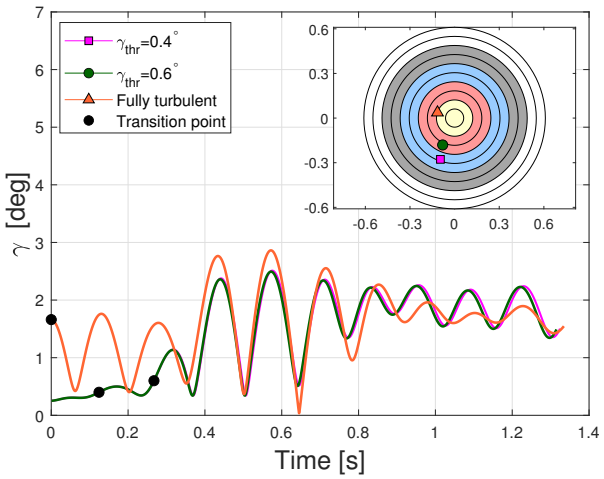

Figure 6.43: Time evolution of the angle of attack for an A/C/E arrow with SWV using two different threshold values of the angle of attack ($\gamma_{\text{thr}} = 0.4^\circ$ and $\gamma_{\text{thr}} = 0.6^\circ$) with the ideal initial angular velocities and zero initial angular velocities. All the computations were carried out in the field II at identical initial background wind conditions.

6.5.4 Time evolution of the velocity for shots in the Olympic archery range

Finally, Figure 6.44 shows the time evolution of the velocity for the previous three shots considered in Section 6.5.3. The shot with a turbulent boundary layer from the beginning of the trajectory retained 85.1% of its velocity when hit the target located 70 m away from the shooting position. The shots with $\gamma_{\text{thr}} = 0.4^\circ$ and $\gamma_{\text{thr}} = 0.6^\circ$ preserved 85.8% and 86.5% of the velocity, respectively. The delay of the boundary layer transition to a turbulent regimes allows the arrows to preserve more of their kinetic energy. Arrows with larger velocities show less deviated trajectories, therefore avoiding the transition of boundary layer flow must be crucial in designing and constructing the archery arrows.

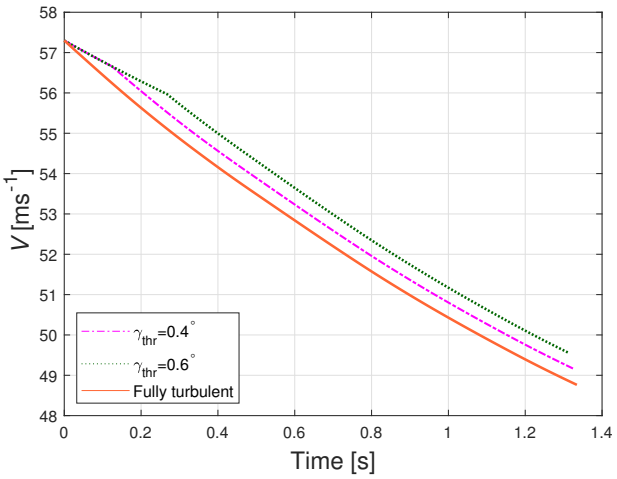

Figure 6.44: Time evolution of velocity for an A/C/E arrow with SWV using two different threshold values of the angle of attack ($\gamma_{\text{thr}} = 0.4^\circ$ and $\gamma_{\text{thr}} = 0.6^\circ$) with the ideal initial angular velocities and zero initial angular velocities. All the computations were carried out in the field II at identical initial background wind conditions.

Chapter 7

Summary, conclusions and further work

This chapter is devoted to firstly, a summary of the current work with the main findings and conclusions. Further ideas are explored in the ending part of the chapter. Let us first give the summary and the conclusions in Section 7.1.

7.1 Summary and conclusions

In the current work, the aerodynamic characteristics of commercial archery arrows were studied. Since the archery competition is a quite popular sport discipline, many sporting companies produce their own products, all of them with different physical characteristics. Carrying out studies of all the available products in the market results non-viable due to the complexity and high cost of the experimental procedures. Therefore, a limited number of elements were analysed in the current work. Let us enlist the main features of such elements,

- The main part of the body of an arrow is the shaft. A slender, light and flexible shaft allows the arrows to translate in an stable way. Two shafts were considered, i.e. the A/C/E and X10 shafts. The latter with smaller mean diameter and larger mass than the former. The mass of the shaft accounts in more than 80% the mass of an arrow.

- In the leading part of the arrow a point is fixed. In the current work, we analysed the commonly used bulge points. One physical characteristic of the bulge point is that its maximum diameter is larger than the arrow's mean diameter. The second type of point considered was the streamlined point. The streamlined point was considered because the fluid flow around the arrow's

leading part is crucial for the aerodynamic characteristics. The streamlined point posses a different profile to the surrounding air than the bulge point.

- The third important element of an arrow are the vanes located in its rear part. The vanes provide the arrows with stable flights. An arrow that is not stable would not travel the 70 m of an archery range successfully. Here, four types of vanes were considered. Two of them are curved and two are straight. The curved vanes were the SPIN-WING-VANES (SWV) and the Gas Pro Vanes (GPV), whereas the straight vanes were referred as the short and large straight vanes, according to their area.

All the mentioned elements, shafts, points and vanes, provide the arrows with different aerodynamic properties. In order to measure such aerodynamic properties, we carried out two different experimental procedures, i.e.

- Experiments in the JAXA's Magnetic Suspension and Balance System (MSBS), which is a magnetic wind tunnel. The arrows were suspended magnetically against gravity, allowing to quantify precisely the pitching moment C_{M}, lift C_{L} and drag C_{D} coefficients for the different arrow configurations. The Re-range in the MSBS experiments was $2.5 \times 10^3 < \mathrm{Re} < 2.0 \times 10^4$.

- Free flight tests, in which the arrows were shot using a compressed-air launching system. The trajectories of the arrows were recorded from the side using several high-speed video cameras. By analysing the video recordings, it was possible to obtain the initial and final conditions of the shots. An acceleration sensor was inserted in the arrows using straight vanes to measure the instantaneous downrange deceleration and rotation rates.

Since the arrows stay in the air less than 1.2 s during our experiments in a 55 m archery range, and considering that the number of located cameras was limited, it was difficult to observe in detail their trajectories and change in their orientation (or attitude). Therefore, we developed a mathematical model to describe the dynamics of archery arrows, in which the arrows were assumed to behave as rigid bodies. The aerodynamic characteristics obtained from the experimental procedures were introduced in the mathematical model to study the response of the arrows to several conditions. It is worth to mention that solving analytically the equations of an arrow motion would be a challenging task. Therefore the system of differential equations were numerically computed.

Since the archery competitions are performed outdoor, the background wind is an important element to consider. The background wind is one of the elements that affects both the archers and the flying arrows considerably. Using numerical simulations we studied the response of the arrows under several conditions, i.e.

- Still-air conditions, in which the influence of the background wind is neglected.
- Uniform background wind, in which the velocity of the wind remains constant regardless of the position of the arrow.
- Non-uniform background wind, in which the wind velocity has a sinusoidal behaviour along the archery range with a maximum at approximately the middle of the trajectory.
- Actual background wind, in which there were considered the wind characteristics in the place where the Tokyo Olympic Archery Competition will take place. The wind information was computed numerically by JAMSTEC and described the actual wind behaviour for 30 s.

By using the numerical simulations it was possible to compute the trajectory, attitude and downrange velocities for arrows under different scenarios. Let us now close the current section with the main findings from the experimental procedures and the numerical simulations.

7.1.1 Conclusions from the MSBS experiments

The current subsection provides the main findings from the MSBS experiments for several arrow configurations. A summary of the findings is listed below.

- Modern archery arrows are stable projectiles. During their flights and due to the presence of an angle of attack (γ) different from zero ($\gamma \neq 0$), a pitching moment arises due to the lift mainly induced by the vanes. The pitching moment acts around the center of gravity ($c.g.$), whereas the lift is exerted in the center of pressure ($c.p.$). During the MSBS experiments, the X10 arrows developed larger C_{M} and C_{L} than the A/C/E arrows.
- A/C/E arrows that were fletched with the large straight vanes developed larger lift and pitching moment coefficients than the arrows using straight short vanes at the same Re. This arises due to the larger area of the straight large vanes.
- The attitude of the arrow is decisive for the state of the boundary layer characteristics. As $|\gamma|$ increases, the value of the drag coefficient (C_{D}) increases abruptly, which is indicative of the transition from laminar to turbulent boundary layer. Such transition takes place regardless the type of arrow.

- The curved SWV contributed with around 53% of the total drag for an A/C/E arrow. When the A/C/E arrow was aligned with the wind flow ($\gamma = 0$), laminar values of the drag coefficient were found in the range $5.5 \times 10^3 < \mathrm{Re} < 1.3 \times 10^4$. At $\mathrm{Re} = 1.3 \times 10^4$, the laminar drag coefficient was $C_\mathrm{D} \sim 1.5$.

- When an angle of attack of $\gamma = 0.75^\circ$ was set between the A/C/E arrow with SWV and the wind flow, the transition from laminar to turbulent boundary layer took place at a lower $\mathrm{Re} = 1.0 \times 10^4$. The turbulent values of the drag coefficient were $C_\mathrm{D} \sim 3.0$ in the range $1.2 \times 10^4 < \mathrm{Re} < 1.4 \times 10^4$.

- When the angle of attack was $\gamma = 0$, laminar values of C_D were found for the X10 with SWV arrow in the range $2.5 \times 10^3 < \mathrm{Re} < 2.0 \times 10^4$. The drag exerted on both the A/C/E and X10 arrows with SWV was found to be almost identical at a fixed Re for turbulent boundary layers, since the ratio of the C_D times the squared values of the radius (r) was around 1.

- For A/C/E arrows with straight vanes, laminar values of the drag coefficient were found in the range $2.5 \times 10^3 < \mathrm{Re} < 1.4 \times 10^4$ when $\gamma = 0$. At $\mathrm{Re} < 1.2 \times 10^4$, the laminar values of the drag coefficient were $C_\mathrm{D} = 1.5$ and $C_\mathrm{D} = 2.0$ for the A/C/E arrows with short and large straight vanes, respectively.

- Similar values of the laminar and turbulent C_D for A/C/E arrows with curved SWV and straight short vanes were found. Laminar values of $C_\mathrm{D} = 1.5$ were found at $\mathrm{Re} = 1.0 \times 10^4$ for both types of arrows. Whereas the turbulent values of $C_\mathrm{D} = 3.0$ were found at $\mathrm{Re} = 1.4 \times 10^4$.

7.1.2 Conclusions from the free flight tests

Unlike the experiments in the MSBS, during the free flight tests the attitude of the arrows cannot be controlled. Further, from the free flight test it was possible to obtain the values of the C_D at larger Re than in the MSBS experiments. Moreover, the instantaneous deceleration, drag coefficient, velocities and rotation rate for A/C/E arrows using short and large straight vanes were measured with an acceleration sensor. A summary of the major findings from the free flight tests is given below.

- For an A/C/E arrow with SWV at relatively low values of Reynolds numbers of around 1.0×10^4, laminar values of $C_\mathrm{D} \sim 1.5$ were obtained. The transition region was located in the range $1.3 \times 10^4 < \mathrm{Re} < 1.8 \times 10^4$. The turbulent values $C_\mathrm{D} \sim 2.7$ were found for the range $2.0 \times 10^4 < \mathrm{Re} < 2.4 \times 10^4$.

- For an X10 arrow with SWV, the turbulent values $C_D \sim 3.2$ were obtained for $Re > 1.6 \times 10^4$.

- For the A/C/E arrow using straight short vanes and a bulge point instantaneous values of around $C_D = 1.5$ were obtained at $Re \sim 1.2 \times 10^4$. Turbulent instantaneous values of $C_D = 2.6$ were found in the range $1.7 \times 10^4 < Re < 2.1 \times 10^4$. These findings are consistent with the MSBS data. When the bulge point was changed to a streamlined point, even at high $Re \sim 2.0 \times 10^4$, laminar values of $C_D \sim 1.3$ were found.

- For the A/C/E arrow using large straight vanes the boundary layer transition zone was located in the range $1.1 \times 10^4 < Re < 1.7 \times 10^4$. In the transition zone the values of the drag coefficient scattered in the range $1.7 < C_D < 3.3$.

- By fletching the straight vanes to A/C/E arrows, the rotation rate can be reduced significantly compared to those arrows with curved vanes. Less than a revolution was observed for shots in the 55 m archery range. The influence of the rotation of the arrow is an element that has to be studied carefully. So far, we were not able to make any conclusion, based on the experimental procedures alone, between the relation of the rotation rate with the boundary layer transition.

7.1.3 Conclusions from the numerical computations

In this subsection the main findings from the numerical computations are given.

- As the arrows travel downrange, the pitching moment exerted around $c.g.$ and the lift exerted in $c.p.$ induce the arrow's oscillation mainly in the vertical plane. Such movement is known as pitching motion. The maximum pitch angle is inversely proportional to the initial velocity of the arrow. Here, the pitching moment is crucial to determine the maximum pitch angle. When the initial velocity was $V_0 = 53$ ms^{-1}, the maximum pitch angles for the A/C/E arrows using straight short and large vanes were 0.40° and 0.30°, respectively. When the initial velocity was increased up to $V_0 = 59$ ms^{-1}, the maximum pitch angles for the A/C/E arrows using straight short and large vanes reduced to 0.31° and 0.23°, respectively. The movement in the horizontal plane, yawing, was several orders of magnitude smaller than the pitching under still-air conditions. Arrows with the large straight vanes undergo oscillation whose maximum pitch angle is smaller than those arrows with short straight vanes.

- The pitching and lift coefficients were found to be crucial to determine the trajectory of the arrows. Arrows generating no pitching moment showed highly deviated trajectories, arising from the absence of the counterbalancing effect against the generated lift.

- Good agreement was found between the measured downrange arrow's velocity decay in the free flight experiments and that obtained from the numerical simulations. The attitude of the arrows was computed using the initial conditions of the actual shots. Fully turbulent boundary layers were found for shots with relatively low values of the angle of attack located in the range $0.4^\circ < \gamma < 0.5^\circ$. This indicates that the state of the boundary layer cannot be elucidated uniquely from the value of γ.

- Under a uniform side-wind of $u_y = 3$ ms^{-1}, large values of the angle of attack, $\gamma = 3^\circ$, were developed by the A/C/E and the X10 arrows. Such magnitudes of γ are considered to be large enough to trigger the transition from a laminar to a turbulent boundary layer.

- It was possible to make angles of attack close to zero along the entire arrows' trajectories if the ideal initial angular velocities were achieved during the shooting stage. Arrows with the correct non-zero value of the initial angular velocities showed less deviated trajectories under the still-air and uniform background winds. A reduction of around 50% was achieved by imparting the ideal initial angular velocities for shots with the A/C/E and X10 arrows, although such initial conditions might be challenging to achieve during actual archery shots.

- The heavier X10 arrows were found to show less deviated trajectories than the lighter A/C/E arrows, irrespective of the background wind characteristics. In a 70 m archery range and with turbulent boundary layers, the X10 arrows retained around 88.1% of their velocity, compared with the 84.5% retained by the A/C/E arrows.

- Even if the ideal initial angular velocities were achieved during the shooting stage, large deviations in the trajectory were found under the actual background wind scenario. An unexpected laminar-turbulent transition of the boundary layer might affect importantly the shots. Large radial deviations from the center of the target of around 0.29 m were found for shots even with the ideal initial conditions. The rapidly changing wind behaviour in outdoor archery ranges disturbs significantly the shots.

- The final deviation in the shots carried out with the ideal initial angular velocities was reduced around 0.09 m by retarding the laminar-turbulent

boundary layer transition around 0.15 s. Nevertheless, the assumption that the boundary layer remains turbulent along the entire arrow's trajectory appears to be wiser than trying to achieve the ideal initial angular velocities.

7.2 Further work

In this section further ideas that might be of interest to consider in the study of the archery arrows are explored.

- **Determination of the angular velocities systematically using refined image processing algorithms.** It has been observed in Chapter 6 the crucial importance of the initial conditions, especially the initial angular velocities, in the dynamics of the archery arrows in free flight and in the boundary layer transition phenomena. Therefore, in an attempt to determine precisely the initial conditions of the shots, refined techniques of image processing could be systematically implemented in the analysis of the high-speed video camera recordings. A brief description of the algorithm for determination of the attitude of the arrow from the high-speed video camera recordings is given in Appendix B.

- **Minimizing the effect of unexpected wind currents at the indoor archery ranges.** Despite that we carefully turned off all the ventilation systems in the indoor archery range, unexpected light background gusts caused by the gradients of temperature may arise in the areas where we set the illumination systems. Since the high-speed video cameras require a good illumination, powerful lamps have to be used around the initial and target locations to increase the quality of the video recordings. This might disturb the wind flow around the archery arrows.

- **Controlled influence of the background wind during the free flight experiments.** Besides carrying experiments under still-air conditions, it also might be interesting to include controlled sources of uniform and not uniform background winds, e.g. fans or ventilation systems located along the entire arrow's trajectory.

- **Reduce the noise in the acceleration sensor induced by the arrows' vibration during free flight.** Until now, the y' and z' components of the instantaneous deceleration were difficult to consider in the numerical computations. This is because during the free flight experiments, the sensor slightly vibrates inside the arrow, resulting in noisy data. Therefore, it is necessary to develop a way to reduce the vibration of the sensor inserted in the arrows.

- **Measure the instantaneous values of the deceleration and rotation rates for arrows using curved vanes.** So far, our measurements with the acceleration sensor were limited to arrows using short and large straight vanes. The reason for this is that by using the straight vanes the arrow's rotation rate can be reduced importantly, compared to the cases when the arrows use curved vanes. Higher rotation rates induced by the curved vanes are out of the measurement range of the present sensor. An acceleration sensor with the capability to measure higher rotation rates is required.

- **Measure the instantaneous values of the deceleration and rotation rates of X10 arrows.** So far, the instantaneous deceleration and rotation rates with the acceleration sensor were limited to the A/C/E arrows. This is due to the difficulty of constructing miniaturized measurement systems able to be inserted in the arrows' shafts. Given the smaller diameter of the X10 arrows, the fabrication of smaller acceleration sensors would be of interest.

Appendix A

Runge-Kutta computation

In this Appendix is described in detail the algorithm to compute the system of coupled equations defined in Chapter 4. The system to solve is defined as an Initial Value Problem (IVP) due to the initial conditions are already known from the experimental procedures. The computations are carried out for the steps $i = 1,2,3,...,n$, where n is the final step. The value of n depends on the total flying time , t_{end}, and is obtained with $n = t_{\text{end}}/\Delta t$. Here Δt is the size step described in Chapter 4.

There exist various types of Runge-Kutta methods, which are classified according to their order. The order identifies the number of points within the subinterval. In the current work is used a fourth order Runge-Kutta method, which means that four intermediate points (K_1, K_2, K_3 and K_4) are used between each step to compute the numerical solution. The local truncation error in fourth order Runge-Kutta method is $O(h^5)$ and the global truncation error is $O(h^4)$, where h is the step size [8].

The system of ten first-order ordinary differential equations, with x, y, z, V, θ, Θ, ϕ, Φ, ω_θ and ω_ϕ as the dependent variables and t as independent variable, has the form:

$$\begin{aligned}
\frac{\mathrm{d}x}{\mathrm{d}t} &= f_1(t,x,y,z,V,\theta,\Theta,\phi,\Phi,\omega_\theta,\omega_\phi),\\
\frac{\mathrm{d}y}{\mathrm{d}t} &= f_2(t,x,y,z,V,\theta,\Theta,\phi,\Phi,\omega_\theta,\omega_\phi),\\
\frac{\mathrm{d}z}{\mathrm{d}t} &= f_3(t,x,y,z,V,\theta,\Theta,\phi,\Phi,\omega_\theta,\omega_\phi),
\end{aligned}$$

$$
\begin{aligned}
\frac{\mathrm{d}V}{\mathrm{d}t} &= f_4(t,x,y,z,V,\theta,\Theta,\phi,\Phi,\omega_\theta,\omega_\phi),\\
\frac{\mathrm{d}\theta}{\mathrm{d}t} &= f_5(t,x,y,z,V,\theta,\Theta,\phi,\Phi,\omega_\theta,\omega_\phi),\\
\frac{\mathrm{d}\Theta}{\mathrm{d}t} &= f_6(t,x,y,z,V,\theta,\Theta,\phi,\Phi,\omega_\theta,\omega_\phi),\\
\frac{\mathrm{d}\phi}{\mathrm{d}t} &= f_7(t,x,y,z,V,\theta,\Theta,\phi,\Phi,\omega_\theta,\omega_\phi),\\
\frac{\mathrm{d}\Phi}{\mathrm{d}t} &= f_8(t,x,y,z,V,\theta,\Theta,\phi,\Phi,\omega_\theta,\omega_\phi),\\
\frac{\mathrm{d}\omega_\theta}{\mathrm{d}t} &= f_9(t,x,y,z,V,\theta,\Theta,\phi,\Phi,\omega_\theta,\omega_\phi),\\
\frac{\mathrm{d}\omega_\phi}{\mathrm{d}t} &= f_{10}(t,x,y,z,V,\theta,\Theta,\phi,\Phi,\omega_\theta,\omega_\phi).
\end{aligned}
\tag{A.1}
$$

For such a system the initial conditions are $x_0, y_0, z_0, V_0, \theta_0, \Theta_0, \phi_0, \Phi_0, \omega_{\theta 0}$ and $\omega_{\phi 0}$. The computation process starts by calculating the value of the first of the four intermediate points for each equation with:

$$
\begin{aligned}
K_{x,1} &= f_1(t_i,x_i,y_i,z_i,V_i,\theta_i,\Theta_i,\phi_i,\Phi_i,\omega_{\theta i},\omega_{\phi i}),\\
K_{y,1} &= f_2(t_i,x_i,y_i,z_i,V_i,\theta_i,\Theta_i,\phi_i,\Phi_i,\omega_{\theta i},\omega_{\phi i}),\\
K_{z,1} &= f_3(t_i,x_i,y_i,z_i,V_i,\theta_i,\Theta_i,\phi_i,\Phi_i,\omega_{\theta i},\omega_{\phi i}),\\
K_{V,1} &= f_4(t_i,x_i,y_i,z_i,V_i,\theta_i,\Theta_i,\phi_i,\Phi_i,\omega_{\theta i},\omega_{\phi i}),\\
K_{\theta,1} &= f_5(t_i,x_i,y_i,z_i,V_i,\theta_i,\Theta_i,\phi_i,\Phi_i,\omega_{\theta i},\omega_{\phi i}),\\
K_{\Theta,1} &= f_6(t_i,x_i,y_i,z_i,V_i,\theta_i,\Theta_i,\phi_i,\Phi_i,\omega_{\theta i},\omega_{\phi i}),\\
K_{\phi,1} &= f_7(t_i,x_i,y_i,z_i,V_i,\theta_i,\Theta_i,\phi_i,\Phi_i,\omega_{\theta i},\omega_{\phi i}),
\end{aligned}
\tag{A.2}
$$

$$
\begin{aligned}
K_{\Phi,1} &= f_8(t_i, x_i, y_i, z_i, V_i, \theta_i, \Theta_i, \phi_i, \Phi_i, \omega_{\theta i}, \omega_{\phi i}), \\
K_{\omega_\theta,1} &= f_9(t_i, x_i, y_i, z_i, V_i, \theta_i, \Theta_i, \phi_i, \Phi_i, \omega_{\theta i}, \omega_{\phi i}), \\
K_{\omega_\phi,1} &= f_{10}(t_i, x_i, y_i, z_i, V_i, \theta_i, \Theta_i, \phi_i, \Phi_i, \omega_{\theta i}, \omega_{\phi i}).
\end{aligned}
$$

The next step is to calculate the value of K_2 for each of the equations:

$$
\begin{aligned}
K_{x,2} &= f_1(t_i + \frac{1}{2}\Delta t, x_i + \frac{1}{2}K_{x,1}\Delta t, y_i + \frac{1}{2}K_{y,1}\Delta t, z_i + \frac{1}{2}K_{z,1}\Delta t, \ldots \\
&\quad V_i + \frac{1}{2}K_{V,1}\Delta t, \theta_i + \frac{1}{2}K_{\theta,1}\Delta t, \Theta_i + \frac{1}{2}K_{\Theta,1}\Delta t, \ldots \\
&\quad \phi_i + \frac{1}{2}K_{\phi,1}\Delta t, \Phi_i + \frac{1}{2}K_{\Phi,1}\Delta t, \omega_{\theta i} + \frac{1}{2}K_{\omega_\theta,1}\Delta t, \ldots \\
&\quad \omega_{\phi i} + \frac{1}{2}K_{\omega_\theta,1}\Delta t), \\
K_{y,2} &= f_2(t_i + \frac{1}{2}\Delta t, x_i + \frac{1}{2}K_{x,1}\Delta t, y_i + \frac{1}{2}K_{y,1}\Delta t, z_i + \frac{1}{2}K_{z,1}\Delta t, \ldots \\
&\quad V_i + \frac{1}{2}K_{V,1}\Delta t, \theta_i + \frac{1}{2}K_{\theta,1}\Delta t, \Theta_i + \frac{1}{2}K_{\Theta,1}\Delta t, \ldots \\
&\quad \phi_i + \frac{1}{2}K_{\phi,1}\Delta t, \Phi_i + \frac{1}{2}K_{\Phi,1}\Delta t, \omega_{\theta i} + \frac{1}{2}K_{\omega_\theta,1}\Delta t, \ldots \\
&\quad \omega_{\phi i} + \frac{1}{2}K_{\omega_\theta,1}\Delta t), \\
K_{z,2} &= f_3(t_i + \frac{1}{2}\Delta t, x_i + \frac{1}{2}K_{x,1}\Delta t, y_i + \frac{1}{2}K_{y,1}\Delta t, z_i + \frac{1}{2}K_{z,1}\Delta t, \ldots \\
&\quad V_i + \frac{1}{2}K_{V,1}\Delta t, \theta_i + \frac{1}{2}K_{\theta,1}\Delta t, \Theta_i + \frac{1}{2}K_{\Theta,1}\Delta t, \ldots \\
&\quad \phi_i + \frac{1}{2}K_{\phi,1}\Delta t, \Phi_i + \frac{1}{2}K_{\Phi,1}\Delta t, \omega_{\theta i} + \frac{1}{2}K_{\omega_\theta,1}\Delta t, \ldots \\
&\quad \omega_{\phi i} + \frac{1}{2}K_{\omega_\theta,1}\Delta t),
\end{aligned}
$$

$$
\begin{aligned}
K_{V,2} &= f_4(t_i+\frac{1}{2}\Delta t, x_i+\frac{1}{2}K_{x,1}\Delta t, y_i+\frac{1}{2}K_{y,1}\Delta t, z_i+\frac{1}{2}K_{z,1}\Delta t, \ldots \\
&\quad V_i+\frac{1}{2}K_{V,1}\Delta t, \theta_i+\frac{1}{2}K_{\theta,1}\Delta t, \Theta_i+\frac{1}{2}K_{\Theta,1}\Delta t, \ldots \\
&\quad \phi_i+\frac{1}{2}K_{\phi,1}\Delta t, \Phi_i+\frac{1}{2}K_{\Phi,1}\Delta t, \omega_{\theta i}+\frac{1}{2}K_{\omega_\theta,1}\Delta t, \ldots \\
&\quad \omega_{\phi i}+\frac{1}{2}K_{\omega_\theta,1}\Delta t), \\
K_{\theta,2} &= f_5(t_i+\frac{1}{2}\Delta t, x_i+\frac{1}{2}K_{x,1}\Delta t, y_i+\frac{1}{2}K_{y,1}\Delta t, z_i+\frac{1}{2}K_{z,1}\Delta t, \ldots \\
&\quad V_i+\frac{1}{2}K_{V,1}\Delta t, \theta_i+\frac{1}{2}K_{\theta,1}\Delta t, \Theta_i+\frac{1}{2}K_{\Theta,1}\Delta t, \ldots \\
&\quad \phi_i+\frac{1}{2}K_{\phi,1}\Delta t, \Phi_i+\frac{1}{2}K_{\Phi,1}\Delta t, \omega_{\theta i}+\frac{1}{2}K_{\omega_\theta,1}\Delta t, \ldots \\
&\quad \omega_{\phi i}+\frac{1}{2}K_{\omega_\theta,1}\Delta t), \\
K_{\Theta,2} &= f_6(t_i+\frac{1}{2}\Delta t, x_i+\frac{1}{2}K_{x,1}\Delta t, y_i+\frac{1}{2}K_{y,1}\Delta t, z_i+\frac{1}{2}K_{z,1}\Delta t, \ldots \\
&\quad V_i+\frac{1}{2}K_{V,1}\Delta t, \theta_i+\frac{1}{2}K_{\theta,1}\Delta t, \Theta_i+\frac{1}{2}K_{\Theta,1}\Delta t, \ldots \\
&\quad \phi_i+\frac{1}{2}K_{\phi,1}\Delta t, \Phi_i+\frac{1}{2}K_{\Phi,1}\Delta t, \omega_{\theta i}+\frac{1}{2}K_{\omega_\theta,1}\Delta t, \ldots \\
&\quad \omega_{\phi i}+\frac{1}{2}K_{\omega_\theta,1}\Delta t), \qquad \text{(A.3)} \\
K_{\phi,2} &= f_7(t_i+\frac{1}{2}\Delta t, x_i+\frac{1}{2}K_{x,1}\Delta t, y_i+\frac{1}{2}K_{y,1}\Delta t, z_i+\frac{1}{2}K_{z,1}\Delta t, \ldots \\
&\quad V_i+\frac{1}{2}K_{V,1}\Delta t, \theta_i+\frac{1}{2}K_{\theta,1}\Delta t, \Theta_i+\frac{1}{2}K_{\Theta,1}\Delta t, \ldots \\
&\quad \phi_i+\frac{1}{2}K_{\phi,1}\Delta t, \Phi_i+\frac{1}{2}K_{\Phi,1}\Delta t, \omega_{\theta i}+\frac{1}{2}K_{\omega_\theta,1}\Delta t, \ldots \\
&\quad \omega_{\phi i}+\frac{1}{2}K_{\omega_\theta,1}\Delta t),
\end{aligned}
$$

$$
\begin{aligned}
K_{\Phi,2} &= f_8(t_i+\frac{1}{2}\Delta t, x_i+\frac{1}{2}K_{x,1}\Delta t, y_i+\frac{1}{2}K_{y,1}\Delta t, z_i+\frac{1}{2}K_{z,1}\Delta t, \ldots \\
&\quad V_i+\frac{1}{2}K_{V,1}\Delta t, \theta_i+\frac{1}{2}K_{\theta,1}\Delta t, \Theta_i+\frac{1}{2}K_{\Theta,1}\Delta t, \ldots \\
&\quad \phi_i+\frac{1}{2}K_{\phi,1}\Delta t, \Phi_i+\frac{1}{2}K_{\Phi,1}\Delta t, \omega_{\theta i}+\frac{1}{2}K_{\omega_\theta,1}\Delta t, \ldots \\
&\quad \omega_{\phi i}+\frac{1}{2}K_{\omega_\theta,1}\Delta t), \\
K_{\omega_\theta,2} &= f_9(t_i+\frac{1}{2}\Delta t, x_i+\frac{1}{2}K_{x,1}\Delta t, y_i+\frac{1}{2}K_{y,1}\Delta t, z_i+\frac{1}{2}K_{z,1}\Delta t, \ldots \\
&\quad V_i+\frac{1}{2}K_{V,1}\Delta t, \theta_i+\frac{1}{2}K_{\theta,1}\Delta t, \Theta_i+\frac{1}{2}K_{\Theta,1}\Delta t, \ldots \\
&\quad \phi_i+\frac{1}{2}K_{\phi,1}\Delta t, \Phi_i+\frac{1}{2}K_{\Phi,1}\Delta t, \omega_{\theta i}+\frac{1}{2}K_{\omega_\theta,1}\Delta t, \ldots \\
&\quad \omega_{\phi i}+\frac{1}{2}K_{\omega_\theta,1}\Delta t), \\
K_{\omega_\phi,2} &= f_{10}(t_i+\frac{1}{2}\Delta t, x_i+\frac{1}{2}K_{x,1}\Delta t, y_i+\frac{1}{2}K_{y,1}\Delta t, z_i+\frac{1}{2}K_{z,1}\Delta t, \ldots \\
&\quad V_i+\frac{1}{2}K_{V,1}\Delta t, \theta_i+\frac{1}{2}K_{\theta,1}\Delta t, \Theta_i+\frac{1}{2}K_{\Theta,1}\Delta t, \ldots \\
&\quad \phi_i+\frac{1}{2}K_{\phi,1}\Delta t, \Phi_i+\frac{1}{2}K_{\Phi,1}\Delta t, \omega_{\theta i}+\frac{1}{2}K_{\omega_\theta,1}\Delta t, \ldots \\
&\quad \omega_{\phi i}+\frac{1}{2}K_{\omega_\theta,1}\Delta t). \qquad \text{(A.4)}
\end{aligned}
$$

This is followed by the calculation of K_3 with:

$$
\begin{aligned}
K_{x,3} &= f_1(t_i+\frac{1}{2}\Delta t, x_i+\frac{1}{2}K_{x,2}\Delta t, y_i+\frac{1}{2}K_{y,2}\Delta t, z_i+\frac{1}{2}K_{z,2}\Delta t, \ldots \\
&\quad V_i+\frac{1}{2}K_{V,2}\Delta t, \theta_i+\frac{1}{2}K_{\theta,2}\Delta t, \Theta_i+\frac{1}{2}K_{\Theta,2}\Delta t, \ldots \\
&\quad \phi_i+\frac{1}{2}K_{\phi,2}\Delta t, \Phi_i+\frac{1}{2}K_{\Phi,2}\Delta t, \omega_{\theta i}+\frac{1}{2}K_{\omega_\theta,2}\Delta t, \ldots \\
&\quad \omega_{\phi i}+\frac{1}{2}K_{\omega_\theta,2}\Delta t),
\end{aligned}
$$

$$
\begin{aligned}
K_{y,3} &= f_2(t_i+\frac{1}{2}\Delta t, x_i+\frac{1}{2}K_{x,2}\Delta t, y_i+\frac{1}{2}K_{y,2}\Delta t, z_i+\frac{1}{2}K_{z,2}\Delta t, \ldots \\
&\quad V_i+\frac{1}{2}K_{V,2}\Delta t, \theta_i+\frac{1}{2}K_{\theta,2}\Delta t, \Theta_i+\frac{1}{2}K_{\Theta,2}\Delta t, \ldots \\
&\quad \phi_i+\frac{1}{2}K_{\phi,2}\Delta t, \Phi_i+\frac{1}{2}K_{\Phi,2}\Delta t, \omega_{\theta i}+\frac{1}{2}K_{\omega_\theta,2}\Delta t, \ldots \\
&\quad \omega_{\phi i}+\frac{1}{2}K_{\omega_\theta,2}\Delta t), \\
K_{z,3} &= f_3(t_i+\frac{1}{2}\Delta t, x_i+\frac{1}{2}K_{x,2}\Delta t, y_i+\frac{1}{2}K_{y,2}\Delta t, z_i+\frac{1}{2}K_{z,2}\Delta t, \ldots \\
&\quad V_i+\frac{1}{2}K_{V,2}\Delta t, \theta_i+\frac{1}{2}K_{\theta,2}\Delta t, \Theta_i+\frac{1}{2}K_{\Theta,2}\Delta t, \ldots \\
&\quad \phi_i+\frac{1}{2}K_{\phi,2}\Delta t, \Phi_i+\frac{1}{2}K_{\Phi,2}\Delta t, \omega_{\theta i}+\frac{1}{2}K_{\omega_\theta,2}\Delta t, \ldots \\
&\quad \omega_{\phi i}+\frac{1}{2}K_{\omega_\theta,2}\Delta t), \\
K_{V,3} &= f_4(t_i+\frac{1}{2}\Delta t, x_i+\frac{1}{2}K_{x,2}\Delta t, y_i+\frac{1}{2}K_{y,2}\Delta t, z_i+\frac{1}{2}K_{z,2}\Delta t, \ldots \\
&\quad V_i+\frac{1}{2}K_{V,2}\Delta t, \theta_i+\frac{1}{2}K_{\theta,2}\Delta t, \Theta_i+\frac{1}{2}K_{\Theta,2}\Delta t, \ldots \\
&\quad \phi_i+\frac{1}{2}K_{\phi,2}\Delta t, \Phi_i+\frac{1}{2}K_{\Phi,2}\Delta t, \omega_{\theta i}+\frac{1}{2}K_{\omega_\theta,2}\Delta t, \ldots \\
&\quad \omega_{\phi i}+\frac{1}{2}K_{\omega_\theta,2}\Delta t), \qquad \text{(A.5)} \\
K_{\theta,3} &= f_5(t_i+\frac{1}{2}\Delta t, x_i+\frac{1}{2}K_{x,2}\Delta t, y_i+\frac{1}{2}K_{y,2}\Delta t, z_i+\frac{1}{2}K_{z,2}\Delta t, \ldots \\
&\quad V_i+\frac{1}{2}K_{V,2}\Delta t, \theta_i+\frac{1}{2}K_{\theta,2}\Delta t, \Theta_i+\frac{1}{2}K_{\Theta,2}\Delta t, \ldots \\
&\quad \phi_i+\frac{1}{2}K_{\phi,2}\Delta t, \Phi_i+\frac{1}{2}K_{\Phi,2}\Delta t, \omega_{\theta i}+\frac{1}{2}K_{\omega_\theta,2}\Delta t, \ldots \\
&\quad \omega_{\phi i}+\frac{1}{2}K_{\omega_\theta,2}\Delta t),
\end{aligned}
$$

$$
\begin{aligned}
K_{\Theta,3} &= f_6(t_i+\frac{1}{2}\Delta t, x_i+\frac{1}{2}K_{x,2}\Delta t, y_i+\frac{1}{2}K_{y,2}\Delta t, z_i+\frac{1}{2}K_{z,2}\Delta t, \ldots \\
&\quad V_i+\frac{1}{2}K_{V,2}\Delta t, \theta_i+\frac{1}{2}K_{\theta,2}\Delta t, \Theta_i+\frac{1}{2}K_{\Theta,2}\Delta t, \ldots \\
&\quad \phi_i+\frac{1}{2}K_{\phi,2}\Delta t, \Phi_i+\frac{1}{2}K_{\Phi,2}\Delta t, \omega_{\theta i}+\frac{1}{2}K_{\omega_\theta,2}\Delta t, \ldots \\
&\quad \omega_{\phi i}+\frac{1}{2}K_{\omega_\theta,2}\Delta t), \\
K_{\phi,3} &= f_7(t_i+\frac{1}{2}\Delta t, x_i+\frac{1}{2}K_{x,2}\Delta t, y_i+\frac{1}{2}K_{y,2}\Delta t, z_i+\frac{1}{2}K_{z,2}\Delta t, \ldots \\
&\quad V_i+\frac{1}{2}K_{V,2}\Delta t, \theta_i+\frac{1}{2}K_{\theta,2}\Delta t, \Theta_i+\frac{1}{2}K_{\Theta,2}\Delta t, \ldots \\
&\quad \phi_i+\frac{1}{2}K_{\phi,2}\Delta t, \Phi_i+\frac{1}{2}K_{\Phi,2}\Delta t, \omega_{\theta i}+\frac{1}{2}K_{\omega_\theta,2}\Delta t, \ldots \\
&\quad \omega_{\phi i}+\frac{1}{2}K_{\omega_\theta,2}\Delta t), \\
K_{\Phi,3} &= f_8(t_i+\frac{1}{2}\Delta t, x_i+\frac{1}{2}K_{x,2}\Delta t, y_i+\frac{1}{2}K_{y,2}\Delta t, z_i+\frac{1}{2}K_{z,2}\Delta t, \ldots \\
&\quad V_i+\frac{1}{2}K_{V,2}\Delta t, \theta_i+\frac{1}{2}K_{\theta,2}\Delta t, \Theta_i+\frac{1}{2}K_{\Theta,2}\Delta t, \ldots \\
&\quad \phi_i+\frac{1}{2}K_{\phi,2}\Delta t, \Phi_i+\frac{1}{2}K_{\Phi,2}\Delta t, \omega_{\theta i}+\frac{1}{2}K_{\omega_\theta,2}\Delta t, \ldots \\
&\quad \omega_{\phi i}+\frac{1}{2}K_{\omega_\theta,2}\Delta t), \qquad \text{(A.6)} \\
K_{\omega_\theta,3} &= f_9(t_i+\frac{1}{2}\Delta t, x_i+\frac{1}{2}K_{x,2}\Delta t, y_i+\frac{1}{2}K_{y,2}\Delta t, z_i+\frac{1}{2}K_{z,2}\Delta t, \ldots \\
&\quad V_i+\frac{1}{2}K_{V,2}\Delta t, \theta_i+\frac{1}{2}K_{\theta,2}\Delta t, \Theta_i+\frac{1}{2}K_{\Theta,2}\Delta t, \ldots \\
&\quad \phi_i+\frac{1}{2}K_{\phi,2}\Delta t, \Phi_i+\frac{1}{2}K_{\Phi,2}\Delta t, \omega_{\theta i}+\frac{1}{2}K_{\omega_\theta,2}\Delta t, \ldots \\
&\quad \omega_{\phi i}+\frac{1}{2}K_{\omega_\theta,2}\Delta t),
\end{aligned}
$$

$$\begin{aligned} K_{\omega_\phi,3} &= f_{10}(t_i+\frac{1}{2}\Delta t, x_i+\frac{1}{2}K_{x,2}\Delta t, y_i+\frac{1}{2}K_{y,2}\Delta t, z_i+\frac{1}{2}K_{z,2}\Delta t, \ldots \\ &\quad V_i+\frac{1}{2}K_{V,2}\Delta t, \theta_i+\frac{1}{2}K_{\theta,2}\Delta t, \Theta_i+\frac{1}{2}K_{\Theta,2}\Delta t, \ldots \\ &\quad \phi_i+\frac{1}{2}K_{\phi,2}\Delta t, \Phi_i+\frac{1}{2}K_{\Phi,2}\Delta t, \omega_{\theta i}+\frac{1}{2}K_{\omega_\theta,2}\Delta t, \ldots \\ &\quad \omega_{\phi i}+\frac{1}{2}K_{\omega_\theta,2}\Delta t). \end{aligned}$$

The last intermediate point to calculate is K_4 wich is obtained by:

$$\begin{aligned} K_{x,4} &= f_1(t_i+\Delta t, x_i+K_{x,2}\Delta t, y_i+K_{y,2}\Delta t, z_i+K_{z,2}\Delta t, \ldots \\ &\quad V_i+K_{V,2}\Delta t, \theta_i+K_{\theta,2}\Delta t, \Theta_i+K_{\Theta,2}\Delta t, \ldots \\ &\quad \phi_i+K_{\phi,2}\Delta t, \Phi_i+K_{\Phi,2}\Delta t, \omega_{\theta i}+K_{\omega_\theta,2}\Delta t, \ldots \\ &\quad \omega_{\phi i}+K_{\omega_\theta,2}\Delta t), \\ K_{y,4} &= f_2(t_i+\Delta t, x_i+K_{x,2}\Delta t, y_i+K_{y,2}\Delta t, z_i+K_{z,2}\Delta t, \ldots \\ &\quad V_i+K_{V,2}\Delta t, \theta_i+K_{\theta,2}\Delta t, \Theta_i+K_{\Theta,2}\Delta t, \ldots \\ &\quad \phi_i+K_{\phi,2}\Delta t, \Phi_i+K_{\Phi,2}\Delta t, \omega_{\theta i}+K_{\omega_\theta,2}\Delta t, \ldots \\ &\quad \omega_{\phi i}+K_{\omega_\theta,2}\Delta t), \\ K_{z,4} &= f_3(t_i+\Delta t, x_i+K_{x,2}\Delta t, y_i+K_{y,2}\Delta t, z_i+K_{z,2}\Delta t, \ldots \\ &\quad V_i+K_{V,2}\Delta t, \theta_i+K_{\theta,2}\Delta t, \Theta_i+K_{\Theta,2}\Delta t, \ldots \\ &\quad \phi_i+K_{\phi,2}\Delta t, \Phi_i+K_{\Phi,2}\Delta t, \omega_{\theta i}+K_{\omega_\theta,2}\Delta t, \ldots \\ &\quad \omega_{\phi i}+K_{\omega_\theta,2}\Delta t), \\ K_{V,4} &= f_4(t_i+\Delta t, x_i+K_{x,2}\Delta t, y_i+K_{y,2}\Delta t, z_i+K_{z,2}\Delta t, \ldots \\ &\quad V_i+K_{V,2}\Delta t, \theta_i+K_{\theta,2}\Delta t, \Theta_i+K_{\Theta,2}\Delta t, \ldots \\ &\quad \phi_i+K_{\phi,2}\Delta t, \Phi_i+K_{\Phi,2}\Delta t, \omega_{\theta i}+K_{\omega_\theta,2}\Delta t, \ldots \\ &\quad \omega_{\phi i}+K_{\omega_\theta,2}\Delta t), \end{aligned}$$

$$
\begin{aligned}
K_{\theta,4} &= f_5(t_i+\Delta t, x_i+K_{x,2}\Delta t, y_i+K_{y,2}\Delta t, z_i+K_{z,2}\Delta t, \ldots \\
&\quad V_i+K_{V,2}\Delta t, \theta_i+K_{\theta,2}\Delta t, \Theta_i+K_{\Theta,2}\Delta t, \ldots \\
&\quad \phi_i+K_{\phi,2}\Delta t, \Phi_i+K_{\Phi,2}\Delta t, \omega_{\theta i}+K_{\omega_\theta,2}\Delta t, \ldots \\
&\quad \omega_{\phi i}+K_{\omega_\theta,2}\Delta t), \\
K_{\Theta,4} &= f_6(t_i+\Delta t, x_i+K_{x,2}\Delta t, y_i+K_{y,2}\Delta t, z_i+K_{z,2}\Delta t, \ldots \\
&\quad V_i+K_{V,2}\Delta t, \theta_i+K_{\theta,2}\Delta t, \Theta_i+K_{\Theta,2}\Delta t, \ldots \\
&\quad \phi_i+K_{\phi,2}\Delta t, \Phi_i+K_{\Phi,2}\Delta t, \omega_{\theta i}+K_{\omega_\theta,2}\Delta t, \ldots \\
&\quad \omega_{\phi i}+K_{\omega_\theta,2}\Delta t), \\
K_{\phi,4} &= f_7(t_i+\Delta t, x_i+K_{x,2}\Delta t, y_i+K_{y,2}\Delta t, z_i+K_{z,2}\Delta t, \ldots \\
&\quad V_i+K_{V,2}\Delta t, \theta_i+K_{\theta,2}\Delta t, \Theta_i+K_{\Theta,2}\Delta t, \ldots \\
&\quad \phi_i+K_{\phi,2}\Delta t, \Phi_i+K_{\Phi,2}\Delta t, \omega_{\theta i}+K_{\omega_\theta,2}\Delta t, \ldots \\
&\quad \omega_{\phi i}+K_{\omega_\theta,2}\Delta t), \\
K_{\Phi,4} &= f_8(t_i+\Delta t, x_i+K_{x,2}\Delta t, y_i+K_{y,2}\Delta t, z_i+K_{z,2}\Delta t, \ldots \\
&\quad V_i+K_{V,2}\Delta t, \theta_i+K_{\theta,2}\Delta t, \Theta_i+K_{\Theta,2}\Delta t, \ldots \\
&\quad \phi_i+K_{\phi,2}\Delta t, \Phi_i+K_{\Phi,2}\Delta t, \omega_{\theta i}+K_{\omega_\theta,2}\Delta t, \ldots \\
&\quad \omega_{\phi i}+K_{\omega_\theta,2}\Delta t), \\
K_{\omega_\theta,4} &= f_9(t_i+\Delta t, x_i+K_{x,2}\Delta t, y_i+K_{y,2}\Delta t, z_i+K_{z,2}\Delta t, \ldots \\
&\quad V_i+K_{V,2}\Delta t, \theta_i+K_{\theta,2}\Delta t, \Theta_i+K_{\Theta,2}\Delta t, \ldots \\
&\quad \phi_i+K_{\phi,2}\Delta t, \Phi_i+K_{\Phi,2}\Delta t, \omega_{\theta i}+K_{\omega_\theta,2}\Delta t, \ldots \\
&\quad \omega_{\phi i}+K_{\omega_\theta,2}\Delta t), \\
K_{\omega_\phi,4} &= f_{10}(t_i+\Delta t, x_i+K_{x,2}\Delta t, y_i+K_{y,2}\Delta t, z_i+K_{z,2}\Delta t, \ldots \\
&\quad V_i+K_{V,2}\Delta t, \theta_i+K_{\theta,2}\Delta t, \Theta_i+K_{\Theta,2}\Delta t, \ldots \\
&\quad \phi_i+K_{\phi,2}\Delta t, \Phi_i+K_{\Phi,2}\Delta t, \omega_{\theta i}+K_{\omega_\theta,2}\Delta t, \ldots \\
&\quad \omega_{\phi i}+K_{\omega_\theta,2}\Delta t). \qquad \text{(A.7)}
\end{aligned}
$$

Once the four intermediate points for each differential equation are obtained, the value of the dependent variables at $t = t_{i+1}$ can be computed with:

$$
\begin{aligned}
x_{i+1} &= x_i + \frac{1}{6}(K_{x,1} + 2K_{x,2} + 2K_{x,3} + K_{x,4})\Delta t, \\
y_{i+1} &= y_i + \frac{1}{6}(K_{y,1} + 2K_{y,2} + 2K_{y,3} + K_{y,4})\Delta t, \\
z_{i+1} &= z_i + \frac{1}{6}(K_{z,1} + 2K_{z,2} + 2K_{z,3} + K_{z,4})\Delta t, \\
V_{i+1} &= V_i + \frac{1}{6}(K_{V,1} + 2K_{V,2} + 2K_{V,3} + K_{V,4})\Delta t, \\
\theta_{i+1} &= \theta_i + \frac{1}{6}(K_{\theta,1} + 2K_{\theta,2} + 2K_{\theta,3} + K_{\theta,4})\Delta t, \\
\Theta_{i+1} &= \Theta_i + \frac{1}{6}(K_{\Theta,1} + 2K_{\Theta,2} + 2K_{\Theta,3} + K_{\Theta,4})\Delta t, \\
\phi_{i+1} &= \phi_i + \frac{1}{6}(K_{\phi,1} + 2K_{\phi,2} + 2K_{\phi,3} + K_{\phi,4})\Delta t, \\
\Phi_{i+1} &= \Phi_i + \frac{1}{6}(K_{\Phi,1} + 2K_{\Phi,2} + 2K_{\Phi,3} + K_{\Phi,4})\Delta t, \\
\omega_{\theta i+1} &= \omega_{\theta i} + \frac{1}{6}(K_{\omega_\theta,1} + 2K_{\omega_\theta,2} + 2K_{\omega_\theta,3} + K_{\omega_\theta,4})\Delta t, \\
\omega_{\phi i+1} &= \omega_{\phi i} + \frac{1}{6}(K_{\omega_\phi,1} + 2K_{\omega_\phi,2} + 2K_{\omega_\phi,3} + K_{\omega_\phi,4})\Delta t.
\end{aligned}
\tag{A.8}
$$

The described algorithm was programmed in a self-written MATLAB script. Nevertheless, similar results can be obtained with different software or programming languages, e.g. FORTRAN or Python.

Appendix B

Image processing of the video recordings

In this section are given the generalities of an algorithm that analyses in a detailed and systematic way the high-speed video camera recordings to obtain the initial values of the angle of attack and angular velocities. Figure B.1 shows one frame extracted from the high-speed video camera recordings in which it is possible to observe the flying arrow. Note from Figure B.1 that besides the image of the actual arrow, its shadow can be observed. Further, irregularities in the illumination provokes the reduction of the quality of the recorded image making necessary to implement, firstly, several types of filtering and image manipulation techniques. For every frame in the videos, cutting, reduction, binarization, edge detection and clustering algorithms can be automatically implemented to determine precisely the attitude of the flying arrows.

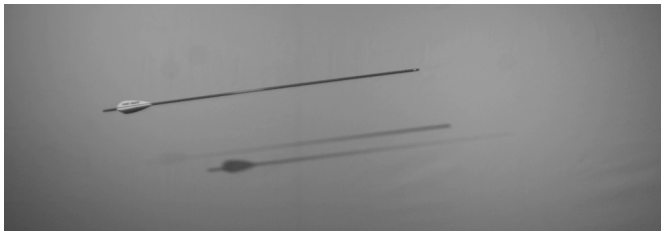

Figure B.1: A single original frame of the flying arrow from the high-speed video camera recordings.

The process of binarization in Figure B.2 consists in techniques of thresholding the original image by comparing each pixel intensity with a reference thresh-

old value and replacing the pixel with a white or black value. By reducing the original gray scale image into a monochrome image, the analysis algorithm can be simplified and the speed of computation reduced.

Figure B.2: A single binary image of the flying arrow from the high-speed video camera recordings.

Once that the binary image was obtained, it is possible to implement techniques of edge detection as shown in Figure B.3. The edge detection is a fundamental image processing operation commonly used in computer vision solutions. The goal of the edge detection procedure is to find the most relevant edges in an image or scene. By applying the edge detection techniques, it is possible to differentiate the edges of the arrow and the shadows in the background. Here the Prewitt edge detector was implemented due to its simplicity [21].

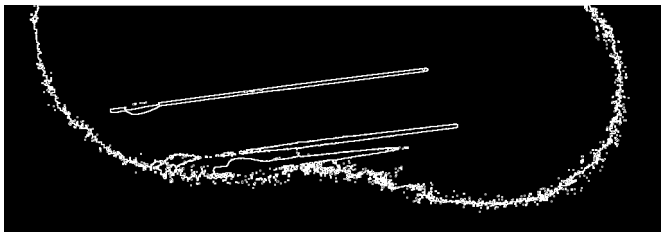

Figure B.3: A single frame of the flying arrow in which the relevant edges were obtained with a Prewitt edge detector.

Once the relevant edges were detected, it is possible to group and differentiate the arrows from the background. By using a density based clustering algorithm, it is possible to group the pixels corresponding to the arrow to compute in a coherent way the angular velocities and arrow orientation. Here, a density based

spatial clustering algorithm (DBSCAN) was implemented because it does not require a pre-set of cluster numbers. The DBSCAN can find arbitrarily sized and shaped clusters, representing a great advantage over other clustering algorithms, e.g. the k-means and mean-shift clustering. Since the archery arrows cannot be represented as a body with simple geometries, the DBSCAN algorithm was used to identify the arrows at every iteration. Figure B.4 shows the identified arrow for a given frame.

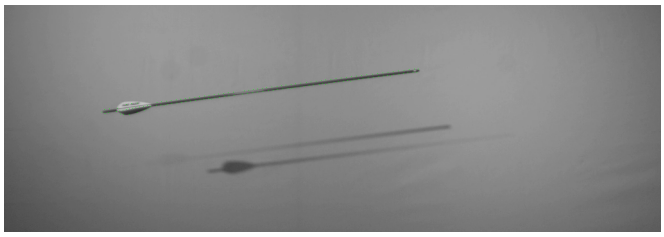

Figure B.4: A single frame in which the flying arrow can be distinguished from the surroundings using a density based spatial clustering algorithm.

By applying the process described in Figures B.1, B.2, B.3 and B.4 at every time step, it is possible to obtain the attitude of the arrow with respect with the inertial frame of reference. In this way, the time evolution of the angle of attack and the angular velocities could be determined precisely at the locations where the high-speed video cameras are located.

Bibliography

[1] Allen T and Goff J E, Resources for sports engineering education, J E Sports Eng, 1-9 (2017)

[2] Ascham R, Toxophilus (1545). Retrieved from https:// www.archerylibrary.com/ books/ toxophilus/

[3] Denny M, Their arrows will darken the sky. The Johns Hopkins University Press, Baltimore (2011).

[4] Barton J, Vcelák J, Torres-Sanchez J, O'Flynn B, O'Mathuna C and Donahoe RV, A miniaturised arrow ballistic measurement system, SENSORS, 2011 IEEE, Limerick, pp. 1289-1292 (2011). DOI: 10.1109/ICSENS.2011.6127412.

[5] Barton J, Vcelák J, Torres-Sanchez J, O'Flynn B, O'Mathuna C, Donahoe RV, Arrow mounted ballistic system for measuring performance of arrows equipped with hunting broadheads, Procedia Engineering, 34: 455-460 (2012). DOI: https://doi.org/ 10.1016/j.proeng.2012.04.078.

[6] Easton Technical Products, 2012 Easton Catalogue (2012).

[7] Everett D, Don't sleep, there are snakes. Life and language in the Amazonian jungle, Profile Books, USA (2009).

[8] Gilat and Subramaniam, Numerical methods for engineers and scientists: an introduction with applications using matlab, Wiley, 3rd edn., USA (2014).

[9] Goff J, A review of recent research into aerodynamics of sports projectiles, J E Sports Eng, 16, 137-154 (2013).

[10] Haake S, The impact of technology on sporting performance in Olympic Sports, J Sport Sci, 27:13, 1421-1431 (2009).

[11] van Hooff T, Blocken B, van Harten M, 3D CFD simulations of wind flow and wind-driven rain shelter in sports stadia: Influence of stadium geometry, Build Environ, 46:1, 22-37 (2011).

[12] Hubbard M, Simulation of javeling flight using experimental aerodynamic data, J Biomech, 17:10, 769-776 (1984).

[13] Hubbard M Optimal javelin trajectories, J Biomech, 17:10, 777-787 (1984).

[14] Jackson P. B., Overview of Missile Flight Control Systems (2010).

[15] Jung A, Muller W, Staat M, Wind and fairness in ski jumping: A computer modelling analysis, J Biomech, 75, 147-153 (2018).

[16] Kelly H R, A note on the laminar boundary layer on a circular cylinder in axial incompressible flow, J. Aeronaut. Sci., 21, 634 (1954).

[17] Kooi B W, Bow-arrow interaction in archery, J Sport Sci, 16, 721-731 (1998).

[18] Kooi B W, Sparenberg J A, On the mechanics of the arrow: Archer's paradox, J Eng Math, 31, 285-306 (1997).

[19] Kuch A, Debril J-F, Tizzoni J-M, Laguillaumie P and Monnet T. A study of the influence of arrow mass on ballistics, Comput Method Biomec, 22:1, S526-S528 (2019). DOI: 10.1080/10255842.2020.1715006

[20] Lu L, Onishi R and Takahashi K. The effect of wind on long-term summer water temperature trends in Tokyo Bay, Japan. Ocean Dynamics, 65, 919-930 (2015). DOI: https://doi.org/10.1007/s10236-015-0848-4

[21] Marques Oge, Practical image and video processing using Matlab, Wiley, USA (2011).

[22] Miyazaki T et al., Indeterminacy of drag exerted on an Arrow in free Flight: arrow attitude and laminar-turbulent transition, Eur J Phys,38,6 (2017).

[23] Miyazaki T et al., Aerodynamic properties of an archery arrow , Sports Eng, 16:1, 43-54 (2013)

[24] Müller M (2014) After Sochi 2014: cost and impacts of Russia's Olympic Games *Eurasian Geography and Economics* 55(6) 628-655 (2014). DOI: 10.1080/15387216.2015.1040432

[25] Pan H (2012) Study in Scientific and technological Olympic Games *Information Technology in Medicine and Education, International Symposium IEEE*

[26] Park J, Arrow behaviour in free flight, Proc Inst Mech Eng P J Sports Eng Technol, 225, 241-252 (2011)

[27] Park J, Arrow behaviour in the lateral plane during and immediately following the power stroke of a recurve archery bow, Proc Inst Mech Eng P J Sports Eng Technol, 227, 172-183 (2012). DOI:https://doi.org/10.1177/1754337112464844

[28] Park J, Arrow behaviour in the vertical plane during and immediately following the power stroke of a recurve bow, Proc Inst Mech Eng P J Sports Eng Technol, 228, 16-23 (2013). DOI:https://doi.org/10.1177/1754337113501492

[29] Park J, Hodge M, Al-Mulla S, Sherry N and Sheridan J, Air flow around the point of an arrow, Proc Inst Mech Eng P J Sports Eng Technol, 1-6 (published online) (2011)

[30] Park J, Minimizing wind drift of an arrow, Proc Inst Mech Eng P J Sports Eng Technol, 226 52-60 (2011)

[31] Park J, The dynamic behaviour of an arrow in wind, Proc Inst Mech Eng P J Sports Eng Technol, 234:268-277 (2020). DOI: 10.1177/1754337120910015

[32] Park J, The impact of the atmosphere on target archery, Proc Inst Mech Eng P J Sports Eng Technol *published online* (2019). DOI: 10.1177/1754337118823967

[33] Sawada H et al., Wind tunnel test of Japanese arrows with the JAXA-60 cm magnetic suspension and balance system, Exp Fluids, 53, 451-466 (2012).

[34] Seban R A and Bond R, Skin-friction and heat-transfer characteristics of a laminar boundary layer on a cylinder in axial incompressible flow, J. Aeronaut. Sci., 18, 671-5 (1951).

[35] Tanentzap A, Taylor P, Yan N and Salmon J, On Sudbury-area wind speeds-A tale of forest regeneration, J Appl Meteorol Climatol, 46:10, 1645-1654 (2007).

[36] Yaghoobian N and Mittal R, A computational approach for predicting plant canopy induced wind effects on the trajectory of golf shots, Sports Eng, 21, 1-10 (2018)

[37] Zanevsky I, Bow tuning in the vertical plane, Sports Eng, 9, 77-86 (2006). DOI:https://doi.org/10.1007/BF02844860

List of publications

Academic papers:

1. Ortiz Julio, Ando Masato, Miyazaki Takeshi. Numerical Simulation of Wind Drift of Arrows on the Olympic Venue for Tokyo 2020. Athens Journal of Sports, 7, 1, pages 1-20 (2020). DOI: 10.30958/ajspo.7-1-1

2. Ortiz Julio, Ando Masato, Murayama Kentaro, Miyazaki Takeshi and Sugiura Hiroki. Computation of the Trajectory and Attitude of Arrows Subject to Background Wind. Sports Engineering, 22, 7 (2019).
DOI: https://doi.org/10.1007/s12283-019-0302-9

International conferences:

1. Ortiz Julio, Serino Atsushi, Hasegawa Toshinari, Onoguchi Takahito, Maemukai Hiroki, Miyazaki Takeshi and Sugiura Hiroki. Experimental and Computational Study of Archery Arrows Fletched with Straight Vanes. Proceedings, 49, 56 (2020). DOI: 10.3390/proceedings2020049056

Other publications:

1. Miyazaki Takeshi, Matsumoto Tatsumasa, Ando Ryu, Ortiz Julio and Sugiura Hiroki. Indeterminacy of drag exerted on an arrow in free flight: arrow attitude and laminar-turbulent transition. European Journal of Physics, 38 (2017). DOI: https://doi.org/10.1088/1361-6404/aa8339